TRIM ANGLE OF ATTACK OF FLEXIBLE WINGS USING NON-LINEAR AERODYNAMICS

By
David E. Cohen

A DISSERTATION SUBMITTED TO THE FACULTY OF
VIRGINIA POLYTECHNIC INSTITUTE AND STATE UNIVERSITY
IN PARTIAL FULFILLMENT OF THE REQUIREMENTS FOR THE DEGREE OF
DOCTOR OF PHILOSOPHY
IN
AEROSPACE ENGINEERING

Rakesh K. Kapania, Co-Chairman

Robert W. Walters, Co-Chairman

Bernard Grossman

Eric Johnson

Joseph A. Schetz

April 1998

Blacksburg, Virginia

Trim Angle of Attack of Flexible Wings Using Non-Linear Aerodynamics

by

David E. Cohen

Committee Chairmen: Rakesh K. Kapania and Robert W. Walters

Aerospace and Ocean Engineering

(ABSTRACT)

Multidisciplinary interactions are expected to play a significant role in the design of future high-performance aircraft (Blended-Wing Body, Truss-Braced wing, High Speed Civil transport, High-Altitude Long Endurance aircraft and future military aircraft). Also, the availability of supercomputers has made it now possible to employ high-fidelity models (Computational Fluid Dynamics for fluids and detailed finite element models for structures) at the preliminary design stage. A necessary step at that stage is to calculate the wing angle-of-attack at which the wing will generate the desired lift for the specific flight maneuver. Determination of this angle, a simple affair when the wing is rigid and the flow regime linear, becomes difficult when the wing is flexible and the flow regime non-linear. To solve this inherently nonlinear problem, a Newton's method type algorithm is developed to simultaneously calculate the deflection and the angle of attack. The present algorithm requires the sensitivity of the aerodynamic pressure with respect to each of the generalized displacement coordinates needed to represent the structural displacement. This sensitivity data is easy to determine analytically when the flow regime is linear. The present algorithm uses a finite difference method to obtain these sensitivities and thus requires only the pressure data and the surface geometry from the aerodynamic model. This makes

it ideally suited for nonlinear aerodynamics for which it is difficult to obtain the sensitivity analytically.

The present algorithm requires the CFD code to be run for each of the generalized coordinates. Therefore, to reduce the number of generalized coordinates considerably, we employ the modal superposition approach to represent the structural displacements. Results available for the Aeroelastic Research Wing (ARW) are used to evaluate the performance of the modal superposition approach. Calculations are made at a fixed angle of attack and the results are compared to both the experimental results obtained at NASA Langley Research Center, and computational results obtained by the researchers at NASA Ames Research Center. Two CFD codes are used to demonstrate the modular nature of this research. Similarly, two separate Finite Element codes are used to generate the structural data, demonstrating that the algorithm is not dependent on using specific codes.

The developed algorithm is tested for a wing, used for in-house aeroelasticity research at Boeing (previously McDonnell Douglas) Long Beach. The trim angle of attack is calculated for a range of desired lift values. In addition to the Newton's method algorithm, a non derivative method (NDM) based on fixed point iteration, typical of fixed angle of attack calculations in aeroelasticity, is employed. The NDM, which has been extended to be able to calculate trim angle of attack, is used for one of the cases. The Newton's method calculation converges in fewer iterations, but requires more CPU time than the NDM method. The NDM, however, results in a slightly different value of the trim angle of attack. It should be noted that NDM will converge in a larger number of iterations as the dynamic pressure increases.

For one value of the desired lift, both viscous and inviscid results were generated. The use of the inviscid flow model while not resulting in a markedly different value for the trim angle of attack, does result in a noticeable difference both in the wing deflection and the span loading when compared to the viscous results.

A crude (coarse-grain) parallel methodology was used in some of the calculations in this research. Although the codes were not parallelized, the use of modal superposition made it possible to compute the sensitivity terms on different processors of an IBM SP/2. This resulted in a decrease in wall clock time for these calculations. However, even with the parallel methodology, the CPU times involved may be prohibitive (approximately 5 days per Newton iteration) to any practical application of this method for wing analysis and design. Future work must concentrate on reducing these CPU times. Two possibilities: (i) The use of alternative basis vectors to further reduce the number of basis vectors used to represent the structural displacement, and (ii) The use of more efficient methods for obtaining the flow field sensitivities. The former will reduce the number of CFD analyses required the latter the CPU time per CFD analysis.

Acknowledgments

This work could not have been completed without the help of many people along my convoluted path towards graduation. First I would like to thank Dr. Rakesh K. Kapania for his help, advice and criticism as this research progressed. I would like to thank Dr. George Tzong of Boeing, Long Beach CA, under whom I began my research in aeroelasticity, and who introduced me to the trim problem that I took on and that eventually turned into my dissertation. Many thank must go to Drs. Grossman and Walters for their help, advice and guidance during my graduate school career. I would like to thank Erwin Sulaeman for his help where NASTRAN was involved in this work. I would also like to acknowledge the technical help and advice of my other two committee members, Drs. Schetz and Johnson.

Writing this up was facilitated by Team U.S.A.'s poor showing in Olympic hockey in Nagano. Without the distraction of having to be a patriot and watch my national team compete, I was able to direct more of my attention to my research. I would also like to thank my parents for their support along all stages of my education. Finally and most importantly, I would not have been able to complete this work without the love, support and motivation of my fiancee Andie DiCarlo. I hope I can be there for her as she was there for me.

Contents

List of Tables **x**

List of Figures **xv**

Nomenclature **xvi**

1 Introduction **1**

1.1 Multidisciplinary Analysis 1

1.2 Aeroelasticity 2

1.3 Previous Research 4

1.4 Aeroelastic Trim 11

1.5 Nonlinear Trim 12

2 Formulation **14**

2.1 Linear Aerodynamics 14

2.2 Non-Linear Aerodynamics 16

2.2.1 Structural Modeling 16

2.2.2 Derivation of Linearized Trim Equation 18

2.2.3 Trim Algorithm Using the Linearized Trim Equation 20

2.2.4 Extension to Multiple Trim Variables 22
2.3 Non Derivative Method Algorithm 23
2.3.1 Non Derivative Algorithm for Fixed Angle of Attack 24
2.4 Relaxation Algorithm for Trim Calculations 25
2.5 Trim Calculations for Rigid Wing 27

3 Data Transfer 30

3.1 Pressure Integration 31
3.2 Splining Deflections 31
3.3 Deflection Transfer in ADOP 32
3.4 Deflection Transfer in the Aeroelastic Research Wing (ARW) Calculations 32

4 Computational Aspects 38

4.1 Grid Convergence for Simple Wing 39

5 Simple Wing Results 47

5.1 Description of the Simple Wing Model 47
5.2 Cases run 48
5.3 Discussion 49
5.3.1 Newtons Method Trim Calculations 49
5.3.2 Fixed Angle of Attack Calculations 53
5.3.3 Non Derivative Trim Calculations 54
5.3.4 Viscous vs Inviscid Results 55

6 ARW Results **118**

6.1 ARW Description 118

6.2 Fixed Angle of Attack Results 119

6.3 ARW Trim Calculation 121

7 Conclusions **136**

Bibliography **139**

A Levels of Aerodynamic Modeling **147**

A.1 Navier-Stokes Equations 147

A.2 Reynolds-Averaged Navier-Stokes Equations 149

A.3 Thin Layer Navier-Stokes Equations 150

A.4 Euler Equations 151

A.5 Potential Flow 151

A.6 Grid Generation 153

B Modal Analysis **161**

C Numerical Aspects **164**

C.1 Newton's Method 164

C.2 Newtons Method for Systems of Equations 166

C.3 Non Derivative Method 168

C.4 Non Derivative Method for Systems of Equations 168

List of Tables

5.1 Aircraft Weight Comparison 56

5.2 Case Summary 57

5.3 Convergence history of the trim angle of attack 58

5.4 Convergence history of lift 59

5.5 Comparison between Rigid and Flexible Wing Results 60

5.6 The 20,000-lbs (20K) case 61

5.7 Convergence history of 40,000-lbs (40k) Case Using 6 Mode Shapes . 62

5.8 Non Derivative Trim Calculation for the 20,000 lbs Case 63

5.9 Convergence of Modal Amplitudes for 10K and 20K Cases 64

5.10 Convergence of Modal Amplitudes for 40K and 60K Cases 65

5.11 Convergence of Modal Amplitudes for 80K Case 66

5.12 Convergence of Modal Amplitudes for 6 Mode shape, 40K Case . . . 67

5.13 Non Derivative Static Aeroelastic Solution Starting From Rigid Wing, $\alpha = 1$, $M = 0.3$, $\omega = 1$ 68

5.14 Non Derivative Static Aeroelastic Solution starting from rigid wing, $\alpha = 1$, $M = 0.3$, $\omega = 0.5$ 69

5.15 Non Derivative Static Aeroelastic Solution Starting From Rigid Wing, $\alpha = 1$, $M = 0.8$, $\omega = 0.5$ 70

5.16 Non Derivative Static Aeroelastic Solution Starting From Rigid Wing, $\alpha = 1$, $M = 0.8$, $\omega = 0.4$ 71

5.17 Non Derivative Trim Calculation for 20K Case. $M = 0.8$, $\omega = 0.5$ . . 72

6.1 Convergence of Modal Amplitudes for Fixed Angle of Attack Calculation for ARW Wing, $\alpha = 1^0$ (Euler) 122

6.2 Convergence history of Trim Calculations for ARW Wing (Euler) . . 123

6.3 Convergence of Modal Amplitudes Trim Calculation for ARW Wing (Euler) 124

A.1 Hierarchial Approach to Computational Simulation in Support of Aerospace Design 155

List of Figures

2.1 Newton's Method Trim Algorithm 28

2.2 Non Derivative Trim Algorithm 29

3.1 CFD Grid Point i,j and Surrounding Cells and Grid Points 35

3.2 Stencil Used to Integrate Aerodynamic Pressure About CFD Grid Point i,j 36

3.3 ADOP Neglects Rotations About the z-axis for Deflection Transfer . 37

4.1 Residual Convergence for Typical CFD Calculation 41

4.2 Grid Convergence for the Simple Wing, Rigid, $\alpha = 1^0$ 42

4.3 Deflection Difference Between Fine and Ultra-fine Meshes 43

4.4 Definition of Twist and Bending 44

4.5 Pressure Coefficient Difference Between Fine and Ultra-fine Meshes at 85% Semi-Span 45

4.6 Spanload Comparison Between Fine and Ultra-Fine Meshes 46

5.1 Simple Wing Planform Geometry 73

5.2 Simple Wing Finite Element Model 74

5.3 Simple Wing Mode Shapes (Mode Shapes are solid grey) 75

5.4 Displacement Convergence for Newton's Method Trim Calculations . 76

5.5 Angle of Attack Convergence 77

5.6 C_L vs α for Flexible and Rigid Wing 78

5.7 Normalized Bending Shapes for all Trim Calculations for the Simple Wing 79

5.8 Normalized Twisting Shapes for all Trim Calculations for the Simple Wing 80

5.9 Adjusted Spanload Distribution for Trim Calculations 81

5.10 Bending Displacement Convergence for 10,000-lbs case, (Navier-Stokes, Newton's Method) 82

5.11 Angle of Twist Convergence for 10,000-lbs case (Navier-Stokes, Newton's Method) 83

5.12 Deflection Convergence of the 10,000-lbs case. (Deflections x 10) (Navier-Stokes, Newton's Method) 84

5.13 Bending Displacement Convergence for the 20,000-lbs case (Navier-Stokes, Newton's Method) 85

5.14 Angle of Twist Convergence for the 20,000-lbs case (Navier-Stokes, Newton's Method) 86

5.15 Deflection Convergence for the 20,000-lbs case (Navier-Stokes, Newton's Method) (Deflections x 10) 87

5.16 Bending Displacement Convergence for the 20,000-lbs case (Euler, Newton's Method) 88

5.17 Angle of Twist Convergence for the 20,000-lbs case (Euler, Newton's Method) 89

5.18 Deflection Convergence for the 20,000-lbs case (Euler, Newton's Method) (Deflections x 10) 90

5.19 Bending Displacement Convergence for the 40,000-lbs case (Navier-Stokes, Newton's Method) 91

5.20 Angle of Twist Convergence for the 40,000-lbs case (Navier-Stokes, Newton's Method) 92

5.21 Deflection Convergence for the 40,000-lbs case (Deflections x 4) (Navier-Stokes, Newton's Method) 93

5.22 Bending Displacement Convergence for the 60,000-lbs case (Navier-Stokes, Newton's Method) 94

5.23 Angle of Twist Convergence for the 60,000-lbs case (Navier-Stokes, Newton's Method) 95

5.24 Deflection Convergence for the 60,000-lbs case (Navier-Stokes, Newton's Method) 96

5.25 Bending Deflection Convergence for the 80,000-lbs case (Navier-Stokes, Newton's Method) 97

5.26 Angle of Twist Convergence for the 80,000-lbs case (Navier-Stokes, Newton's Method) 98

5.27 Deflection Convergence for the 80,000-lbs case (Navier-Stokes, Newton's Method) 99

5.28 Structural Convergence for Fixed α Calculations 100

5.29 Bending Displacement Convergence for $\alpha = 1$, $M = 0.3$, $\omega = 1.0$ . . . 101

5.30 Angle of Twist Convergence Using NDM for $\alpha = 1$, $M = 0.3$, $\omega = 1.0$ 102

5.31 Bending Displacement Convergence Using NDM for $\alpha = 1$, $M = 0.3$, $\omega = 0.5$ 103

5.32 Angle of Twist Convergence Using NDM for $\alpha = 1$, $M = 0.3$, $\omega = 0.5$ 104

5.33 Bending Displacement Convergence Using NDM for $\alpha = 1$, $M = 0.8$, $\omega = 0.5$ 105

5.34 Angle of Twist Convergence Using NDM for $\alpha = 1$, $M = 0.8$, $\omega = 0.5$ 106

5.35 Bending Displacement Convergence Using NDM for $\alpha = 1$, $M = 0.8$, $\omega = 0.4$ 107

5.36 Angle of Twist Convergence Using NDM for $\alpha = 1$, $M = 0.8$, $\omega = 0.4$ 108

5.37 Convergence of Non Derivative Trim Calculations 109

5.38 Bending Displacement Convergence for the 20,000-lbs Case (Euler, Non Derivative) 110

5.39 Angle of Twist Convergence for the 20,000-lbs Case (Euler, Non Derivative) 111

5.40 Deflection Convergence for the 20,000-lbs Case (Euler, Non Derivative) (Deflections x 10) 112

5.41 Spanwise Variation of the Bending Displacement for the 20,000-lbs Case 113

5.42 Spanwise Variation of the Angle of Twist for the 20,000-lbs Case . . 114

5.43 Pressure Coefficient at 80% Spanwise Location 115

5.44 Spanload Plot for the 20,000-lbs Case 116

5.45 Converged Wing Shapes for the 20,000 lbs cases (Deflections x 10) . 117

6.1 ARW Planform Geometry (all dimensions in inches) 125

6.2 ARW Finite Element Model 126

6.3 ARW Mode Shapes (Mode Shapes are solid Grey) 127

6.4 Convergence of the Structural Displacement of the ARW using NDM 128

6.5 ARW Front Spar Deflection 129

6.6 ARW Rear Spar Deflection 130

6.7 Section Lift Coefficient Variation along span for $\alpha = 1^0$ 131

6.8 C_p plot at 70.7 % spanwise location for $\alpha = 1^0$ 132

6.9 ARW Wing Deflection (Jig shape is solid grey) 133

6.10 ARW Chordwise Deflection at 70.0 % spanwise location 134

6.11 ARW Trim Calculation Structural Convergence 135

A.1 Comparison Between Viscous and Inviscid CFD Grids 156

A.2 Typical Grid for a Viscous Surface 157

A.3 Typical Discretization of a flow field 158

A.4 Hyperbolic Grid Generation 159

A.5 Elliptical Grid Generation 160

C.1 Newton's Method 170

C.2 Non Derivative Method (NDM) 171

Nomenclature

$[A]$	interpolation matrix from aerodynamic load coefficients to generalized forces
$[\bar{A}]$	sensitivity of the pressure field with respect to generalized deflections for linear aerodynamics
$[\bar{\bar{A}}]$	sensitivity of pressure field with respect to deflection for non-linear aerodynamics
a_0, a_1, a_2	coefficients in surface spline formulation
$\{a\}$	aerodynamic load coefficients
$\{c\}$	displacement vector
E	error between desired and actual lift
F, G, H	flux vectors
$\{F\}$	aerodynamic Loads
F_i	coefficient in surface spline formulation
$\vec{F}$	aerodynamic force due to integrated pressure
J	Jacobian
$[K]$	stiffness matrix
$\{L\}^T$	vector of Gaussian integration coefficients
$[M]$	mass matrix
n	load factor
$\hat{n}$	unit normal vector
$\{Q\}$	generalized forces
Q	vector of conserved aerodynamic variables

$\{p\}$	vector or surface pressure
$[R]$	interpolation matrix from pressure to aerodynamic load coefficients
R_{ij}	term in surface spline matrix
r_{ij}	displacement between the ith and the jth points in splining formulation
r_z	offset distance in ADOP data transfer
S	CFD grid cell area
u, v, w	x, y and z displacement in ADOP
u, v, w	x, y and z velocity in Navier-Stokes equations
$\vec{V}$	velocity
W	aircraft weight
α	angle of attack
ε	tolerance
η, ξ, ζ	logical coordinates
$[\Lambda]$	diagonal matrix of eigenvalues
λ_i	ith eigenvalue
μ	coefficient of viscosity
$[\Phi]$	matrix of mode shapes
ϕ_i	ith mode shape
ϕ	velocity potential function
$\{\phi_{PL}\}^T$	integration vector to convert aerodynamic loads to lift
$\{\psi_M\}^T$	integration vector to convert aerodynamic loads to moments
ρ	density
θ	rotation
ω	relaxation factor

Chapter 1

Introduction

1.1 Multidisciplinary Analysis

Currently, a great deal of effort is being directed in aerospace and other branches of engineering towards problems that involve interaction among different disciplines. It is necessary to incorporate controls, propulsion, structures, aerodynamics, and other areas into the design of aerospace vehicles.[1] This is only logical, since all areas affect and are affected by the others. For example, where the engines are placed on the airframe greatly affects the aerodynamics of the vehicle, the structures and the controls.

However until recently, the computational state of the art was such that it was not feasible to consider all aspects of vehicle design concurrently. Since faster and more powerful computers have become available over the past decade, it has become possible to consider many disciplines together in the preliminary design phase of vehicles. Even cost is now a consideration in the preliminary design phase of engineering. In addition sophisticated optimization algorithms are available with which one can consider many variables while designing vehicles.

Oloso and Taylor[2] do not perform a multidisciplinary analysis *per se*, but they do

give a good example of design and optimization issues in aerodynamic design. The authors optimize a High Speed Civil Transport (HSCT) geometry with 60 variables using the Computational Fluid Dynamics code CFL3D to solve the Euler equations. The authors solve the problem on a parallel platform, the IBM SP/2; thus demonstrating another aid to modern aeroelastic analysis, the use of parallel computations. Bhardwaj[3,4] also demonstrated a parallel methodology for aeroelastic calculations. Aeroelasticity is ideally suited to parallel computing since the aerodynamic and structural calculations can be made simultaneously, although a bottleneck occurs when data is transmitted between the structural and aerodynamic calculations.

Representative significant multidisciplinary design efforts, for an HSCT configuration, are Knill *et al.*[5] and Giunta *et al.*[6] Although those references deal with specific aspects of the optimization and design phase, they reflect a much larger attempt to develop a methodology to incorporate many disciplines into the design process in a practical way. Tyll *et al.*[7] presents a design methodology for MAGLEV trains that takes aerodynamics and cost into effect.

1.2 Aeroelasticity

One of the older fields of multidisciplinary interactions in aerospace engineering is Aeroelasticity, the study of the interaction between fluids and structures. It is not just something that comes into play only in the design and analysis of airplanes. Aeroelastic effects are visible everywhere. A pedestrian can watch a stop sign flutter in the wind and in the wake of the cars driving by. On a stormy day, one can watch the trees outside sway in the wind. A tourist on top of the Eiffel tower can watch the shadow cast by the tower move back and forth on the river Seine as the tower moves in the Paris breeze. On a more catastrophic note, most engineering students have seen the film of the Tacoma Narrows Bridge disaster. The bridge collapsed as a result of stall-flutter(Fung[8] p. 60). Aeroelastic calculations are now considered vital

to the design of tall buildings and bridges as well as that of aircraft.

This research centers around aeroelasticity as it applies to aircraft wings. Simply stated, the problem is as follows: the aerodynamic loads are dependent upon the geometry of the wing and are therefore dependent upon the structural deformation of the wing. The structural deformation is a function of the aerodynamic loads.

There are other aspects to the aeroelasticity of aircraft wings such as flutter and divergence. Flutter is a dynamic instability of the wing which occurs at a critical speed and results in a dynamic instability. Divergence is a static instability whereby near a critical speed, the aerodynamic moment exerted on the wing becomes too great for the elastic moment to compensate for resulting in large angles of twist(Fung[8] pp. 81,161).

Computationally, aeroelastic calculations are comprised of three parts. The first two parts seem obvious. One needs to be able to solve the aerodynamic problem and the structural problem. The third part of the problem is integrating the structural and aerodynamic calculations.

There are two fundamental approaches to computational aeroelasticity. The first is to use an integrated code such as the NASA Ames code ENSAERO[9] where both the structures and the aerodynamic modules are combined into one integrated code and all coupling is internal to the code. ENSAERO,[9] which stands for Euler/ Navier Stokes Aeroelastic code, contains a Computational Fluid Dynamics module capable of solving either the Euler or the Navier-Stokes equations, and a Plate Finite Element code along with data coupling routines, and grid generation routines for the CFD module. A second approach that seems to be more common is to use off–the–shelf aerodynamics codes, and available structures codes and a separate coupling modules to pass data between the structures code and the aerodynamics code.

Another issue is the relative complexity of the aerodynamic and structural models. Everything from a simple beam model to an elaborate finite element model can be

used for the structures, and everything from a simple panel code to a full Navier-Stokes representation can be, and has been used for aerodynamic modeling in CFD analysis for aeroelastic modeling. It is one's approach to these issues, and to the problem of coupling the aeroelastic and structural model, that define a solution to an aeroelastic problem.

1.3 Previous Research

Bhardwaj[3] (see also Kapania and Bhardwaj[10]) presents an overview of an aeroelastic methodology incorporating high end structural and aerodynamic models. His research uses NASTD to solve the Euler equations, and ENSAERO to solve the Navier-Stokes equations for modeling the aerodynamics and using NASTRAN and a Finite Element code developed for that research by Bhardwaj to model the structures. For data transfer, the splining method by Harder and Desmarais[11] is used to translate deflections from the structural code to the aerodynamic grid. For translating loads from the aerodynamics model to the structural model, Bhardwaj developed a method for translating forces based on area coordinates that works well. Results are presented for an F/A-18 Stabilator, the movable horizontal tail of that aircraft, and for the Aeroelastic Research Wing (ARW).[12]

MacMurdy[13] also presents a methodology for coupling the Navier-Stokes equations with finite element structural models within the code ENSAERO. A further discussion of the coupling methodology is continued by MacMurdy.[14] (See also McMurdy, Guruswamy and Kapania[15]).

Tzong *et al.*[16] use the McDonnel Douglas/Boeing code ADOP (Aeroelastic Design Optimization Program)[17] to analyze a simple wing, the same wing used in the bulk of this research, and to analyze an MD-90 wing. ADOP is a structural optimization code designed specifically for aircraft structures. It does not contain an aerodynamic model, but it is designed to handle input from both CFD and panel

codes. OVERFLOW[18] is used to generate the aerodynamic data, solving the Thin Layer Navier Stokes equations. The issue of data transfer is dealt with extensively in the paper of Tzong *et al.* and the transfer methodology for ADOP is discussed. Tzong *et al.* present force and moment data for both the simple wing and the MD-90-wing. Results for the simple wing force coefficients are compared for rigid and flexible conditions and a comparison is made between the use of linear aerodynamics and CFD. The results in this paper show typically about a 3 percent difference in load results when using linear and non-linear aerodynamics. In aircraft design, this is a significant difference, but the decrease in CPU time involved in solving simpler aerodynamic codes is also significant. The authors in this case speculate that the difference between results from linear and non-linear aerodynamics may increase for complex aerodynamic geometries that can be handled by CFD much better than by linear codes.

Tzong *et al.*[19] continued using ADOP to demonstrate a modal analysis of aircraft structures. Results are presented for natural frequencies for various test cases ranging from a cantilevered plate to the inboard flap of a transport wing. ADOP results are compared with NASTRAN[20] results a and good agreement is presented. In addition, the authors in this case derive an advanced subspace iteration technique to perform structural calculations. Sikes *et al.*[21] further demonstrate the use of ADOP. In this case, a modal analysis is used to model the structure, and a doublet lattice method is used for the aerodynamics. The authors investigate flutter optimization of transport wings. The authors also emphasize the multidisciplinary nature of the analysis.

Schuster *et al.*[22] use the full Navier Stokes equations in the static analysis of a fighter aircraft configuration. A linear structural model is used. The purpose of the study was to perform an aeroelastic analysis of the full configuration of a vehicle where the flow field contains instances of vortices, separated flow and unsteady flow. Experimental data was available to the authors, and the computational results are compared favorably to the experimental data. The authors demonstrate how the

control surfaces on the fighter geometry can be designed to deflect into favorable geometries for the aerodynamics, and for aeroelastic effects. Fatigue analysis is also discussed. Fatigue as a result of buffeting from burst vortices can reduce the surface life of the tail, and accurate structural analysis of the wing under unsteady aerodynamic loads is necessary to adequately study the aeroelastic behaviour of the aircraft. For such problems, the full Navier Stokes equations that model viscous effects must be used. The Euler equations are not adequate, and linear methods certainly are not accurate enough. For structural modeling, a modal analysis was used. For the CFD, the code ENS3d was used, solving the Reynolds Averaged Navier Stokes (RANS) equations (See Appendix A). Grid generation was performed using a zonal hybrid Algebraic/Parabolic/Elliptic grid generator. A Baldwin-Lomax turbulence model is used in the RANS calculations. The CFD analysis does not seem to adequately capture a massive upper surface separation. The authors attribute this to the use of the Baldwin-Lomax turbulence model which according to the authors over predicts the turbulence quantities resulting in the flow remaining attached longer than is seen in experimental results.

In the research by Hooker *et al.*,[23] a study of different levels of structural modeling is performed, along with an extensive experimental validation. Coupled with the CFD code CFL3D,[24] Hooker *et al* use the finite element capabilities of ADOP[17] that is very similar to NASTRAN[20] to model the structure. In addition, a 1-D beam model is also used. The advantage being fast turnaround time and simple grid generation albeit with a loss of accuracy.

Purcell *et al.*[25] use a loose coupling between the CFD and FEM codes. By loose coupling, it is meant that there is no direct integration between the aerodynamic and structural models. Any CFD code could be used, along with any FEM code. Emphasizing that the use of "empirically modified linear aerodynamics"[25] is the rule in computational aeroelasticity more often than not, Purcel *et al.* point out that the use of CFD is crucial when no experimental data is available. The use of simplified

structural models vs. high fidelity complex FEM models is investigated as is the use of Wind Tunnel data for validation or aeroelastic data rather than modification of codes. The CFD codes FLO27 and FLO28 are used for CFD, and the ELFINI[26] finite element code is used. The analysis is performed on a Boeing 747-200 wing model, and the results are compared with available experimental data

Nathman and Barton[27] use the structural optimization code ASTROS[28] along with the linear panel aerodynamics code USSAERO[29] in addition to the structured multi-grid Euler code MGAERO.[30] This reseach demonstrates another important aspect of aeroelastic calculations, and that is the modular nature of the computational side of aeroelasticity. Either USSAERO or MGAERO can be used. Also Nathman and Barton demonstrate the necessity of using at least the Euler equations for examining control reversal in the transonic regime. The authors in this paper demonstrate that panel codes aren't able to adequately analyze the aerodynamics of control reversal when compressible effects are present.

Newman *et al.*[31] demonstrate another aspect of Computational Fluid Dynamics that may be ideally suited for aeroelasticity; an unstructured grid. The aerodynamic forces generated by the Euler equations are applied to the jig shape of the wing. The jig shape is the shape of the wing under just body forces, the shape of the wing as the plane is sitting on the runway. The possible advantage of using unstructured CFD is in grid generation, and its comparative ease in handling complex geometry. If one wants to calculate a wing with a strut,[32] or a wing with deflected flaps, it could prove to be a problem generating the surface geometry using structured grid technology. Newman *et al.*[33] define a virtual surface between the CFD model and the Finite Element model and use this to translate loads and deflections back and forth between the FEM model and the CFD grid. This virtual surface approach was developed by Guruswamy and Byun.[34] A virtual surface is defined between the CFD surface grid and the FEM mesh. The virtual surface is discretized using finite elements distinct from the elements used in structural modeling. A mapping

matrix, developed by Appa,[35] is used to transfer data between the fluid and structural interface boundaries.

Byun and Guruswamy[36] describe the code ENSAERO[9] that they have developed. ENSAERO is a modularized aeroelastic code that contains a CFD model that can solve either the Euler or the Navier Stokes Equations and contains a Finite Element solver for the structures. The grid generator defines the surface in terms of aerodynamic variables such as the airfoil section, taper and twist.

Robinson *et al.*[37] use the NASA Langley code CFL3D[24] to solve the Euler equations to perform aeroelastic analysis of a test case wing. The wing used is a simple model, untapered, untwisted with a NACA 0012 section, swept back 45 degrees. Flutter analysis is performed, and compared with available experimental data. The authors use a deforming mesh algorithm, and examples are given of various meshes and results. A modal analysis is used for the structural model. CFL3D has time accurate capability using a three factor implicit, finite-volume algorithm. CFL3D includes unsteady grid metric terms needed for time accurate calculations with moving meshes. Robinson *et al.* have included terms to account for deforming meshes as well as translating grids. The deforming mesh algorithm in this work is similar to that by Batina[38,39] on unstructured meshes. Batina deforms the grid triangles and tetrahedrons by modeling each node as a spring and he demonstrates this in 2D on a NACA 0012 airfoil[38] and on complex 3-D geometries.[39]

Kousen and Bendiksen[40] perform an aeroelastic analysis of flutter behavior of a typical 2-D airfoil section using the Euler equations. Aerodynamic nonlinearities can result in limit cycle behaviour. The authors investigate the effects of freeplay on the limit cycle behaviour at transonic Mach numbers. NACA 64A010 and NACA 64A006 sections are used in this study.

Karpel and Brainin[41] discuss the use of stress considerations in aeroelastic optimization. A modal approach to structures is used in design routines. The authors

found that 10-20 modes were necessary in optimization calculations with regard to divergence and control effectiveness and 20-30 modes were used for static aeroelastic optimization. Tzong *et al.*[19] demonstrated that 8 mode shapes were adequate for aeroelastic analysis of transport wings.

A significant amount of research has been performed in the use of an equivalent plate model in aeroelastic analysis. The equivalent plate model was developed by Giles.[42,43] The objective is to develop a simplified plate-type model that can simulate the behaviour of a more complex structure, and the author has achieved some degree of success. The structural properties of an equivalent plate model are further investigated by Kapania and Lovejoy.[44]

When the aerodynamics is modeled using Computational Fluid Dynamics solving either the Euler Equations or some version of the Navier Stokes Equations, a central issue is the grid generation. There are two ways to approach grid generation for aeroelastic calculations. The first is to generate an initial volume grid, and then modify that grid as the surface deflects[3,9] without completely regenerating the volume grid each time the wing deflects. This is probably the simplest way to approach this problem. The second method is to completely regenerate the grid as the surface geometry changes at each iteration.

In the research presented in this dissertation, the second method was used. The surface grid was re-defined as the wing was deflected, and the volume grid was re-generated. This problem was made much easier through the use of a hyperbolic grid generator. Numerical grid generators solve partial differential equations to generate the volume grid that discretizes the flow domain for the CFD code. Many grid generators such as the very successful GRIDGEN[45,46] package use elliptic solvers to generate volume grids. To solve an elliptic partial differential equation numerically to generate a volume grid, the user must explicitly define all of the boundaries. Practically this means generating the surface grid for all 6 numerical boundaries. This can be a time consuming process. In solving a hyperbolic partial differential equation,

the grid generator can solve the PDE through a marching algorithm. The user has to only define the wing surface, and the solution of the grid generator marches, outward from the wing surface, based on spacing parameters and boundary conditions. A grid generator of this type is ideally suited for aeroelastic calculations because the user has to explicitly define only the CFD grid on the surface of the wing.

The issue of data transfer is made more complicated by the fact that most of the time the Aerodynamic grid and the Structural model are not exactly coincident, some sort of interpolation is needed. If the CFD is used to simulate the flow, the aerodynamic grid is normally more dense than the structural discretization.

Appa *et al.*[47]present a method to spline deflections and loads back and forth between the CFD and FE grids based on the piecewise cubic monotonic interpolation scheme developed by Fritsch and Carlson.[48] Harder and Desmarais[11] present an interpolation scheme based on small deflections of an infinite beam. Appa[35] presents another method based on an infinite plate representation. Since a closed form solution for this problem is available for the problem as postulated, this method is extremely attractive. Pidaparti[49] presents an isoparametric mapping based on isoparametric finite elements. This method can be extended to control surfaces or more complex geometry than just a simple wing. Smith *et al.*[50] present a comprehensive survey of interfacing techniques for aeroelastic use.

Bhardwaj[3,10] presents a coupling methodology for aeroelastic analysis. Using the surface spline of Harder and Desmarais[11] to translate the deflections from the structural to the aerodynamic grids. Bhardwaj developed a technique based on area coordinates to translate forces from pressure data on the aerodynamic model to structural loads.

1.4 Aeroelastic Trim

An important aspect of the aeroelastic analysis of a wing is the determination of the trimmed condition. To analyze wing performance during maneuvers or during straight and level flight, the amount of lift that the wing needs to generate must be determined, and the correct angle of attack must be used. To use a simple example, consider straight and level flight. If the wing is being analyzed for a specific maneuver, then there is a specific amount of lift the wing must generate to maintain that maneuver. The problem is to simultaneously determine the angle of attack and the deflection for which the desired lift is generated. For a rigid wing, it is simple. Lift is a function of the angle of attack, and one need only to know the lift-curve slope of the wing. For a flexible wing, the problem is not that simple. As lift increases, obviously so do the aerodynamic pressures that act on the structure of the wing, and the wing deforms more. As the geometry changes, the loads and the lift on the wing both change. Again, the problem is non-linear unless one can determine explicitly the variation of the loads on the wing as a function of the geometry.

Kapania *et al.*[51] derive an algorithm to calculate the trimmed condition of a wing using linear aerodynamics. The explicit dependence of the pressure field on the geometry is needed, and this is available through the use of linear aerodynamics. Baker an D'Vari[52] also derive an aeroelastic analysis using ADOP[17] to analyze a complete configuration. Trim considerations are included. Again, specific information about the dependence of the aerodynamic loads with respect to the geometry is needed. The authors call these sensitivities "Aerodynamic Influence Coefficients" and this algorithm is limited to linear aerodynamics.

Though the problem is normally posed as a problem of simultaneously determining the angle of attack and deflection corresponding to a given lift, physically, the problem is also dependent on more than just the angle of attack. The wing's control surfaces also play a role in determining the trimmed state of the wing, and one is trimming

the wing for more than just lift. For certain maneuvers, the aircraft trimmed state may involve a specific moment as well. For this research, angle of attack has been considered to be the only trim variable. A discussion of the extension of the algorithm to include more variables to achieve different trim conditions is included.

1.5 Nonlinear Trim

Previously, no methodology has been available to calculate trim angle of attack using CFD. The purpose of this research is to derive an algorithm that can be used to calculate aeroelastic trim using CFD. A Newton's method type algorithm is derived in chapter 2 for calculating the trimmed condition. In addition, a non derivative method (NDM) based on fixed point iteration is also derived in chapter 2 that is a common algorithm for the calculation of fixed angle of attack aeroelastic solutions. This NDM algorithm is extended to calculate the trimmed condition for purposes of comparison with the Newton's method algorithm.

Chapter 2 details the derivation of the trim algorithm, as well as the description of a typical fixed point scheme for use in aeroelastic analysis. Chapter 3 describes the aeroelastic coupling techniques used in this research. Chapter 4 includes details of the computational aspects of this work. Grid convergence for the simple wing is presented as are details of the CPU times required and the computer platforms that this research utilized.

Two wing models were used in this research. A simple wing model was used for trim calculations. Chapter 5 presents the results for the simple wing. Chapter 6 presents results for the Aeroelastic Research Wing (ARW). The ARW is a research wing for which both experimental and computational data is available. Results are used to evaluate the modal approach to structural modeling. Inviscid and viscous results are compared.

The appendices include an overview of the levels of aerodynamic modeling pertinent to this research, an overview of modal analysis in structures and a discussion of the fundamental differences between Newton's method and the NDM algorithm employed herein.

Chapter 2

Formulation

2.1 Linear Aerodynamics

Kapania *et al.*[51] describe a method of simultaneously determining the deflection and the trim angle of attack for a flexible wing using linear aerodynamics.

This algorithm begins with expressing the aerodynamic pressure, $\{p\}$, over the surface of the wing as

$$\{p\} = [\bar{A}]\{c\} + \alpha\{\frac{\partial p}{\partial \alpha}\} \tag{2.1}$$

where $\{c\}$ is the deflection of the wing, α is the angle of attack and

$$\bar{A}_{ij} = \frac{\partial p_i}{\partial C_j} \tag{2.2}$$

where p_i is the aerodynamic pressure at the ith generalized coordinate of the wing and C_j is the deflection of the jth coordinate on the wing.

Kapania *et al.* use Chebyshev polynomials to form an interpolation matrix, $[R]$ to interpolate aerodynamic pressures $\{p\}$ to structural generalized loads, $\{a\}$.

$$\{a\} = [R]\{p\} \tag{2.3}$$

Kapania *et al.* express structural equilibrium as

$$[K]\{c\} = [A][R][\bar{A}]\{c\} + \alpha\{L\}^T[R]\left\{\frac{\partial p}{\partial \alpha}\right\} \tag{2.4}$$

where $\{L\}^T$ is a vector of Gaussian integration coefficients to integrate the forces $\{a\}$ to obtain lift. $[A]$ is an interpolation matrix to convert aerodynamic load coefficients from the linear aerodynamics code to generalized forces. The equation for lift can be written as

$$\frac{nW}{2} = \{L\}^T\{a\} \tag{2.5}$$

where n is the load factor, and W is the weight of the aircraft.

Combining equations 2.1 and 2.3 with 2.5 results in the trim equation.

$$\frac{nW}{2} = \{L\}^T[R][\bar{A}]\{c\} + \alpha\{L\}^T[R]\left\{\frac{\partial p}{\partial \alpha}\right\} \tag{2.6}$$

Combining 2.4 with 2.6 results in the governing equation to simultaneously determine deflection and angle of attack for the case of linear aerodynamics.[51]

$$\begin{bmatrix} [K] - [A]\frac{\partial\{a\}}{\partial\{c\}} & [A]\frac{\partial\{a\}}{\partial\alpha} \\ \{L\}^T\left[\frac{\partial\{a\}}{\partial\{c\}}\right] & \{L\}^T\frac{\partial\{a\}}{\partial\alpha} \end{bmatrix} \begin{Bmatrix} c \\ \alpha \end{Bmatrix} = \begin{Bmatrix} 0 \\ \frac{nW}{2} \end{Bmatrix} \tag{2.7}$$

Note that for linear aerodynamics, the derivatives of the load terms with respect to displacement and angle of attack can be calculated explicitly and no iteration is necessary.

D'Vari and Baker[52] present a similar method of calculating the trimmed condition of an aircraft for multiple trim variables. This is done as a part of a larger design and optimization algorithm. Again, the methodology developed by D'Vari and Baker is contingent upon knowing what they term as "Theoretical Aerodynamic Influence Coefficients", explicitly given from linear aerodynamics. These are similar to the explicitly calculated sensitivities mentioned as $[\bar{A}]_{ij}$ in the work of Kapania *et al.*[51]

2.2 Non-Linear Aerodynamics

The method of Kapania *et al.* can not be easily extended for non- linear aerodynamics. The problem term is the derivative of the pressure field over the wing with respect to the deflection of the wing. This term cannot be calculated analytically in this case, and there is no direct way to numerically calculate the term in a fashion that will not be prohibitively expensive, especially if one is working with a finite element model of the wing.

However, using mode shapes to represent the structural deflection as a set of resuded bases makes the numerical calculation of this term using CFD a reasonable proposition. A discussion of the use of mode shapes is given in Appendix B. For a structural model using N mode shapes, it would take N+1 aerodynamic solutions to calculate the sensitivity of the pressure with respect to each of the generalized coordinates. One baseline undeflected solution, and one solution for each mode shape with that mode shape deflected by unity amplitude. The value of N is generally on the order of ten whereas an FEM model may have tens of thousands of generalized coordinates (degrees-of-freedom).[53]

2.2.1 Structural Modeling

Beginning with a modal representation of the deflection of the wing

$$[K]\{c\} = \{F\} \tag{2.8}$$

where the deflection $\{c\}$ is represented as a linear combination of the mode shapes.

$$\{c\} = [\Phi]\{q\} \tag{2.9}$$

Where $\{q\}$ is the vector of modal amplitudes and $[\Phi]$ is the matrix of mode shapes of the wing under consideration

$$[\Phi] = [\phi_1, \phi_2, \phi_3 \dots \phi_n] \tag{2.10}$$

so

$$[K]\{\Phi\}[q] = \{F\} \tag{2.11}$$

premultiplying by $[\Phi]^T$

$$[\Phi]^T[K]\{\Phi\}[q] = [\Phi]^T\{F\} \tag{2.12}$$

which simplifies to

$$[\Lambda]\{q\} = \{Q\} \tag{2.13}$$

where $[\Lambda]$ is the diagonal matrix of eigenvalues, q is the vector of modal amplitudes and the generalized force, $\{Q\}$ is given by

$$\{Q\} = [\Phi]^T\{F\} \tag{2.14}$$

Equation 2.13 the structural model.

2.2.2 Derivation of Linearized Trim Equation

The change in aerodynamic forces on the wing $\{\Delta F\}$ can be represented as

$$\{\Delta F\} = \{F_\alpha\}\Delta\alpha + \Sigma_{i=1}^{N}\{F_i\}\Delta q_i \tag{2.15}$$

or

$$\{\Delta F\} = [F_i \dots F_n | F_\alpha] \left\{ \begin{array}{c} \{\Delta q\} \\ \\ \Delta\alpha \end{array} \right\} \tag{2.16}$$

where F_α is the force due to a unit change in α and F_i is the vector of aerodynamic forces due to a unit change in the ith mode shape.

Substituting Equation 2.11 in for $\{\Delta F\}$

$$[K][\Phi]\{\Delta q\} = [F_i \dots F_n | F_\alpha] \left\{ \begin{array}{c} \{\Delta q\} \\ \\ \Delta\alpha \end{array} \right\} \tag{2.17}$$

or

$$[K][\Phi]\{\Delta q\} = [\overline{\overline{A}}]\{\Delta q\} + \{F_\alpha\}\Delta\alpha \tag{2.18}$$

where $[\overline{\overline{A}}]$ is a matrix whose columns are made up of the F_i terms.

$$[\overline{\overline{A}}] = [F_i \dots F_n] \tag{2.19}$$

$[\overline{\overline{A}}]$ is the sensitivity of the pressure field with respect to the deflection. Premultiplying by $[\Phi]^T$

$$\left([\Phi]^T[K][\Phi] - [\Phi]^T[\overline{\overline{A}}]\right)\{\Delta q\} - [\Phi]^T\{F_\alpha\}\Delta\alpha = 0 \tag{2.20}$$

$$([\Lambda] - [Q_M])\{\Delta q\} - \{Q\}_\alpha \Delta\alpha = 0 \tag{2.21}$$

where

$$[Q_M] = [\Phi]^T[\overline{\overline{A}}] \tag{2.22}$$

and

$$\{Q\}_\alpha = [\Phi]^T\{F_\alpha\} \tag{2.23}$$

Change in lift due to a change in aerodynamic force can be expressed as

$$\Delta L = \{\phi_{PL}\}^T\{\Delta F\} \tag{2.24}$$

Where $\{\phi_{PL}\}^T$ is an integrating factor applied to the aerodynamic force vector to calculate lift. In effect $\Delta L = \Sigma\Delta F_z$ where $\{\phi_{PL}\}^T = \{0, 0, 1, 0, 0, 1 \ldots 0, 0, 1\}$ assuming that lift is in the $+z$ direction. In this case, $\{\phi_{PL}\}^T$ is analogous to $\{L\}^T$ in the linear trim analysis above.

Substituting for $\{\Delta F\}$

$$\{\phi_{PL}\}^T[\overline{\overline{A}}]\{\Delta q\} + \{\phi_{PL}\}^T\{F_\alpha\}\Delta\alpha = \Delta L \tag{2.25}$$

Combining equation 2.20 with equation 2.25 results in the Linearized Trim Equation

$$\begin{bmatrix} ([\Lambda] - [Q_M]) & \{Q_\alpha\} \\ \{\phi_{PL}\}^T[\overline{\overline{A}}] & \{\phi_{PL}\}^T\{F_\alpha\} \end{bmatrix} \begin{Bmatrix} \{\Delta q\} \\ \Delta\alpha \end{Bmatrix} = \begin{Bmatrix} \{0\} \\ \Delta L \end{Bmatrix} \tag{2.26}$$

2.2.3 Trim Algorithm Using the Linearized Trim Equation

Initially, the wing is undeflected, and for the first iteration, aerodynamic calculations are made at $\alpha = \alpha_0$. ΔL is set at $nW/2 - L_{\alpha=\alpha_0}$. Note that if the wing being analyzed is symmetric, then ΔL can be set at $nW/2$ if $\alpha_0 = 0$. Including the load factor n allows different maneuvers to be analyzed. The weight represented by W is the weight of the aircraft.

$[\Lambda]$ and $[\Phi]$ are calculated from the FEM model of the wing. These are one time calculations for each wing to be analyzed, and do not change when changing flight conditions.

The iterative cycle is explained below. (Figure 2.1)

1. Matrices $[Q_M]$, $\{Q_\alpha\}$, $[\overline{\overline{A}}]$ and $\{F_\alpha\}$ are calculated from the CFD model of the wing at the current value of α_{trim}.

2. $[Q_M]$ and $[\overline{\overline{A}}]$ are calculated by deflecting each mode by unit amplitude, and solving for the aerodynamic loads on the wing at the flight conditions at which the wing is being analyzed. The loads on the undeflected wing are then calculated at the same flight conditions. $[\overline{\overline{A}}]$ is the difference in the loads due to the deflected and undeflected wing.

$$[Q_M] = [\Phi]^T[\overline{\overline{A}}]$$

3. Matrix $\{Q_\alpha\}$ is calculated by solving for the loads at an angle of attack $\alpha = \alpha + \Delta\alpha$ of the undeflected wing, subtracting out the loads of the undeflected wing at the current α_{trim}, and dividing by $\Delta\alpha$.

4. The Linear trim equation is then solved for $\{\Delta q\}$ and for $\Delta\alpha$

5. The trim angle of attack α and the displacement vector $\{q\}$ are adjusted as

$$\alpha_{trim}^{n+1} = \alpha_{trim}^{n} + \Delta\alpha$$

and

$$\{q\}^{n+1} = \{q\}^{n} + \{\Delta q\}$$

The deflected geometry is then generated based on the resulting $\{q\}$ from the above calculation.

6. A CFD solution is run at the new α_{trim} with the deflected geometry, and the lift on the wing is calculated by integrating the pressure. Convergence is based on the error in the lift calculations. For purposes here, the error is defined as the discrepancy between the lift needed and the lift generated. It is expressed as a percentage.

$$E = 100\frac{|\frac{nw}{2} - L|}{L} \tag{2.27}$$

If

$$E < \varepsilon \tag{2.28}$$

where ε is a prescribed tolerance, then the problem solved, otherwise, the cycle is repeated.

2.2.4 Extension to Multiple Trim Variables

Extension of this method to multiple trim variables is trivial. To include a variable, x as a new variable under consideration for trim calculations, one would need to re-formulate the change in force from equation 2.15 as

$$\{\Delta F\} = \{F_\alpha\}\Delta\alpha + \Sigma\{F_i\}\Delta q_i + \{F_x\}\Delta x \tag{2.29}$$

Equation 2.25 becomes

$$\{\phi_{PL}\}^T[\overline{\overline{A}}]\{\Delta q\} + \{\phi_{PL}\}^T\{F_\alpha\}\Delta\alpha + \{\phi_{PL}\}^T\{F_x\}\Delta x = \Delta L \tag{2.30}$$

and 2.20 becomes

$$\left([\Phi]^T[K][\Phi] - [\Phi]^T[\overline{\overline{A}}]\right)\{\Delta q\} - [\Phi]^T\{F_\alpha\}\Delta\alpha - [\Phi]^T\{F_x\}\Delta x = 0 \tag{2.31}$$

However, since an additional variable has entered the problem, a third equation is needed. The third equation would depend on the new variable. A likely choice for an additional trim variable would be a control surface deflection. In this case, a possible additional equation would be a moment balance.

If the moment M due to a vector of aerodynamic forces $\{F\}$ can be expressed as $M = \{\psi_M\}^T\{F\}$, where $\{\psi_M\}^T$ is analogous to $\{\phi_{PL}\}^T$ and is a vector of integrating coefficients to convert the aerodynamic loads to a moment about a specific point, then the moment balance equation would be

$$\{\psi_M\}^T[\overline{\overline{A}}]\{\Delta q\} + \{\psi_M\}^T\{F_\alpha\}\Delta\alpha + \{\psi_M\}^T\{F_x\}\Delta x = \Delta L \tag{2.32}$$

This would result in the new linear trim equation

$$\begin{bmatrix} ([\Lambda]-[Q_M]) & \{Q_\alpha\} & \{Q_x\} \\ \{\phi_{PL}\}^T[\overline{\overline{A}}] & \{\phi_{PL}\}^T\{F_\alpha\} & \{\phi_{PL}\}^T\{F_x\} \\ \{\psi_M\}^T[\overline{\overline{A}}] & \{\psi_M\}^T\{F_\alpha\} & \{\psi_M\}^T\{F_x\} \end{bmatrix} \begin{Bmatrix} \{\Delta q\} \\ \Delta\alpha \\ \Delta x \end{Bmatrix} = \begin{Bmatrix} \{0\} \\ \Delta L \\ 0 \end{Bmatrix} \tag{2.33}$$

Additional trim variables could be added to the formulation in a similar manner.

2.3 Non Derivative Method Algorithm

One of the most common ways to calculate the deflection of a flexible wing is to use a non derivative Fixed-Point Iteration technique, since these techniques are relatively simple to implement. Typically, the aerodynamic loads would be calculated based on whatever aerodynamics code is being used. The deflections from the aerodynamic loads would be calculated based on the structural model of the wing. The loads are then re-calculated based on the new geometry of the wing. As the solution converges, the change in deflection between iterations approaches zero. A typical Fixed Point equation can be expressed as

$$F(x) = x \tag{2.34}$$

For an aeroelastic calculation, the form of the Fixed Point problem is that the aerodynamic loads given from the solution of the flow field will deflect the wing the same amount as the initial deflection that resulted in the aerodynamic loads. In mathematical form, the Fixed Point equation for aeroelasticity can be expressed as

$$c(\{F\}_i) = c_i \tag{2.35}$$

where $\{F\}_i$ are the aerodynamic loads that result from a deflection of c_i.

In the research presented here, two types of non derivative calculations were performed. Fixed angle of attack calculations and Trim calculations. Under-relaxation was used to facilitate convergence.

Beginning with the structural model 2.13

$$[\Lambda]\{q\} = \{Q\} \tag{2.36}$$

where

$$\{Q\} = [\Phi]^T\{F\} \tag{2.37}$$

Equation 2.37 is the structural model of this formulation.

Note that

$$q_i = Q_i/\lambda_i \tag{2.38}$$

where λ_i is the ith eigenvalue, or the square of the natural frequency corresponding to the ith mode shape.

2.3.1 Non Derivative Algorithm for Fixed Angle of Attack

Initially the wing is at an angle of attack α and deflection $\{q_n\}$.

1. Use CFD to calculate the aerodynamic loads on the wing, $\{F\}$
2. Use the structural model to calculate the deflections, $\{q\}$
3. Calculate the change in deflection.
4. If the deflection $\{q_n\}$ and the angle of attack α results in aerodynamic forces $\{Q_n\}$, then $\{q_{n+1}\}$ is given by

$$[\Lambda]\{q_{n+1}\} = \{Q_n\} \tag{2.39}$$

So $\{\Delta q\}$ is given by

$$\{\Delta q\} = \{q_{n+1}\} - \{q_n\} \tag{2.40}$$

5. Update the deflection with the relaxation factor ω

$$\{q_{n+1}\} = \{q_n\} + \omega\{\Delta q\} \tag{2.41}$$

or

$$\{q_{n+1}\} = \{q_n\} + \omega(\{q_{n+1}\} - \{q_n\}) \tag{2.42}$$

And continue until some tolerance is reached. In this case, convergence is monitored through $||\Delta q||_2$. When $||\Delta q||_2 < \varepsilon$ then the algorithm is considered converged. (Figure 2.2).

2.4 Relaxation Algorithm for Trim Calculations

Initially the wing is at an angle of attack α_n and deflection $\{q_n\}$.

1. Use CFD to calculate the aerodynamic loads on the wing, $\{F\}$ and the lift, L.
2. Use the structural model to calculate the deflections, $\{q\}$
3. Calculate the change in alpha

   (Note that to calculate $\Delta\alpha$, lifts at two previous angles of attack must be known. If this is the first iteration, and the $\alpha = 0$ lift is known, this could be used.)

$\Delta\alpha$ is calculated based on the difference between the desired value of lift, and the current value of lift.

$$\Delta\alpha = (L_{des} - L_n)(\alpha_n - \alpha_{n-1})/(L_n - L_{n-1}) \tag{2.43}$$

4. Calculate the change in deflection.

   If the deflection $\{q_n\}$ gives forces $\{Q_n\}$, then $\{q_{n+1}\}$ is given by

$$[\Lambda]\{q_{n+1}\} = \{Q_n\} \tag{2.44}$$

   So $\{\Delta q\}$ is given by

$$\{\Delta q\} = \{q_{n+1}\} - \{q_n\} \tag{2.45}$$

5. Update deflection and angle of attack with the relaxation factor ω

$$\{q_{n+1}\} = \{q_n\} + \omega\{\Delta q\} \tag{2.46}$$

   or

$$\{q_{n+1}\}^r = \{q_n\} + \omega(\{q_{n+1}\} - \{q_n\}) \tag{2.47}$$

$$\alpha_{n+1} = \alpha_n + \omega\Delta\alpha \tag{2.48}$$

In this case, since the solution is being converged to a desired value of lift, convergence was determined through the error term defined above in equations 2.27 and 2.28.

2.5 Trim Calculations for Rigid Wing

Trim calculations for the rigid wing were made using a similar non derivative algorithm to the one above.

1. Calculate the lift at initial angles of attack α_0 and α_1.

2. Update the angle of attack as

$$\alpha_2 = \left(\frac{L_{des} - L_0}{L_1 - L_0}\right)(\alpha_1 - \alpha_0) + \alpha_0 \tag{2.49}$$

3. Calculate L_2 and check convergence based on $L_2 - L_1$.

4. If the lift is not converged, set

$$\begin{aligned} \alpha_0 &= \alpha_1 \\ \alpha_1 &= \alpha_2 \\ L_0 &= L_1 \\ L_1 &= L_2 \end{aligned} \tag{2.50}$$

and return to step 2.

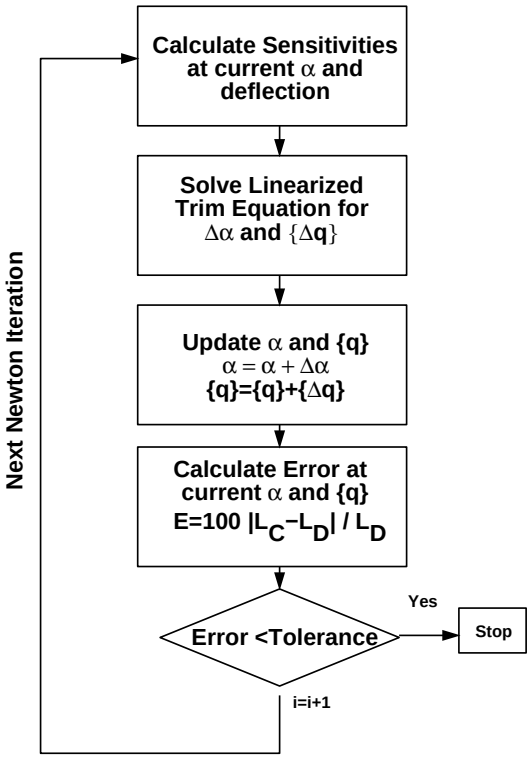

Figure 2.1: Newton's Method Trim Algorithm

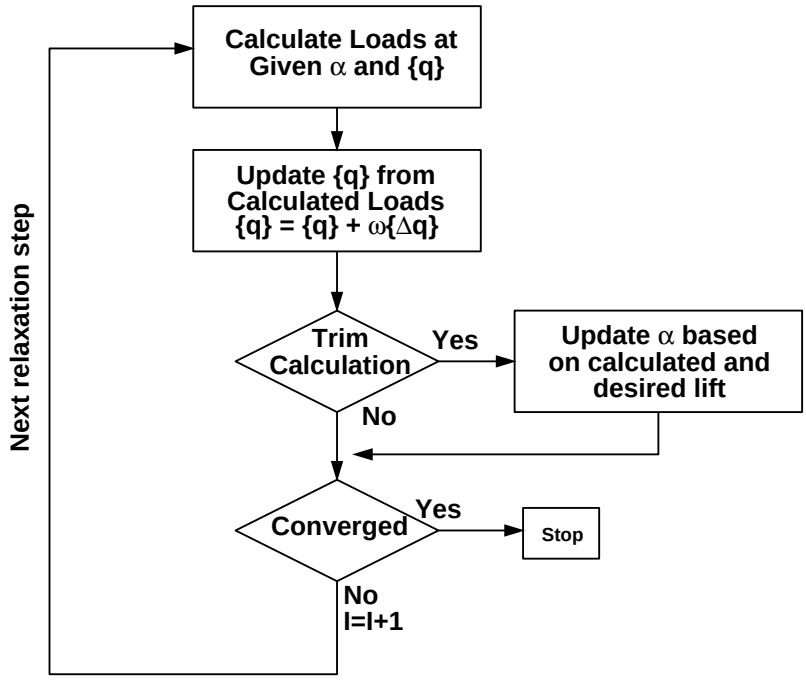

Figure 2.2: Non Derivative Trim Algorithm

Chapter 3

Data Transfer

One of the primary elements of any aeroelastic analysis is how one converts structural deflections to an aerodynamic geometry and how aerodynamic pressures are converted to structural loads.

In this research, the structural modeling is done through a modal representation of the wing. The mode shapes are splined onto the CFD surface grid before any aeroelastic calculations are performed. This is discussed in more detail below. The aeroelastic calculations are thus performed in the aerodynamic coordinate system. In other words, the load data that results from the aerodynamic calculation exists in the form of forces at the CFD grid points. The structural model using mode shapes already splined to the CFD grid expects force data at the CFD grid points, and no additional transformation is needed.

The governing structural model is given by equation 2.13

$$[\Lambda]\{q\} = \{Q\} \tag{3.1}$$

The generalized forces, $\{Q\}$ are expressed as CFD pressure forces integrated about the CFD grid points. The generalized displacement $\{q\}$ is expressed as modal amplitudes. The deflection is then a linear combination of the mode shapes that have

been splined onto the CFD surface grid.

3.1 Pressure Integration

If the CFD grid cell designated as $cell_{i,j}$ is the cell bounded by the points $\vec{x}_{i,j}$, $\vec{x}_{i+1,j}$, $\vec{x}_{i,j+1}$ and $\vec{x}_{i+1,j+1}$ (see Figure 3.1) then the integrated aerodynamic load at the CFD grid point $\vec{x}_{i,j}$ is given by

$$\vec{F} = \frac{1}{4}\sum_i S_i \hat{n}_i p_i \tag{3.2}$$

where the sum is over the 4 CFD grid cells surrounding the grid point in question, S_i is the area of the cell, $\hat{n}_i$ is the unit normal vector of the grid cell, and p_i is the cell centered pressure from the output of the CFD code. If the grid point in question is on a grid boundary, then the summation is over the surrounding 2 cells. If the grid point is in a computational 'corner' of the grid, then the corresponding corner cell is the only term in the summation. (see Figure 3.2)

The generalized forces, $\{Q\}$ are given by $\{Q\} = [\Phi]^T\{F\}$ as explained above, where the matrix of mode shapes $[\Phi]$ has already been transformed to the aerodynamic coordinate system as described below.

3.2 Splining Deflections

The initial step in the structural calculations in this research is to calculate the mode shapes and spline them onto the CFD surface grid.

For the simple wing, the structural calculations were performed using the McDonnell Douglas Aeroelastic Design Optimization Program (ADOP).[17] The splining procedure is internal to ADOP.[16]

3.3 Deflection Transfer in ADOP

In ADOP, the first step in the transfer of displacements from the structural analysis results to aerodynamic grids is to project each aerodynamic grid point onto an adjacent structural node. This process creates transformation data to be used throughout the aeroelastic analysis procedure. With the offset distance between the aerodynamic grid point and the adjacent structural element as r_z, the projection from the structural to the aerodynamic coordinate systems is

$$\begin{Bmatrix} u \\ v \\ w \end{Bmatrix}_{aero} = \begin{bmatrix} 1 & 0 & 0 & 0 & r_z & 0 \\ 0 & 1 & 0 & -r_z & 0 & 0 \\ 0 & 0 & 1 & 0 & 0 & 0 \end{bmatrix} \begin{Bmatrix} u \\ v \\ w \\ \theta_x \\ \theta_y \\ \theta_z \end{Bmatrix}_{FEM} \tag{3.3}$$

Where u, v and w are displacements and θ_x, θ_y and θ_z are rotational displacements in the structural frame of reference. Using this transformation, structural displacements are converted to displacements of the aerodynamic geometry. Note that rotations about the z-axis are not translated into aerodynamic deflections. ADOP neglects in-plane bending of the wing. (Figure 3.3)

3.4 Deflection Transfer in the Aeroelastic Research Wing (ARW) Calculations

For the ARW wing, ADOP was not used. NASTRAN[20] was used to generate the mode shapes from the finite element model used by Bhardwaj[3] in an analysis of this wing

The surface Spline of Harder and Desmarais[11] was used to transfer displacements from the FEM calculations of the mode shapes to the CFD surface grid. The spline is derived from the equations for an infinite plate that's deformation is restricted to bending. The governing equation is

$$w_j = a_0 + a_1 x_j + a_2 y_j + \sum_{i=1}^{N} F_i r_{ij}^2 \ln r_{ij}^2 \tag{3.4}$$

where w_j is the displacement at point (x_j, y_j), and $r_{ij}^2 = (x_i - x_j)^2 + (y_i - y_j)^2$.

Note that a problem seems to arise when $r_{ij} = 0$ due to the natural log term, however since $\lim_{r \to 0} r^2 \ln r^2 = 0$, then $r_{ij}^2 \ln r_{ij}^2 = 0$ when $r_{ij} = 0$. This avoids the problem of trying to calculate $\ln 0$ which doesn't exist.

Initially, using known structural points, the coefficients a_0, a_1, a_2 and F_i can be calculated. Using points from the FEM model for (x_j, y_j) where the value of W_j is known, N equations can be constructed for the surface spline. There are, however, $N + 3$ coefficients in equation 3.4 so three more equations are needed.

The three equations that are to be used are

$$\begin{aligned} \sum_{i=1}^{N} F_i &= 0 \\ \sum_{i=1}^{N} x_i F_i &= 0 \\ \sum_{i=1}^{N} y_i F_i &= 0 \end{aligned} \tag{3.5}$$

Harder and Desmarais[11] draw the parallel between these equations and equations of equilibrium.

Given N known points, and the three equilibrium equations, the coefficients are obtained by solving the following set of linear equations.

$$\begin{bmatrix} 1 & x_1 & y_1 & R_{11} & R_{12} & \cdots & R_{1N} \\ 1 & x_2 & y_2 & R_{21} & R_{22} & \cdots & R_{2N} \\ \vdots & \vdots & \vdots & \vdots & \vdots & \ddots & \vdots \\ 1 & x_N & y_N & R_{N1} & R_{N2} & \cdots & R_{NN} \\ 0 & 0 & 0 & 1 & 1 & \cdots & 1 \\ 0 & 0 & 0 & x_1 & x_2 & \cdots & x_N \\ 0 & 0 & 0 & y_1 & y_2 & \cdots & y_N \end{bmatrix} \begin{Bmatrix} a_0 \\ a_1 \\ a_2 \\ F_1 \\ F_2 \\ \vdots \\ F_N \end{Bmatrix} = \begin{Bmatrix} W_1 \\ W_2 \\ \vdots \\ W_N \\ 0 \\ 0 \\ 0 \end{Bmatrix} \tag{3.6}$$

where $R_{ij} = r_{ij}^2 \ln r_{ij}^2$ and r_{ij} is defined above.

After solving for the coefficients, one can return to equation 3.4 and solve for W given (x, y). Thus the deflection can be found for any CFD surface grid point. The Harder and Desmarais surface spline is a commonly used spline for aeroelastic calculations of this sort.[3,9,50] Note that this spline only translates deflections in the z-direction. In plane deflections of the surface are neglected.

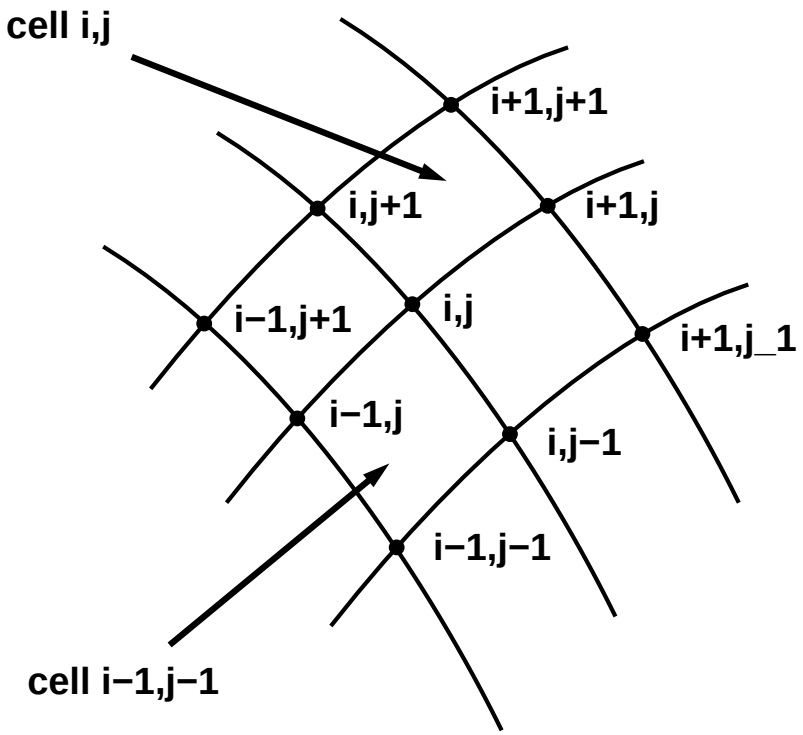

Figure 3.1: CFD Grid Point i,j and Surrounding Cells and Grid Points

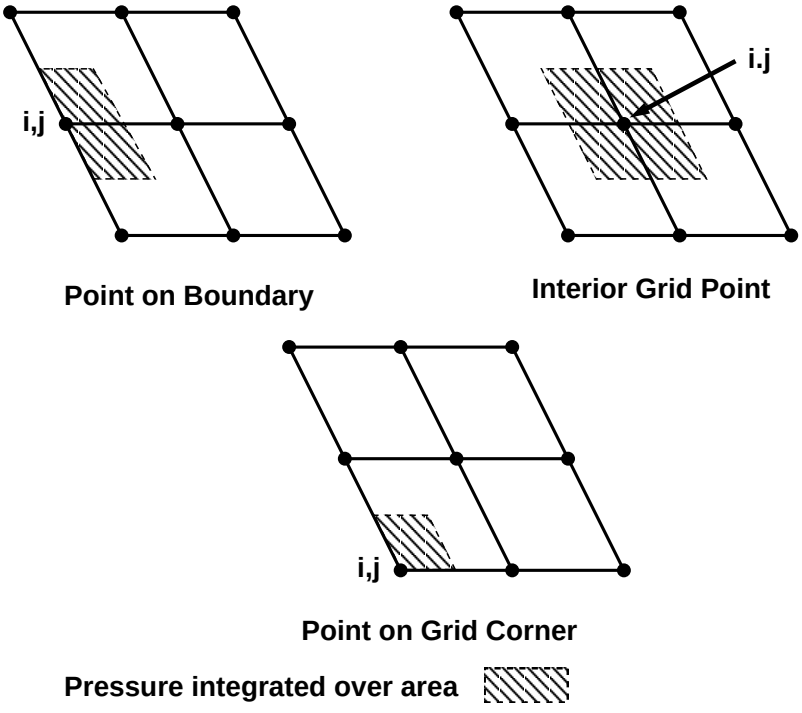

Figure 3.2: Stencil Used to Integrate Aerodynamic Pressure About CFD Grid Point i,j

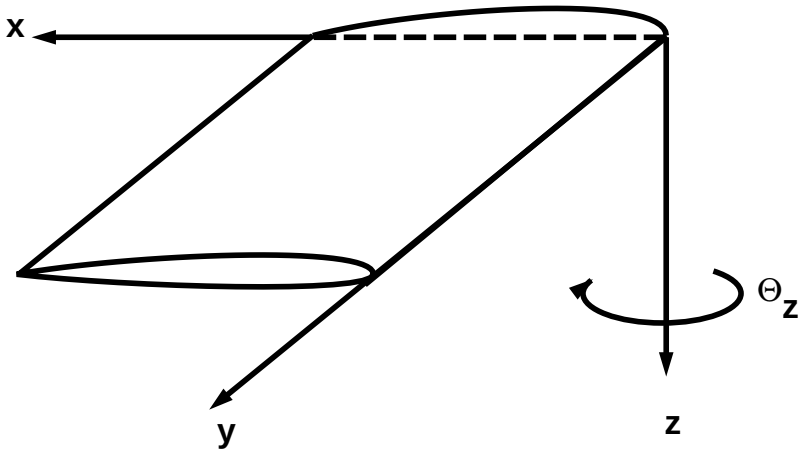

Figure 3.3: ADOP Neglects Rotations About the z-axis for Deflection Transfer

Chapter 4

Computational Aspects

Two types of aeroelastic analysis were performed in this research; analysis using the linearized trim equation as derived in chapter 2, and an analysis using the non derivative approach, discussed in chapter 2.

For the trim calculation, two computational methods were used. Serial calculations using a Cray YMP-C90 and a crude parallel methodology incorporating an IBM-SP2 and an SGI Power Challenge.

Calculations using the Cray C90 took approximately 25 minutes to converge the CFD calculation 3 orders of magnitude on the fine mesh. Trim calculations using the Cray took approximately 4.5 hours per iteration of CPU time, although the wall clock time was usually longer by a factor of about 3 or 4 depending upon the machine usage at the time.

The CFD code OVERFLOW[18] was used for the calculations on the Cray C90.

All other calculations were made using the code GASPv3. The non derivative calculations were made on an SGI Power Challenge using an R-8000 processor. To converge a CFD solution on the fine mesh ($251,865$ grid points) took approximately 2430 minutes. A convergence plot of a typical CFD calculation using GASPv3 is seen in Figure 4.1.

For the trim calculations, sensitivity terms were calculated on an IBM SP2. The SP2 uses an RS/6000 processor. The machine has 14 processors. An individual user can use from four to eight processors at a time, so from four to eight CFD solutions were calculated simultaneously depending on the current load on the machine. The IBM SP2 was noticeably slower than the SGI Power Challenge. A typical CFD solution on the fine mesh of the simple wing took approximately 3860 minutes of CPU time to converge 3 orders of magnitude.

Typically an iteration of the trim calculation took approximately 5 days of wall clock time.

Grids were generated using the NASA Ames hyperbolic grid generation code HYPGEN.[54] Appendix A contains a discussion about hyperbolic grid generation.

The ARW wing mesh was generated initially for use by ENSAERO by Farhangnia *et al.*[55] Farhangnia *et al.* state that the grid "has been found to be efficient and accurate for aeroelastic wing simulations".

4.1 Grid Convergence for Simple Wing

A convergence study was performed for the grid used in the aerodynamic calculations of the simple wing model using GASPv3 solving the Thin Layer Navier-Stokes equations. The grid used in these calculations had dimensions of 193 grid points in the chordwise direction, 29 points in the spanwise direction and 45 points normal to the wing surface. Grid convergence is presented as lift coefficient vs the number of grid points for 4 meshes. A coarse mesh (48x8x12), a medium mesh (87x15x23), a fine mesh (193x29x45), the mesh used in these calculations, and an ultra-fine mesh generated for the purpose of this study (385x57x89). (Figure 4.2).

The calculations were made at $\alpha = 1^0$ using the rigid wing, and using the Thin Layer Navier-Stokes equations.

The results show that there is little change in C_L from the fine to the ultra fine mesh. The numerical values being $C_L = 0.0911$ for the fine mesh and $C_L = 0.0910$ for the ultra fine mesh.

The angle twist and bending as a result of the loads from the fine and ultra fine meshes are plotted in Figure 4.3. Bending is measured as the difference in the vertical coordinate at the trailing edge. This is consistent with the results reported by Tzong *et al.*[16] who report maximum values of deflection at the trailing edge. The twist angle is determined as the angle between the deflected line between the leading and trailing edge of a section and the corresponding line on an undeflected section. (Figure 4.4). Pressure coefficient distribution at the 85% semi span location is plotted in Figure 4.5 and the spanload distribution is plotted in figure 4.6. Although there are subtle numerical differences in the values of C_p and section lift coefficient, the net result seen in the deflection is virtually unnoticeable. The desired result from CFD Calculations in aeroelasticity are the loads in order to calculate the deflections. Since the difference between the fine and ultra-fine meshes result in a very small difference in deflection, the fine mesh can be considered to be grid converged for the purposes of generating pressure loads.

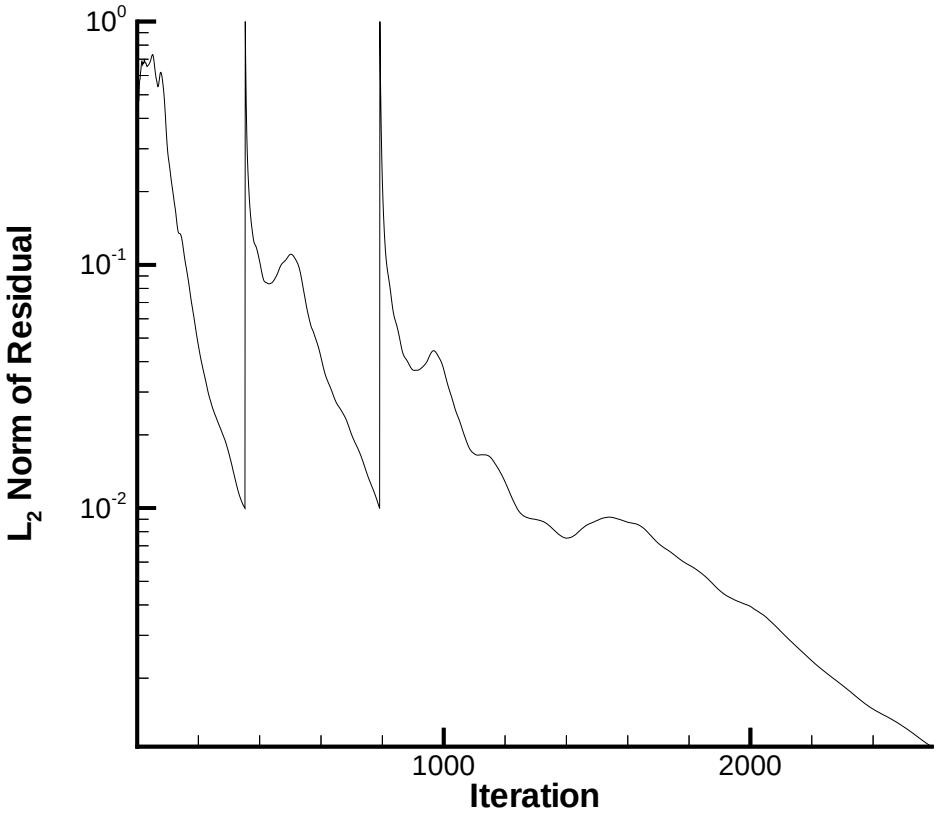

Figure 4.1: Residual Convergence for Typical CFD Calculation

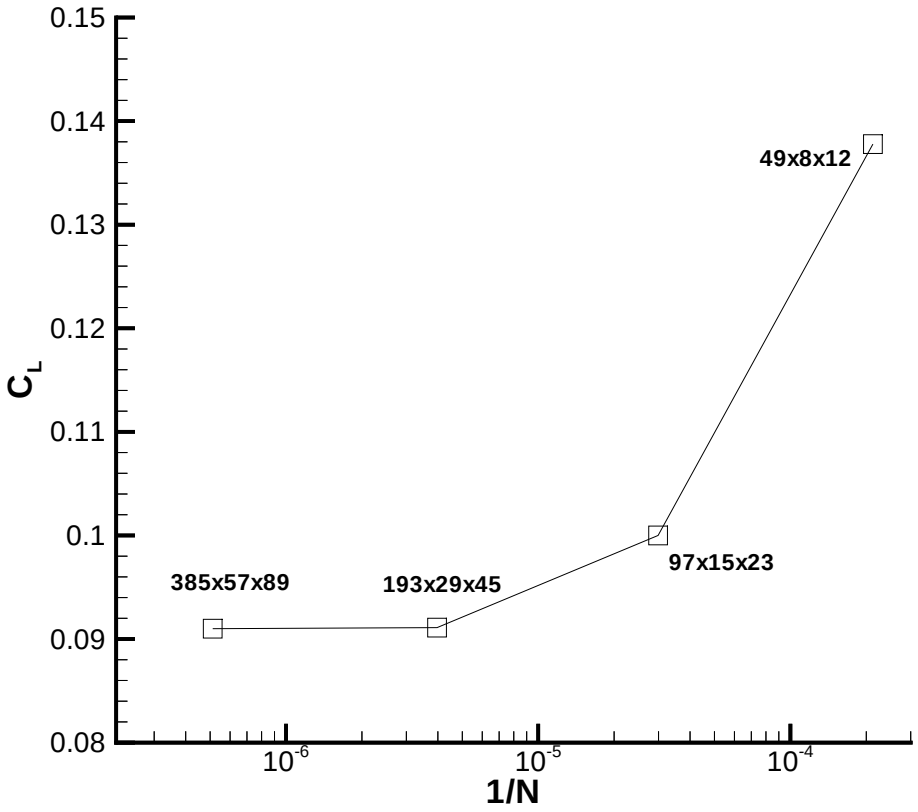

Figure 4.2: Grid Convergence for the Simple Wing, Rigid, $\alpha = 1^0$

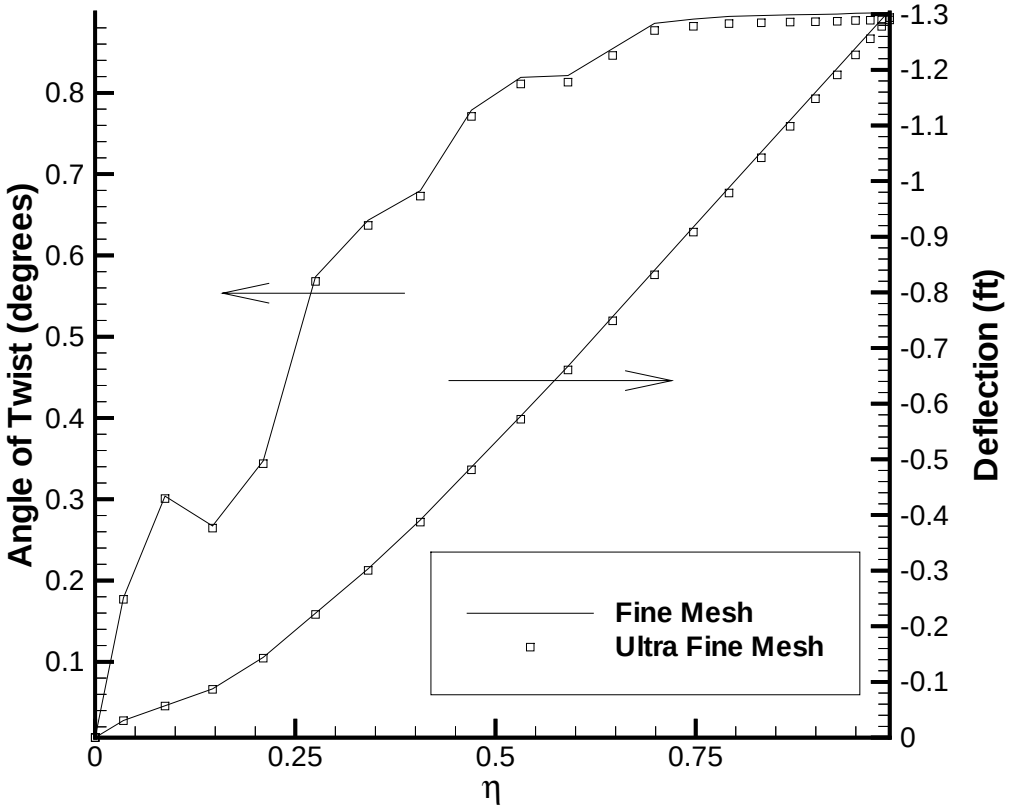

Figure 4.3: Deflection Difference Between Fine and Ultra-fine Meshes

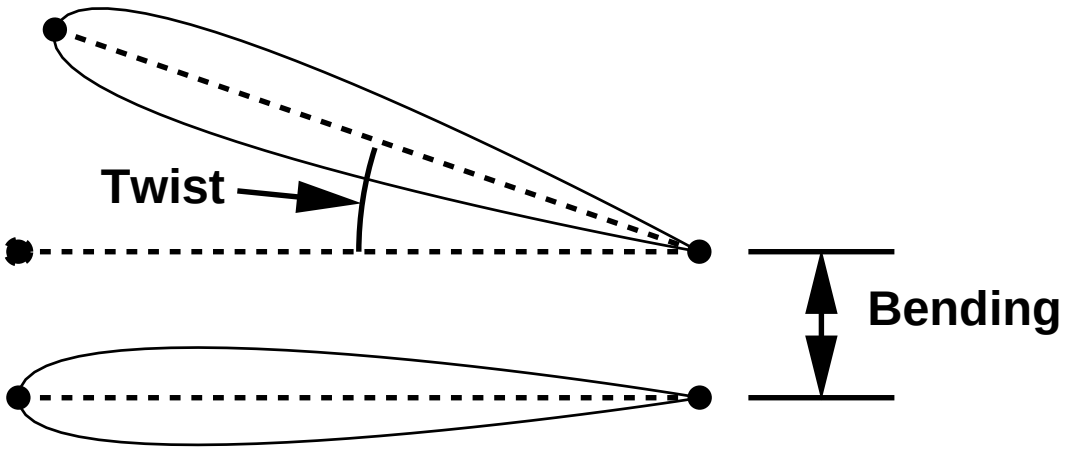

Figure 4.4: Definition of Twist and Bending

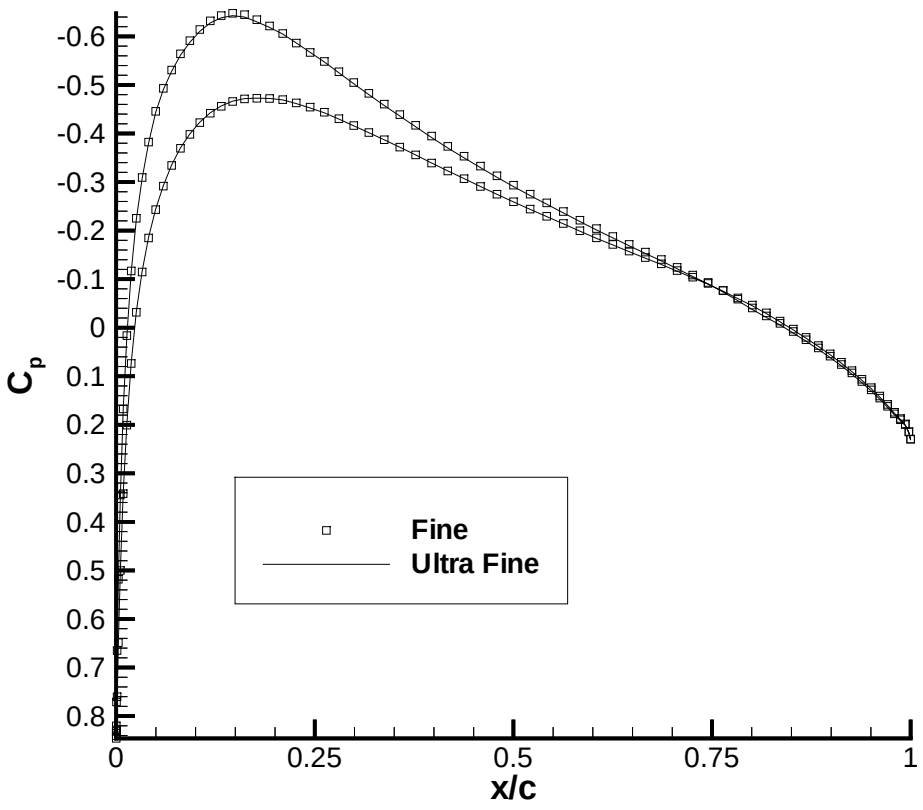

Figure 4.5: Pressure Coefficient Difference Between Fine and Ultra-fine Meshes at 85% Semi-Span

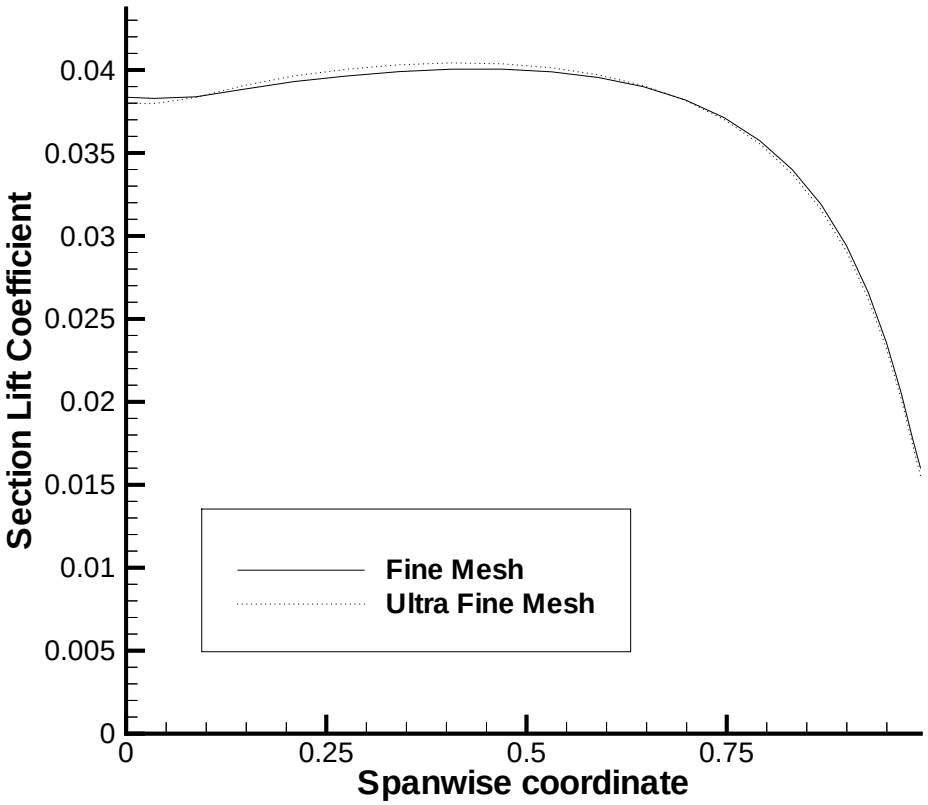

Figure 4.6: Spanload Comparison Between Fine and Ultra-Fine Meshes

Chapter 5

Simple Wing Results

5.1 Description of the Simple Wing Model

The wing has a NACA-0012 airfoil section. It is untapered, swept back at an angle of 30 degrees, has a wingspan of 350 inches and a chord of 100 inches (see Figure 5.1) The aerodynamic surface grid was initially generated for the undeflected wing at McDonnell Douglas Long Beach, now Boeing Long Beach. The grid has a C-H type topology with the C-grid going around the airfoil section of the wing and the H-grid normal to the wing.

The Finite Element model of the simple wing has 121 nodes, 419 degrees of freedom and is composed of 125 quadrilateral elements, 24 shell elements and 149 rod elements. (See Figure 5.2). Mode shapes for the wing are shown in Figure 5.3. Cases were run at a Mach number of $M = 0.80$, a dynamic pressure of $390psf$ and a Reynolds number of $2.1x10^7$ for the viscous cases.

5.2 Cases run

The trim algorithm is a function of desired lift. To determine the values of desired lift to use in the trim calculations, the wing span was used as a reference point to find the maximum take off weight for similar sized aircraft. Table 5.1 shows those values. The trim condition was calculated at 20,000 lbs intervals up to 80,000 lbs, and an initial calculation was made at 10,000 lbs using the strongly coupled method. Structural information was generated using the McDonnell Douglas/Boeing code ADOP[17] described previously from the finite element model. GASP[56] and OVERFLOW[18] were used to calculate the aerodynamic loads. GASP was used to solve the Euler Equations, and where OVERFLOW was used, a viscous solution was used. For the 20,000 lbs case both the Euler and Navier-Stokes equations were used. Table 5.2 summarizes the cases that were run.

The fixed angle of attack cases were run as a preliminary to the non derivative trim calculations. The fixed α cases were run at $\alpha = 1^o$. Four cases were calculated using the non derivative algorithm. Table 5.2 gives the breakdown of the 4 cases that were calculated with a fixed angle of attack. In all four cases, GASP was used to calculate the aerodynamic loads, solving the Euler Equations. Convergence for the non derivative calculations was determined by looking at the L_2 norm of the vector of modal amplitudes. Convergence was difficult to judge. The change in the modal amplitudes tended not to follow noticeable trends; however, if a downward trend was apparent, and the convergence reached below 2 orders of magnitude, the case was considered to be converged.

One non derivative Trim calculation was performed for a desired lift value of 20,000 lbs for comparison with the Newton's method calculations performed at the same value of lift using both the Euler and Navier-Stokes calculations.

The 40,000 lbs case was repeated using only 6 mode shapes to investigate the

possibility of using fewer mode shapes to calculate the trim condition to save computational resources. In addition, the trim angle of attack was calculated assuming the wing to be rigid using a non derivative algorithm described in chapter 2.

5.3 Discussion

5.3.1 Newtons Method Trim Calculations

Convergence values for angle of attack are presented in Table 5.3 . Convergence values for lift and error as defined in chapter 2 are presented in Table 5.4. Structural convergence is presented in figure 5.4. Structural convergence is plotted as the L2 norm of the change in the vector of modal amplitudes vs iteration. Note that the convergence of the deflection is the same order of magnitude as the convergence of error. Figure 5.4 shows that all the cases converged at approximately the same rate except for the 20,000 lbs case that was solved using the Newtons method algorithm with the Euler equations. This case converged much faster.

A comparison between the rigid and the flexible results are presented in Table 5.5 for both lift, and error as defined earlier. Figure 5.5 presents angle of attack convergence. Figure 5.6 presents the lift curve slope for the flexible and the rigid cases. The Converged values of α_{trim} when divided by the corresponding values of the rigid trim angle of attack collapse to a single value. This corresponds to a constant lift coefficient on Figure 5.6. Dividing the flexible trim angle of attack by the rigid angle of attack will result in a constant provided that it is within the linear range of both plots. Note that the 80,000 lbs case doesn't fall within the linear range, and doesn't collapse to the same constant as the other cases. This will be discussed below.

Figure 5.7 shows the normalized bending of all of the trim cases, and the shape of the deflection is consistent. The deflection was normalized so that the maximum value of deflection was 1 for each case. The coordinate system for the simple wing results

in lift being in the negative direction, so a negative value of bending corresponds to the wing bending up. Figure 5.8 shows the normalized twist of all the cases, and the shape of the viscous solutions is slightly different than that of the inviscid solutions. with the possible difference of the 10,000 lbs case. Twist angle for the inviscid cases shows a relative decrease in twist angle near the tip, and inboard. The maximum value of twist occurred at the same spanwise location for all of the trim cases, at approximately 70% span. Figure 5.9 shows spanload plots for the first four desired lift values. The plots have been scaled so that the area under each is the same in order to show how the lift distribution varies with changes in deflection. As the deflection increases, more lift would be expected to be generated inboard corresponding with the increased twist of the wing outboard. This effect was observed, but it was a more subtle effect than what was anticipated. Spanload for the rigid wing generating the same amount of lift was also plotted on the same figure.

Each case was started from the solution of the previous case. For example, the initial condition for the 40,000 lbs case was the solution of the 20,000 lbs case and so on. The graphical representation of the deflection for the 40,000 lbs and 60,000 lbs cases show little change in deflection after the initial iteration.

Plots of bending and twist convergence convergence and a graphical representation of the deflection for the 10,000 lbs cases are presented in Figures 5.10, 5.11 and 5.12. These plots show an oscillatory convergence of twist and deflection. The initial iteration overshoots the converged values of deflection and bending, and as iterations progress, the deflection decreases to the converged value. The graphical representation of the deflection makes this oscillatory behavior obvious. Again, the non-monotonic convergence behavior is visible on the twist convergence plot. The form of the twist distribution doesn't change with iteration, although the magnitude does.

For the 20,000 lbs viscous case, the deflection, bending and twist are shown in Figures 5.13, 5.14 and 5.15. Convergence behavior is again oscillatory with an initial overshoot and then a decrease in deflection as the solution approaches the converged

value. The twist distribution in this case is not different than the 10,000 lbs case, and again the non-monotonic convergence is visible on the convergence plots for both the angle of twist and the deflection. The maximum values of bending and twist for the 20,000 lbs viscous case are approximately twice the corresponding values for the 10,000 lbs case. The graphical representation of the deflection in this case again show the oscillatory nature of the convergence.

The 20,000 lbs case was repeated using the Euler equations to generate inviscid results to compare with the viscous results. Convergence in this case was much faster and was monotonic without the oscillatory behavior previously seen. The converged value was approximately reached in two iterations as opposed to four for the previous two cases although a third iteration was calculated. Bending distribution convergence is plotted in Figure 5.16, along with the twist distribution convergence in Figure 5.17 and a graphical representation of the deflection in Figure 5.18. In this case, the initial iteration on the twist distribution plot shows the maximum twist value at the wingtip, but the converged solution shows the maximum angle of twist at the 70% spanwise location. The graphical representation of the deflection shows the solution appears to be converged after two iterations.

The 40,000 lbs case was run using the Thin Layer Navier Stokes equations. Figure 5.19 Shows the deflection convergence and Figure 5.20 shows the twisting convergence. The deflection appears to be approximately converged after two iterations. Convergence again was oscillatory with the first iteration resulting in an overshoot of both twist and deflection. Values of maximum twist and bending are approximately twice that of the viscous 20,000 lbs case. Figure 5.21 shows the deflection of the wing for the 4 iterations and it shows that the deflection appears to be approximately converged after the second iteration.

The 60,000 lbs case was run using in inviscid solution. Deflection convergence is plotted in figure 5.22. It seems that the form of the bending is approximately converged after the first iteration. The same thing is apparent with the twist (Figure

5.23). The maximum values of bending and twist are approximately 3 times the magnitude of the maximum values for the 20,000 lbs inviscid solution. Figure 5.24 shows little change in the deflection as a function of the iteration.

The 80,000 lbs case behaved differently than the other cases. Based on Figure 5.6 it appears that this case may be stalled, and part of the flow field may be separated. However, since this case was solved using the Thin Layer Navier-Stokes equations, the results are suspect. In all probability, although the grid is converged for pressure using the Thin Layer equations it will not be fine enough to resolve details of separated flow. The results are included, however, for completeness. Bending, twisting and deflection are shown in Figures 5.25, 5.26 and 5.27. The convergence in this case was monotonic. The form of the bending was similar to the 20,000 lbs and 40,000 lbs viscous solution without the inboard maximum that was seen in the 10,000 lbs case and the 20,000 lbs inviscid case. The maximum values of bending and twist are approximately 5 times the corresponding values for the 20,000 lbs viscous case. The trend for the previous cases has been that the maximum values of twist and bending vary proportional to the lift, although in this case the maximum values are greater than proportional to the lift. This could be accounted for by the separated nature of the flow.

Tables 5.9, 5.10, and 5.11 present the numerical values of the modal amplitudes for the cases studies.

It was attempted to reduce the number of modes used in these calculations and the results for modal amplitudes are shown in Table 5.12. The 40,000 lbs case was repeated with 6 mode shapes, however this case did not converge in four iterations and the error continued to increase. Table 5.7 shows the convergence behavior for the angle of attack, the error between the actual and desired lifts, and the actual lift for this case.

5.3.2 Fixed Angle of Attack Calculations

The fixed angle of attack calculations were done as a precursor to the non derivative trim calculation.

Four cases were run. Two cases at a Mach number of 0.3 and two cases at a Mach number of 0.8. For each Mach number, two values of the relaxation parameter were used.

Table 5.13 presents the numerical values of the modal amplitudes for the first of the fixed angle of attack static aeroelastic analyses. Convergence was not apparent after 7 iterations at a Mach Number of 0.3

Tables 5.14, 5.15 and 5.16 contain the modal amplitudes for the following 3 fixed α calculations. Using a relaxation factor of 0.5 facilitated convergence of this case in 5 iterations. Increasing the Mach number to 0.8, the deflected solution was calculated using relaxation factors of $\omega = 0.4$ and $\omega = 0.5$ (Figure 5.28)

The initial case was calculated at a Mach number of $M = 0.3$ and a relaxation factor of $\omega = 1.0$. Bending convergence is plotted in figure 5.29. This case did not converge and an oscillatory behavior is apparent in the behavior of the deflection and the twist (Figure 5.30).

Figure 5.31 shows bending convergence for the $M = 0.3$, $\omega = 0.5$ case. Bending convergence shows monotonic behavior. Twist convergence shown in figure 5.32 shows a similar behavior to the trim solutions with the maximum value of twist at the 70% span location.

Increasing the Mach number to $M = 0.8$, the calculation was repeated using a relaxation factor of $\omega = 0.5$. Twist distribution as a function of iteration is plotted in figure 5.34. Bending distribution is shown in figure 5.33. Bending does not seem to change as the solution advances. Twist distribution as a function of iteration is plotted in figure 5.34. The Angle of Twist does change dramatically with iteration,

and perhaps indicates that the solution is not fully converged. Convergence is not apparent from figure 5.28.

The relaxation factor was decreased to $\omega = 0.4$, and the Mach number was not changed. Figure 5.35 shows the convergence of the deflection distribution. Figure 5.36 shows the convergence of the twist distribution. The deflection appears to be converged based on this plot. The angle of twist appears to be converged based on figure 5.36 but convergence was not apparent from figure 5.28. The twist distribution is consistent with the shape of the twist distribution in the 10,000 lbs case, and the numerical values of twist are approximately the same. This is to be expected since both of these solutions were at approximately the same angle of attack.

5.3.3 Non Derivative Trim Calculations

The non derivative trim calculation was performed with a relaxation parameter of $\omega = 0.4$ for a desired lift value of 20,000 lbs. This case converged in 9 iterations based on the convergence criteria used in the Newtons method trim calculations. Error convergence is given in Table 5.8. Figure 5.37 shows both the structural convergence, and the convergence for α_{trim}. Note that the normalized change in deflection for the structure has converged approximately 2 orders of magnitude, and the lift discrepancy has converged to within 1 percent, however the angle of attack does not appear to be fully converged. Figure 5.38 shows the convergence of the deflection distribution along the wing. Convergence in this case is oscillatory. Twist distribution is shown in figure 5.39 and is consistent with the results using Newton's method inviscid results. Figure 5.40 shows the deflected shape of the wing as a function of convergence. The oscillatory nature of the convergence is apparent.

5.3.4 Viscous vs Inviscid Results

Three trimmed cases were calculated for a desired lift of 20,000 lbs. Bending and Twisting results for the three cases are presented in Figures 5.41 and 5.42. Table 5.6 presents the results for the three calculations. Although all three converged with respect to lift, α_{trim} for the non derivative case is markedly less than the other two cases. This may be because lift discrepancy is not a completely adequate marker for the convergence in that case. The strongly coupled cases are derived taking the coupling of the fluid and the structures into account. The non derivative algorithm described earlier takes only the aerodynamics into account when it updates the angle of attack. So although the structural deflection and the lift error appear to be converged independently, the coupled system may not be.

The bending and the twist distribution of the three 20,000 lbs cases is similar. The non derivative solution results in less deflection than either of the Newton's method solutions, likely due to the reduced angle of attack. The viscous solution resulted in greater deflection than the inviscid solution. The twist distribution in the three cases is slightly different, although the maximum difference in twist angle is less than 0.2^o. Between the viscous and the inviscid solutions, the inviscid solution resulted in greater angle of twist along the wing. The NDM calculation resulted in less twist, but again this could be due to the decreased angle of attack, and corresponding decrease in lift. Figure 5.44 shows the spanload for the three cases. The viscous flow solution experiences a greater loss of lift near the wing tip than do the inviscid cases. This is reflected in the deflection plot as well, but not as dramatically as the twist effect. Figure 5.45 shows the deflected wings for the three cases superimposed. There is a noticeable difference in the wing geometry due to the subtle differences in bending and the significant difference in the twist. Figure 5.43 shows Cp plots for Navier Stokes and Euler calculations at the same spanwise location 80% outboard.

Table 5.1: Aircraft Weight Comparison

Aircraft	Wing Span	Max. Take Off Weight
Cessna Citation Excel	55' 8.5"	14,000 lbs
Cessna 750 Citation X	62' 11"	34,500 lbs
GulfStream IV	77' 10"	74,000 lbs
McDonnell Douglas M-D 95	93' 3.5"	121,000 lbs

Table 5.2: Case Summary

Trim Calculations			
Aerodynamics (Code)	Desired Lift	Algorithm	No. of Modes
TLNS (OVERFLOW)	10,000 lbs	Newton's Method	8
TLNS (OVERFLOW)	20,000 lbs	Newton's Method	8
Euler (GASP)	20,000 lbs	Newton's Method	8
Euler (GASP)	20,000 lbs	Non Derivative	8
TLNS (OVERFLOW)	40,000 lbs	Newton's Method	8
TLNS (OVERFLOW)	40,000 lbs	Newton's Method	6
Euler (GASP)	60,000 lbs	Newton's Method	8
TLNS (OVERFLOW)	80,000 lbs	Newton's Method	8
Fixed α Calculations			
Aeodynamics (Code)	Mach Number	Relaxation Factor	α
Euler (GASP)	0.3	1.0	1.0
Euler (GASP)	0.3	0.5	1.0
Euler (GASP)	0.8	0.5	1.0
Euler (GASP)	0.8	0.4	1.0

Table 5.3: Convergence history of the trim angle of attack, * GASP Solution (Euler)

	α_{trim} (degrees)				
Iteration	10,000 lbs	20,000 lbs	40,000 lbs	60,000 lbs *	80,000 lbs
1	1.188350	2.227816	4.407093	5.617503	8.419924
2	0.936341	1.847846	3.791764	5.816602	8.892019
3	0.993333	1.983497	3.905955	5.765289	9.244597
4	1.000888	1.946902	3.876949	5.777348	9.474579
5					9.635559
6					9.752693

Table 5.4: Convergence history of lift, * GASP Solution (Euler)

	Lift in Pounds				
Iteration	10,000 lbs	20,000 lbs	40,000 lbs	60,000 lbs *	80,000 lbs
1	12,060	23,046	44,963	57871	73747
2	9,409	18,896	39,089	60662	77160
3	9,922	20,298	39,060	59849	78186
4	9,990	20,053	39,943	59989	78717
5					79059
6					79325
	Percentage Error				
1	20.6	15.2	12.4	3.5	7.8
2	5.9	5.5	2.3	1.1	3.5
3	0.78	1.5	0.58	0.25	2.3
4	0.10	0.27	0.14	0.018	1.6
5					1.18
6					0.84

Table 5.5: Comparison between Rigid and Flexible Wing Results, * GASP Solution (Euler)

	Flexible		Rigid	
	α_{trim} (degrees)	Error (percent)	α_{trim} (degrees)	Error (percent)
10,000 lbs	1.001	0.10	0.621	0.40
20,000 lbs	1.947	0.26	1.242	0.10
20,000 lbs*	1.947	0.67	1.242	0.10
40,000 lbs	3.877	0.14	2.484	0.05
60,000 lbs*	5.777	0.02	3.726	1.5
80,000 lbs	9.474	0.84	5.358	0.01

Table 5.6: The 20,000-lbs (20K) case

	N-S	Euler	Non Derivative Euler
$\alpha_{trim}(degrees)$	1.947	1.947	1.822
Lift (lbs)	20,053	20,133	19901
Error(percent)	0.27	0.67	.50
Convergence (Iterations)	4	4	9

Table 5.7: Convergence history of 40,000-lbs (40k) Case Using 6 Mode Shapes

40,000-lbs			
Iteration	Lift	Error (percent)	α_{trim}
1	43,250	8.12	4.314
2	39,823	0.44	3.941
3	40,340	0.80	3.961
4	39,643	0.89	3.922

Table 5.8: Non Derivative Trim Calculation for the 20,000 lbs Case

	Lift	α_{trim} (degrees)	Error (percent)
Iteration 1	35632	1.498	78.1
Iteration 2	13886	1.170	30.6
Iteration 3	16836	1.427	15.8
Iteration 4	17126	1.552	14.4
Iteration 5	18933	1.693	5.33
Iteration 6	19360	1.752	3.20
Iteration 7	19361	1.781	3.19
Iteration 8	19867	1.810	0.665
Iteration 9	19901	1.822	0.495

Table 5.9: Convergence of Modal Amplitudes for 10K and 20K Cases

	modal amplitude			
10,000 lbs				
	Iteration 1	Iteration 2	Iteration 3	Iteration 4
Mode 1	-0.1074443E+01	-0.8554238E+00	-0.9182862E+00	-0.9266195E+00
Mode 2	-0.6851629E-01	-0.5361590E-01	-0.5789260E-01	-0.5845950E-01
Mode 3	-0.1016169E-01	-0.9457701E-02	-0.9655483E-02	-0.9682496E-02
Mode 4	0.1084679E-01	0.7882859E-02	0.8733555E-02	0.8846327E-02
Mode 5	-0.4232339E-02	-0.3402194E-02	-0.3640458E-02	-0.3672092E-02
Mode 6	-0.2043739E-02	-0.1587604E-02	-0.1718555E-02	-0.1735909E-02
Mode 7	0.4946848E-03	0.3217618E-03	0.3713938E-03	0.3779732E-03
Mode 8	-0.9389894E-03	-0.8187877E-03	-0.8532880E-03	-0.8578615E-03
20,000 lbs				
Mode 1	-0.1997852E+01	-0.1667532E+01	-0.1786934E+01	-0.1754658E+01
Mode 2	-0.1305921E-00	-0.1089253E-00	-0.1167598E-00	-0.1146529E-00
Mode 3	-0.1249460E-01	-0.1108180E-01	-0.1154880E-01	-0.1142000E-01
Mode 4	0.2342250E-01	0.1929020E-01	0.2071610E-01	0.2033500E-01
Mode 5	-0.7572083E-02	-0.6356725E-02	-0.6795230E-02	-0.6677739E-02
Mode 6	-0.3955750E-02	-0.3304975E-02	-0.3536024E-02	-0.3474020E-02
Mode 7	0.1275180E-02	0.1043132E-02	0.1128981E-02	0.1106058E-02
Mode 8	-0.1436282E-02	-0.1242345E-02	-0.1312136E-02	-0.1293291E-02
20,000 lbs Euler				
Mode 1	-0.1308444E+01	-0.1872516E+01	-0.1865668E+01	
Mode 2	-0.5748770E-01	-0.9147856E-01	-0.8932063E-01	
Mode 3	-0.2626300E-01	-0.2199040E-01	-0.2120963E-01	
Mode 4	0.1150785E-01	0.1527134E-01	0.1521633E-01	
Mode 5	-0.3673650E-02	-0.5349219E-02	-0.5339943E-02	
Mode 6	-0.6871989E-02	-0.2521046E-02	-0.2513372E-02	
Mode 7	0.2291219E-03	0.5153110E-03	0.5160723E-03	
Mode 8	-0.6895439E-03	-0.1275716E-02	-0.1272884E-02	

Table 5.10: Convergence of Modal Amplitudes for 40K and 60K Cases

	modal amplitude			
40,000 lbs				
	Iteration 1	Iteration 2	Iteration 3	Iteration 4
Mode 1	-0.3924485E+01	-0.3340882E+01	-0.3443456E+01	-0.3417401E+01
Mode 2	-0.2563105E-00	-0.2220760E-00	-0.2285558E-00	-0.2269245E-00
Mode 3	-0.2007640E-01	-0.1748045E-01	-0.1795020E-01	-0.1783122E-01
Mode 4	0.4595110E-01	0.3720910E-01	0.3858103E-01	0.3822724E-01
Mode 5	-0.1457620E-01	-0.1268760E-01	-0.1304903E-01	-0.1295796E-01
Mode 6	-0.7641985E-02	-0.6682441E-02	-0.6870830E-02	-0.6823441E-02
Mode 7	0.2647043E-02	0.2311565E-02	0.2376429E-02	0.2360143E-02
Mode 8	-0.2560106E-02	-0.2255262E-02	-0.2315133E-02	-0.2300795E-02
60,000 lbs				
Mode 1	-0.5268989E+01	-0.5470913E+01	-0.5409862E+01	-0.5424629E+01
Mode 2	-0.2928642E+00	-0.2999478E+00	-0.2976285E+00	-0.2981224E+00
Mode 3	-0.3544110E-01	-0.3729441E-01	-0.3665510E-01	-0.3678747E-01
Mode 4	0.5266673E-01	0.5402348E-01	0.5343960E-01	0.5354468E-01
Mode 5	-0.1680466E-01	-0.1716801E-01	-0.1704640E-01	-0.1707016E-01
Mode 6	-0.8478489E-02	-0.8641371E-02	-0.8561844E-02	-0.8574882E-02
Mode 7	0.2813099E-02	0.2863123E-02	0.2849901E-02	0.2853182E-02
Mode 8	-0.2985700E-02	-0.3061637E-02	-0.3040743E-02	-0.3045873E-02

Table 5.11: Convergence of Modal Amplitudes for 80K Case

	modal amplitude		
	Iteration 1	Iteration 2	Iteration 3
Mode 1	-0.78485285E+01	-0.84777063E+01	-0.87346895E+01
Mode 2	-0.50827510E+00	-0.55598090E+00	-0.57774936E+00
Mode 3	-0.38224300E-01	-0.42097800E-01	-0.43646800E-01
Mode 4	0.96866500E-01	0.10776330E+00	0.11086120E+00
Mode 5	-0.29163300E-01	-0.31800500E-01	-0.33279600E-01
Mode 6	-0.14613200E-01	-0.15534600E-01	-0.15967300E-01
Mode 7	0.51690770E-02	0.55940023E-02	0.57851894E-02
Mode 8	-0.49443620E-02	-0.53648804E-02	-0.55530377E-02
	Iteration 4	Iteration 5	Iteration 6
Mode 1	-0.88924061E+01	-0.90005895E+01	-0.90786369E+01
Mode 2	-0.59138040E+00	-0.60099070E+00	-0.60801240E+00
Mode 3	-0.44597300E-01	-0.45253900E-01	-0.45726474E-01
Mode 4	0.11237990E+00	0.11325000E+00	0.11378350E+00
Mode 5	-0.34285700E-01	-0.35031600E-01	-0.35588900E-01
Mode 6	-0.16242600E-01	-0.16437300E-01	-0.16578100E-01
Mode 7	0.59097112E-02	0.59976973E-02	0.60625052E-02
Mode 8	-0.56755104E-02	-0.57618777E-02	-0.58256693E-02

Table 5.12: Convergence of Modal Amplitudes for 6 Mode shape, 40K Case

	modal amplitude			
40,000 lbs, 6 Mode Shapes				
	Iteration 1	Iteration 2	Iteration 3	Iteration 4
Mode 1	-0.39354331E+01	-0.35574078E+01	-0.35769540E+01	-0.35392742E+01
Mode 2	-0.25482990E+00	-0.23247730E+00	-0.23372340E+00	-0.23131320E+00
Mode 3	-0.19790400E-01	-0.18117500E-01	-0.18211000E-01	-0.18031641E-01
Mode 4	0.44130700E-01	0.38672800E-01	0.38961400E-01	0.38423173E-01
Mode 5	-0.14431000E-01	-0.13188500E-01	-0.13262200E-01	-0.13124134E-01
Mode 6	-0.72640560E-03	-0.66538826E-02	-0.66925015E-02	-0.66232460E-02

Table 5.13: Non Derivative Static Aeroelastic Solution Starting From Rigid Wing, $\alpha = 1$, $M = 0.3$, $\omega = 1$

	modal amplitude			
	Iteration 1	Iteration 2	Iteration 3	Iteration 4
Mode 1	-0.1615098E+00	-0.1391196E+00	-0.1434317E+00	-0.1387136E+00
Mode 2	-0.4981507E-02	-0.5310840E-02	-0.5269170E-02	-0.5235001E-02
Mode 3	-0.2524556E-02	-0.2211212E-02	-0.2261413E-02	-0.2298121E-02
Mode 4	0.1449702E-02	0.4489448E-02	0.6150652E-03	0.7087231E-03
Mode 5	-0.3264850E-03	-0.2660658E-03	-0.2764724E-03	-0.2736204E-03
Mode 6	-0.1278570E-03	-0.1223396E-03	-0.1212609E-03	-0.1259038E-02
Mode 7	-0.2130464E-03	-0.1944694E-03	-0.1973483E-03	-0.1977977E-03
Mode 8	-0.2626768E-03	-0.2823666E-03	-0.2792670E-03	-0.2791028E-03
	Iteration 5	Iteration 6	Iteration 7	
Mode 1	0.9176740E-00	-0.3650330E+00	-0.9502632E-01	
Mode 2	-0.1001551E-01	-0.3402740E-02	-0.5665523E-02	
Mode 3	0.4964562E-02	-0.3941658E-02	-0.1907888E-02	
Mode 4	-0.2430927E-01	0.6213125E-02	-0.5871188E-03	
Mode 5	0.1703190E-02	-0.7288620E-03	-0.1778317E-03	
Mode 6	-0.8537062E-04	-0.9361276E-04	-0.1292433E-03	
Mode 7	0.3412881E-03	-0.3188215E-03	-0.1712686E-03	
Mode 8	-0.8362847E-03	-0.1512835E-03	-0.3068174E-03	

Table 5.14: Non Derivative Static Aeroelastic Solution starting from rigid wing, $\alpha = 1$, $M = 0.3$, $\omega = 0.5$

	modal amplitude			
	Iteration 1	Iteration 2	Iteration 3	Iteration 4
Mode 1	-0.8075489E-01	-0.1162522E+00	-0.1323265E+00	-0.1388471E+00
Mode 2	-0.2490753E-02	-0.3832530E-02	-0.4543559E-02	-0.4907377E-02
Mode 3	-0.1262278E-02	-0.1820087E-02	-0.2050761E-02	-0.2157260E-02
Mode 4	0.7248510E-03	0.8415341E-03	0.7592986E-03	0.6901004E-03
Mode 5	-0.1632425E-03	-0.2298380E-03	-0.2569035E-03	-0.2675788E-03
Mode 6	-0.6392850E-04	-0.9500340E-04	-0.1083171E-03	-0.1149142E-03
Mode 7	-0.1065232E-03	-0.1551492E-03	-0.1771612E-03	-0.1873787E-03
Mode 8	-0.1313384E-03	-0.2019858E-03	-0.2395855E-03	-0.2591878E-03
	Iteration 5			
Mode 1	-0.1388471E+00			
Mode 2	-0.5065645E-02			
Mode 3	-0.2232175E-02			
Mode 4	0.7139233E-03			
Mode 5	-0.2712949E-03			
Mode 6	-0.1207156E-03			
Mode 7	-0.1928487E-03			
Mode 8	-0.2688607E-03			

Table 5.15: Non Derivative Static Aeroelastic Solution Starting From Rigid Wing, $\alpha = 1$, $M = 0.8$, $\omega = 0.5$

	modal amplitude			
	Iteration 1	Iteration 2	Iteration 3	Iteration 4
Mode 1	-0.8671300E+00	-0.8536603E+00	-0.8699241E+00	-0.8733600E+00
Mode 2	-0.2773575E-01	-0.3225261E-01	-0.3492439E-01	-0.3614274E-01
Mode 3	-0.9979905E-02	-0.1171734E-01	-0.1262498E-01	-0.1304035E-01
Mode 4	0.7904905E-02	0.6943694E-02	0.6601420E-02	0.6376206E-02
Mode 5	-0.1454126E-02	-0.1792979E-03	-0.1961395E-02	-0.2037198E-02
Mode 6	-0.5962760E-03	-0.7666952E-03	-0.8521096E-03	-0.8915504E-03
Mode 7	0.9258535E-04	0.1562323E-03	0.1886283E-03	0.2050204E-03
Mode 8	0.2964300E-03	-0.3958916E-04	-0.4639196E-03	-0.4980518E-03
	Iteration 5	Iteration 6		
Mode 1	-0.8695167E+00	-0.8885216E+00		
Mode 2	-0.3667835E-01	-0.3738994E-01		
Mode 3	-0.1332916E-01	-0.1353685E-01		
Mode 4	0.6312280E-02	0.6275928E-02		
Mode 5	-0.2079087E-02	-0.2104687E-02		
Mode 6	-0.9103761E-02	-0.9149235E-03		
Mode 7	0.2120934E-03	0.2155731E-03		
Mode 8	-0.5168147E-03	-0.5238780E-03		

Table 5.16: Non Derivative Static Aeroelastic Solution Starting From Rigid Wing, $\alpha = 1$, $M = 0.8$, $\omega = 0.4$

	modal amplitude			
	Iteration 1	Iteration 2	Iteration 3	Iteration 4
Mode 1	-0.6937040E+00	-0.8227416E+00	-0.9320446E+00	-0.9248737E+00
Mode 2	-0.2218860E-01	-0.2951070E-01	-0.3499624E-01	-0.3653935E-01
Mode 3	-0.7983924E-02	-0.3514910E-01	-0.2707833E-01	-0.2171432E-01
Mode 4	0.6323924E-02	0.6990948E-02	0.7412814E-02	0.6945353E-02
Mode 5	-0.1163301E-02	-0.1611849E-02	-0.1855787E-02	-0.1950739E-02
Mode 6	-0.4770208E-03	-0.6801929E-03	-0.7998493E-03	-0.8528097E-03
Mode 7	0.7406828E-04	0.1294684E-03	0.1690674E-03	0.1931264E-03
Mode 8	-0.2051440E-03	-0.3359459E-03	-0.4225241E-03	-0.4714542E-03
	Iteration 5	Iteration 6	Iteration 7	Iteration 8
Mode 1	-0.9205711E+00	-0.8979481E+00	-0.8885855E+00	-0.8836832E+00
Mode 2	-0.3746522E-01	-0.3739439E-01	-0.3739891E-01	-0.3739399E-01
Mode 3	-0.1849589E-01	-0.1643098E-01	-0.1522552E-01	-0.1450961E-01
Mode 4	0.6664875E-02	0.6357880E-02	0.6237565E-02	0.6184341E-02
Mode 5	-0.2007713E-02	-0.2035359E-02	-0.2058035E-02	-0.2073953E-02
Mode 6	-0.8845860E-03	-0.8991410E-03	-0.9093204E-03	-0.9158216E-03
Mode 7	0.2075617E-03	0.2145487E-03	0.2180333E-03	0.2197823E-03
Mode 8	-0.5014522E-03	-0.5158208E-03	-0.5235439E-03	-0.5276857E-03

Table 5.17: Non Derivative Trim Calculation for 20K Case. $M = 0.8$, $\omega = 0.5$

	modal amplitude			
	Iteration 1	Iteration 2	Iteration 3	Iteration 4
Mode 1	-0.2207199E+01	-0.8304474E+00	-0.1019641E+01	-0.1243381E+01
Mode 2	-0.6947510E-01	-0.2518685E-01	-0.3644548E-01	-0.4733111E-01
Mode 3	-0.1346974E-01	-0.1282321E-01	-0.1454778E-01	-0.1667180E-01
Mode 4	0.2475075E-01	0.5012853E-02	0.7096486E-02	0.9350980E-02
Mode 5	-0.3319928E-02	-0.4826742E-03	-0.1555861E-02	-0.2364528E-02
Mode 6	-0.1222750E-02	-0.3275703E-03	-0.7319516E-03	-0.1052346E-02
Mode 7	0.3722996E-03	0.1778780E-04	0.1454610E-03	0.2484875E-03
Mode 8	-0.3132136E-03	-0.2563979E-03	-0.4290639E-03	-0.5664769E-03
	Iteration 5	Iteration 6	Iteration 7	Iteration 8
Mode 1	-0.1325706E+01	-0.1500960E+01	-0.1556448E+01	-0.1576542E+01
Mode 2	-0.5443877E-01	-0.6198419E-01	-0.6511933E-01	-0.6675507E-01
Mode 3	-0.1832107E-01	-0.2018463E-01	-0.2043023E-01	-0.2053828E-01
Mode 4	0.1096839E-01	0.1297614E-01	0.1266794E-01	0.1243477E-01
Mode 5	-0.2911527E-02	-0.3362215E-02	-0.3539252E-02	-0.3649109E-02
Mode 6	-0.1325079E-02	-0.1527783E-02	-0.1593437E-02	-0.1638390E-02
Mode 7	0.3302676E-03	0.3879194E-03	0.4288560E-03	0.4543936E-03
Mode 8	-0.6821448E-03	-0.7620108E-03	-0.8105423E-03	-0.8422864E-03
	Iteration 9			
Mode 1	-0.1611966E+01			
Mode 2	-0.6841704E-01			
Mode 3	-0.2083609E-01			
Mode 4	0.1259761E-01			
Mode 5	-0.3751256E-02			
Mode 6	-0.1680736E-02			
Mode 7	0.4706744E-03			
Mode 8	-0.8643731E-03			

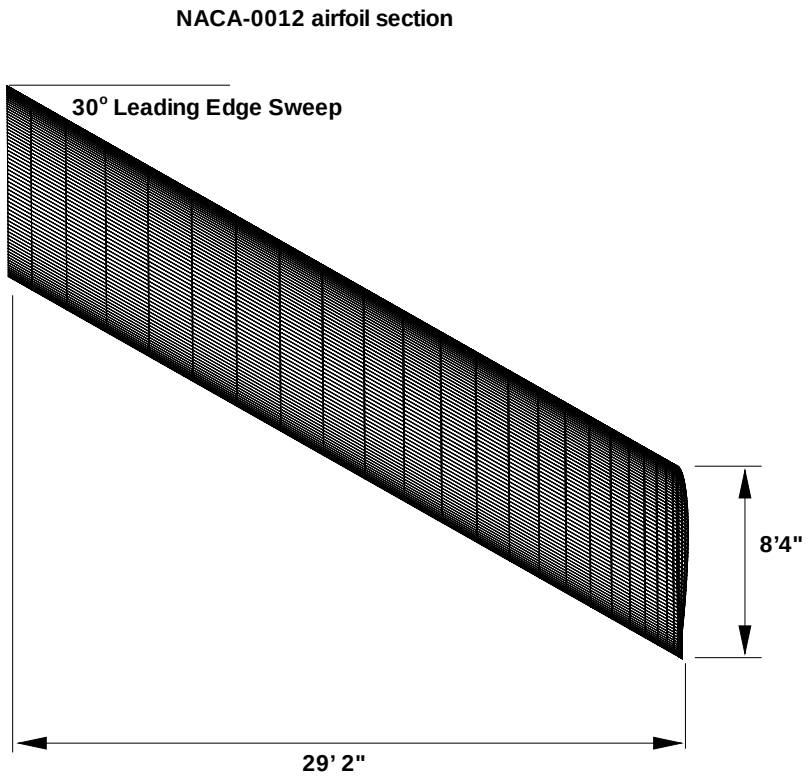

Figure 5.1: Simple Wing Planform Geometry

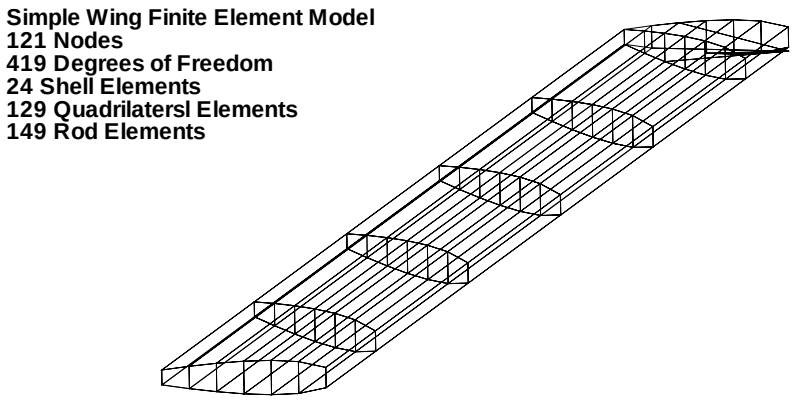

Figure 5.2: Simple Wing Finite Element Model

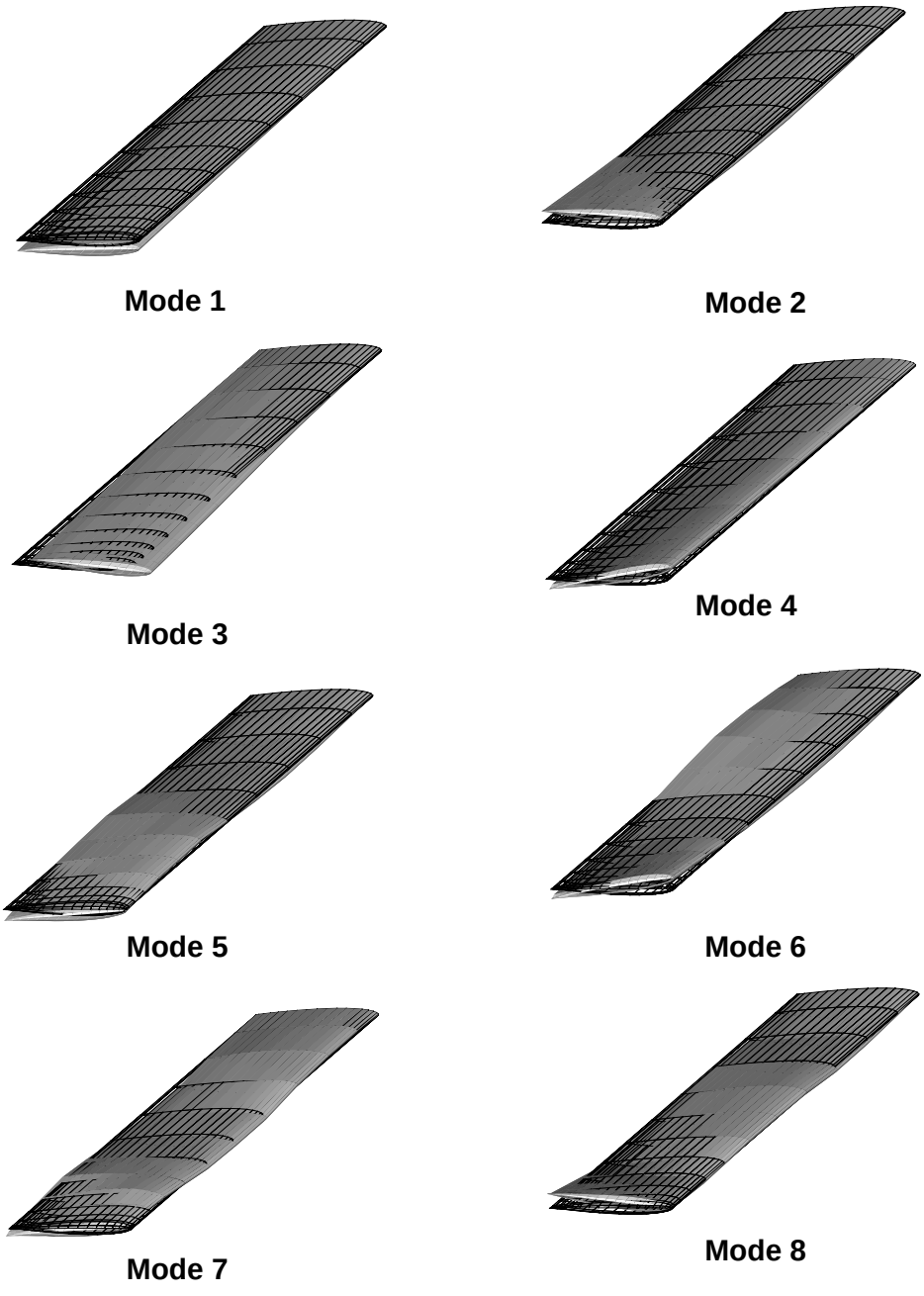

Figure 5.3: Simple Wing Mode Shapes (Mode Shapes are solid grey)

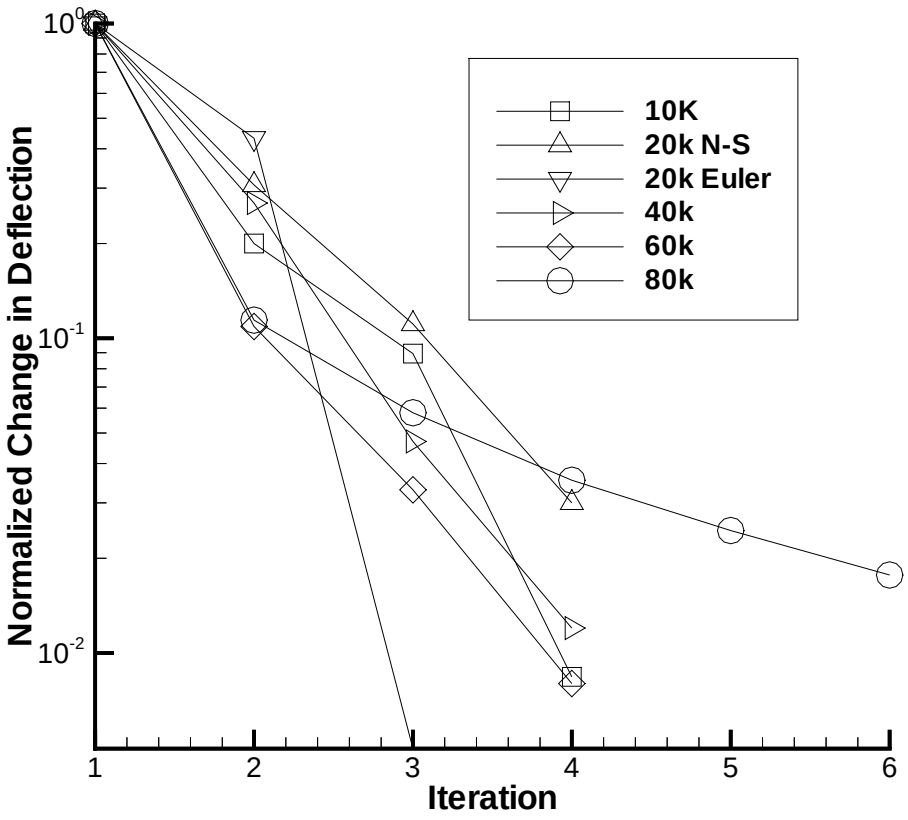

Figure 5.4: Displacement Convergence for Newton's Method Trim Calculations

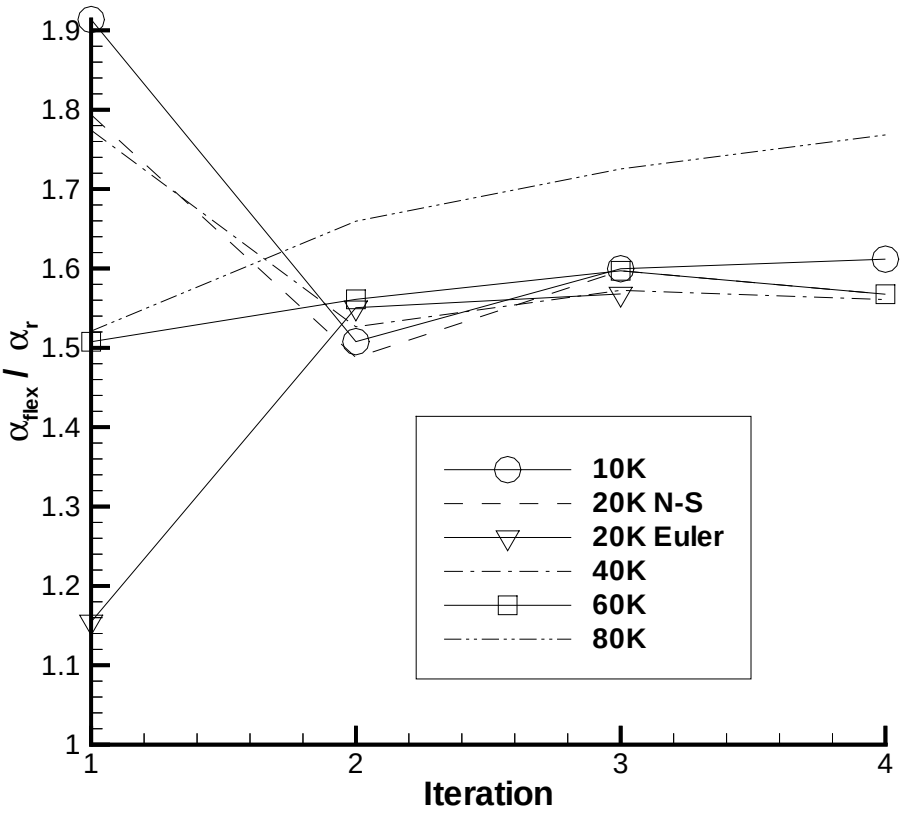

Figure 5.5: Angle of Attack Convergence

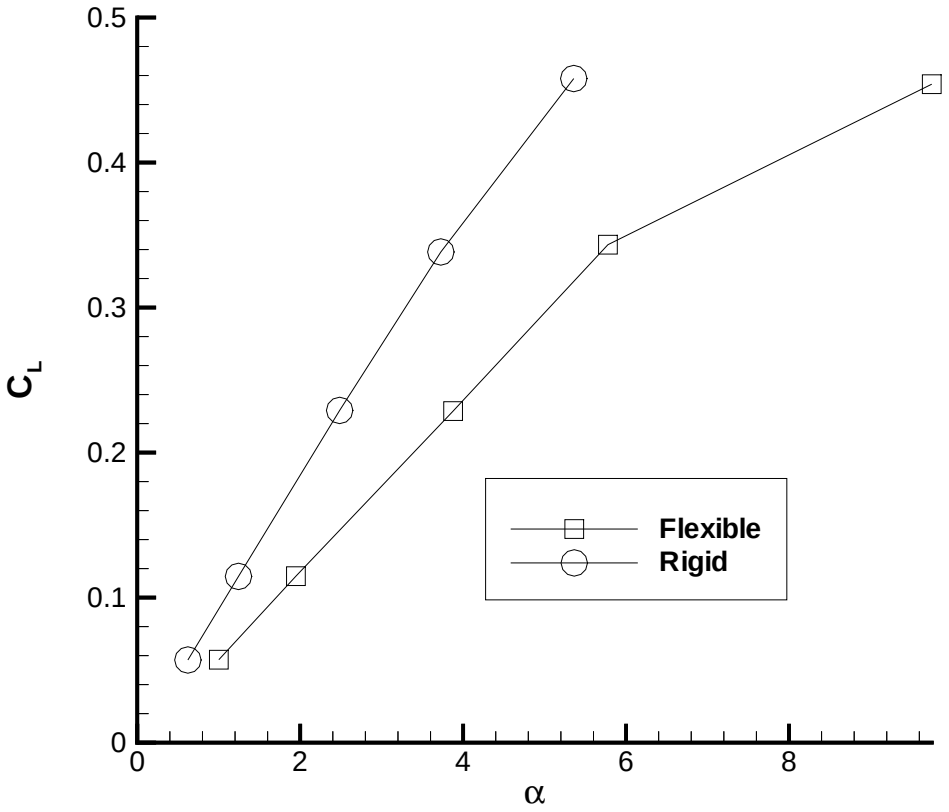

Figure 5.6: C_L vs α for Flexible and Rigid Wing

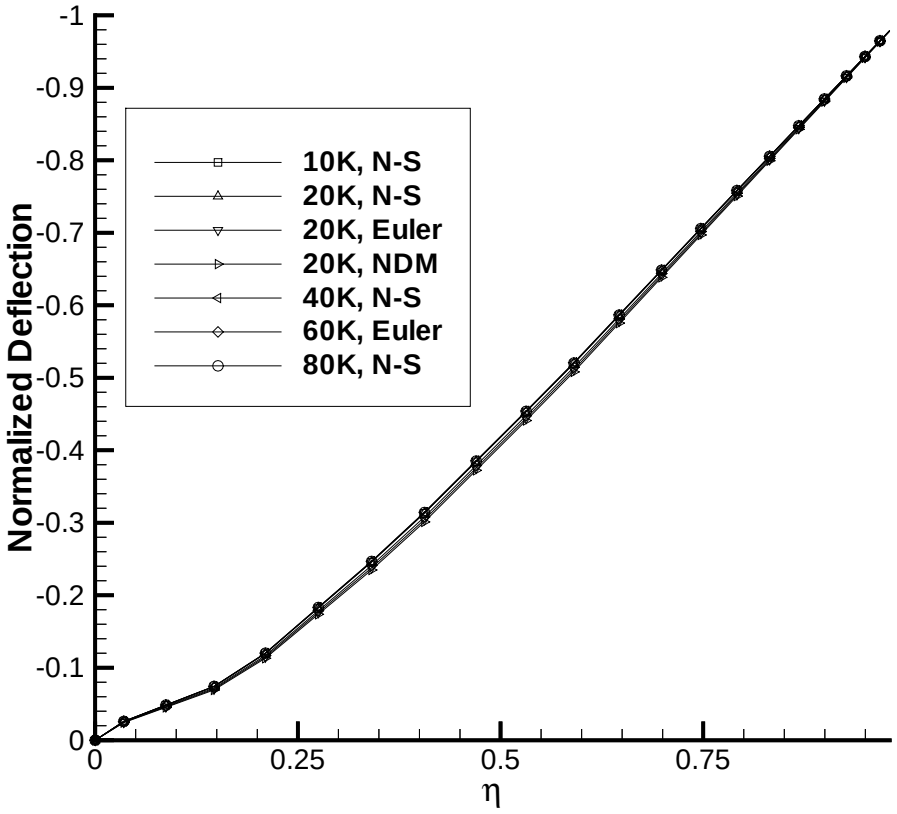

Figure 5.7: Normalized Bending Shapes for all Trim Calculations for the Simple Wing

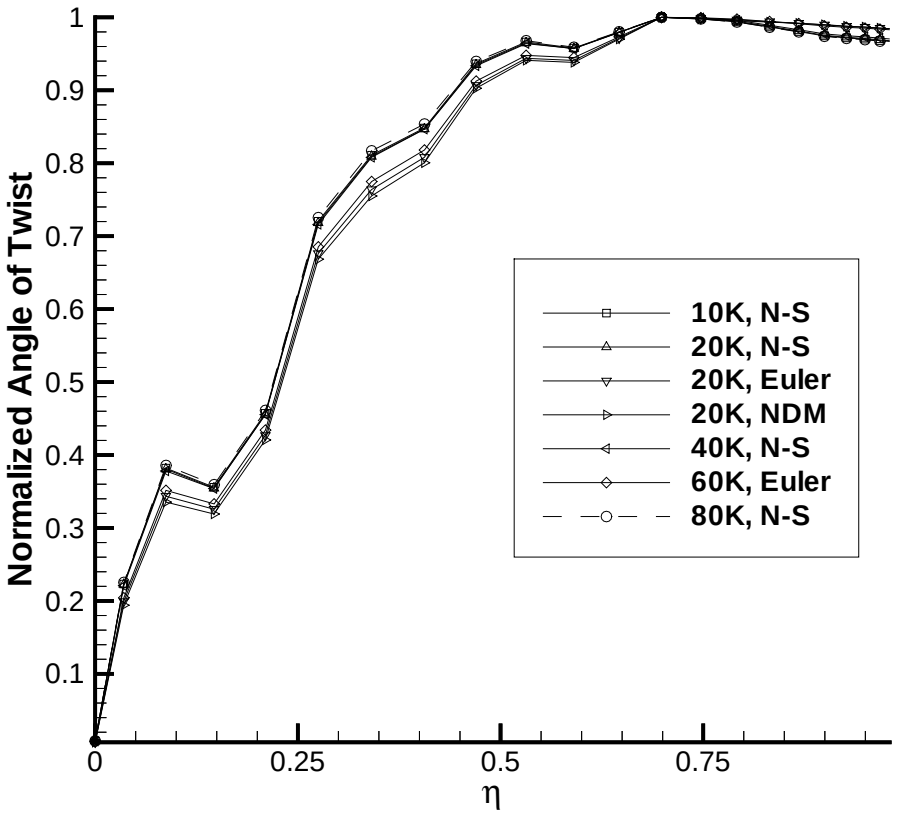

Figure 5.8: Normalized Twisting Shapes for all Trim Calculations for the Simple Wing

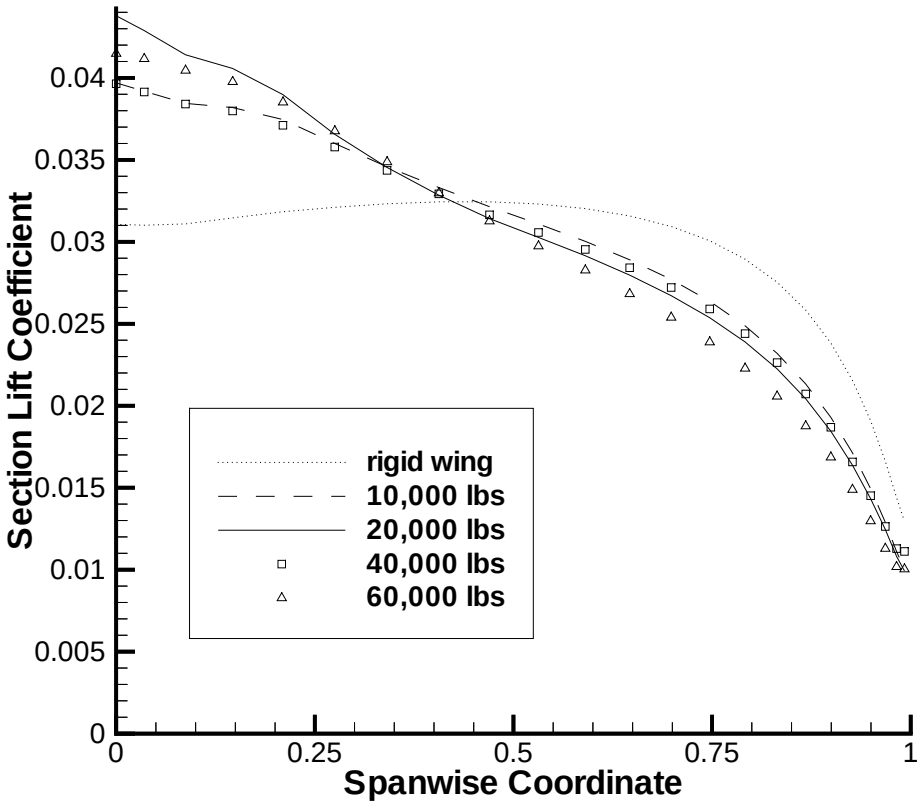

Figure 5.9: Adjusted Spanload Distribution for Trim Calculations

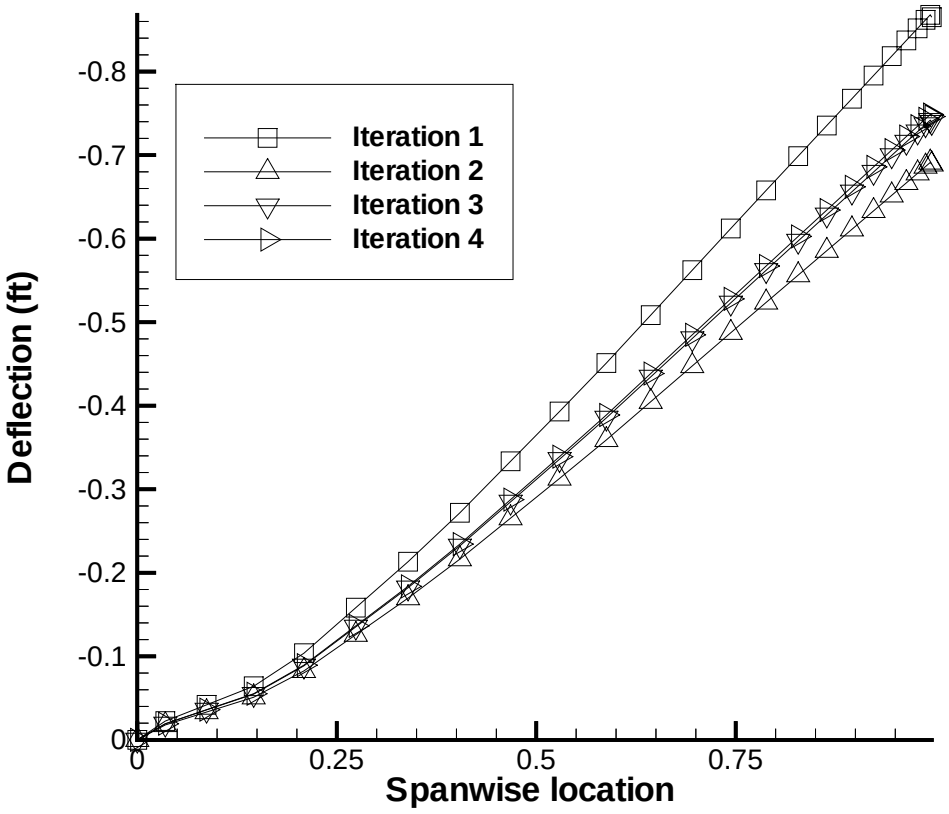

Figure 5.10: Bending Displacement Convergence for 10,000-lbs case, (Navier-Stokes, Newton's Method)

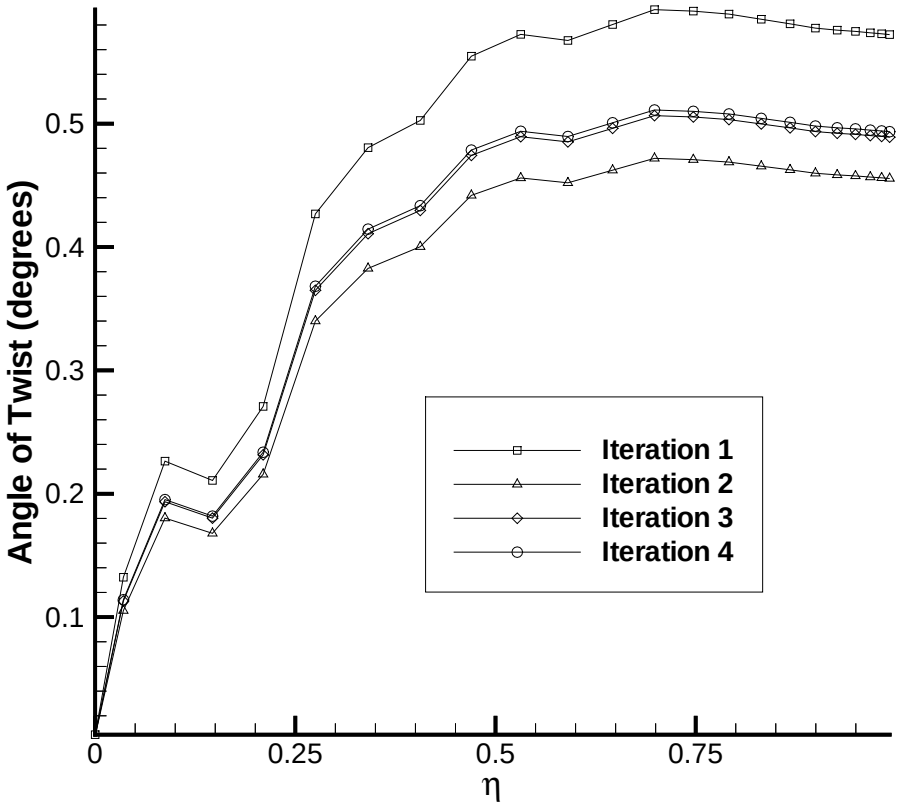

Figure 5.11: Angle of Twist Convergence for 10,000-lbs case (Navier-Stokes, Newton's Method)

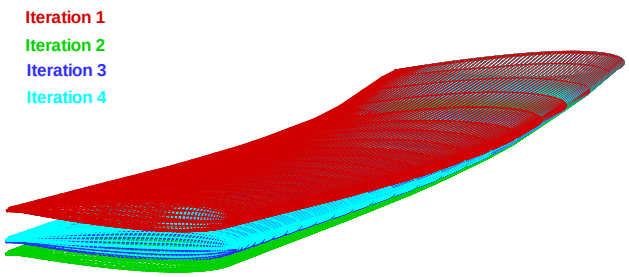

Figure 5.12: Deflection Convergence of the 10,000-lbs case. (Deflections x 10) (Navier-Stokes, Newton's Method)

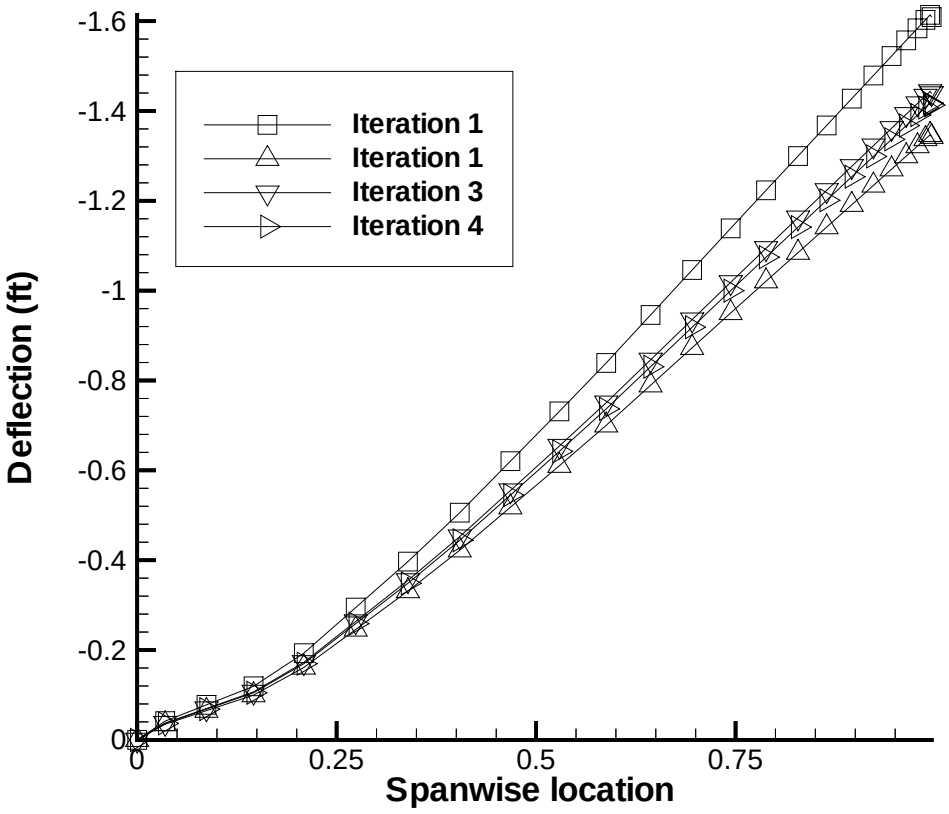

Figure 5.13: Bending Displacement Convergence for the 20,000-lbs case (Navier-Stokes, Newton's Method)

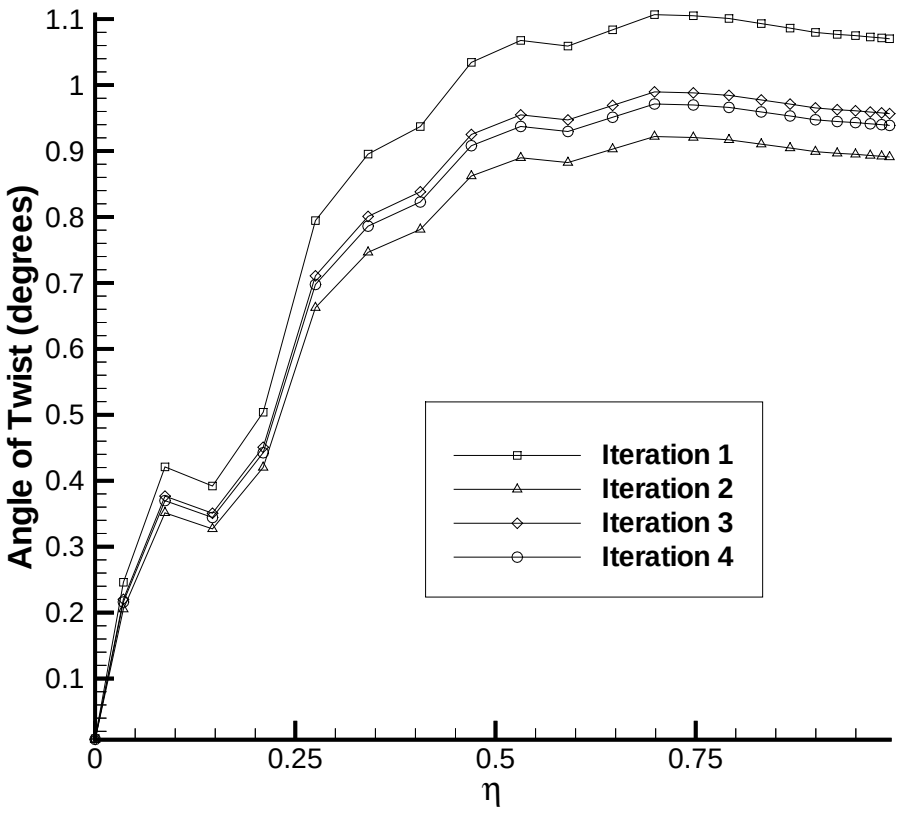

Figure 5.14: Angle of Twist Convergence for the 20,000-lbs case (Navier-Stokes, Newton's Method)

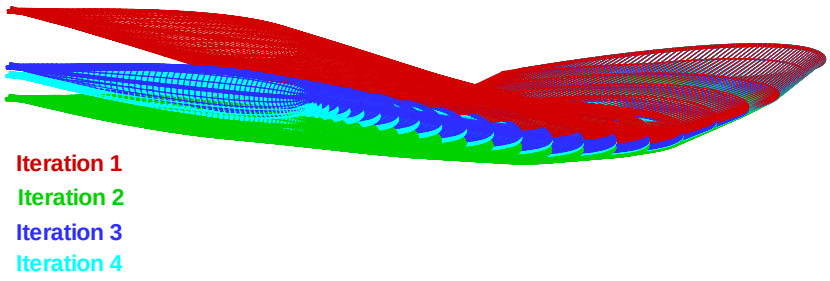

Figure 5.15: Deflection Convergence for the 20,000-lbs case (Navier-Stokes, Newton's Method) (Deflections x 10)

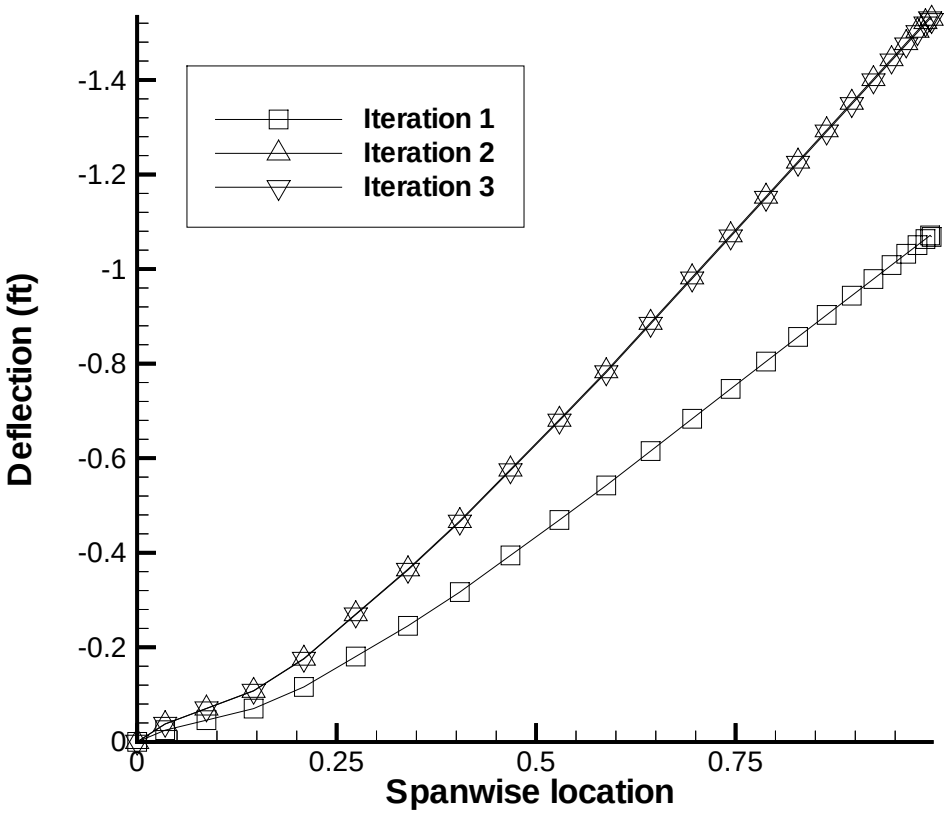

Figure 5.16: Bending Displacement Convergence for the 20,000-lbs case (Euler, Newton's Method)

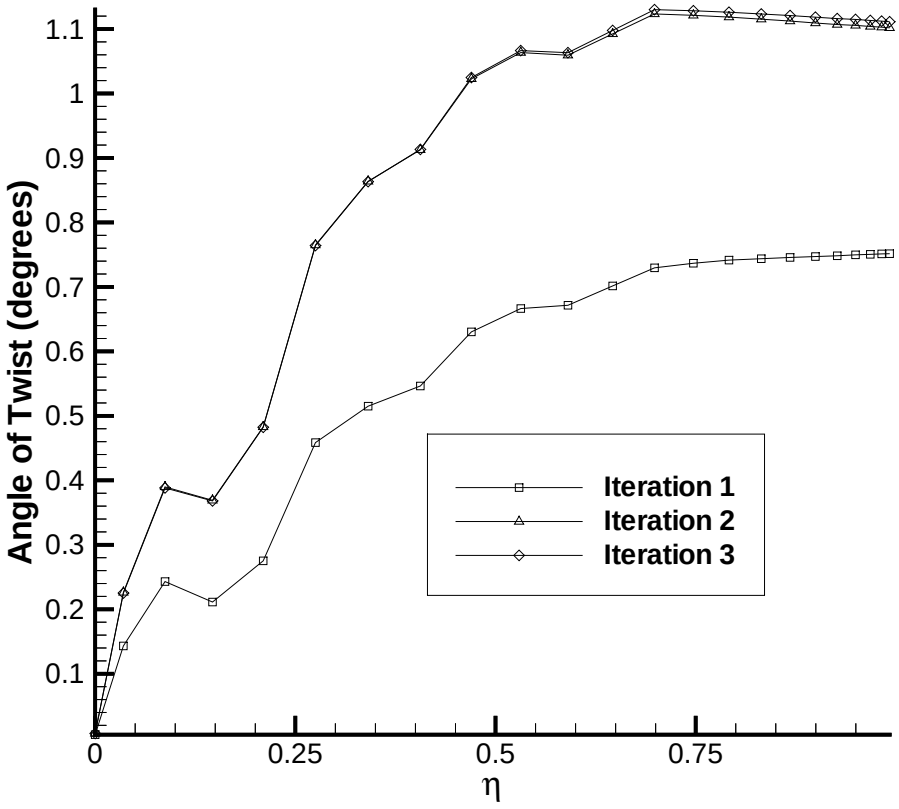

Figure 5.17: Angle of Twist Convergence for the 20,000-lbs case (Euler, Newton's Method)

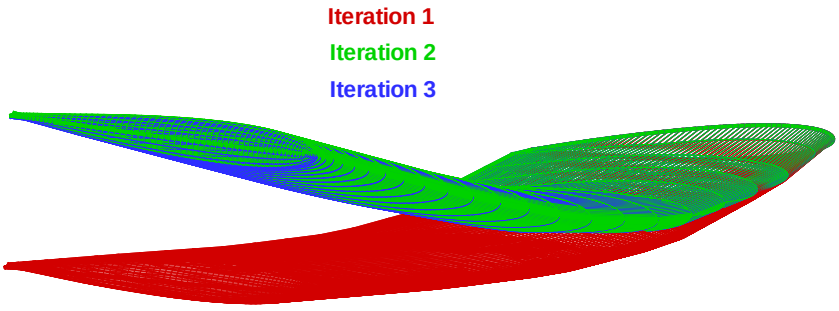

Figure 5.18: Deflection Convergence for the 20,000-lbs case (Euler, Newton's Method) (Deflections x 10)

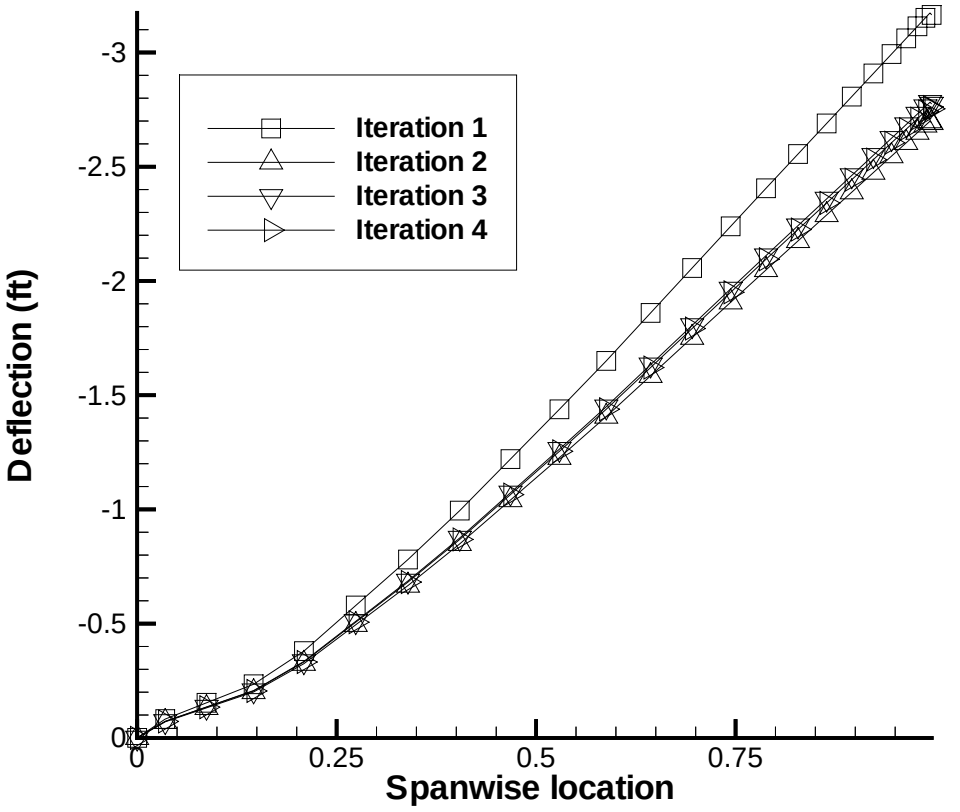

Figure 5.19: Bending Displacement Convergence for the 40,000-lbs case (Navier-Stokes, Newton's Method)

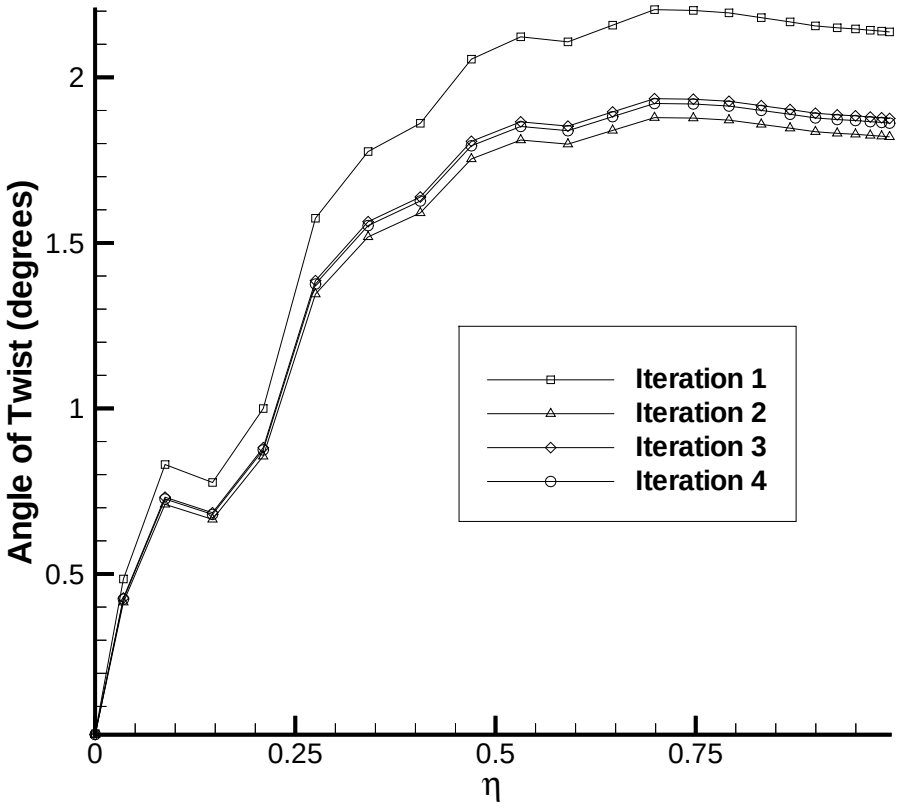

Figure 5.20: Angle of Twist Convergence for the 40,000-lbs case (Navier-Stokes, Newton's Method)

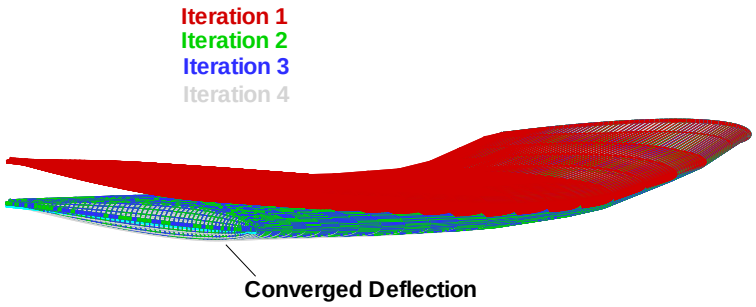

Figure 5.21: Deflection Convergence for the 40,000-lbs case (Deflections x 4) (Navier-Stokes, Newton's Method)

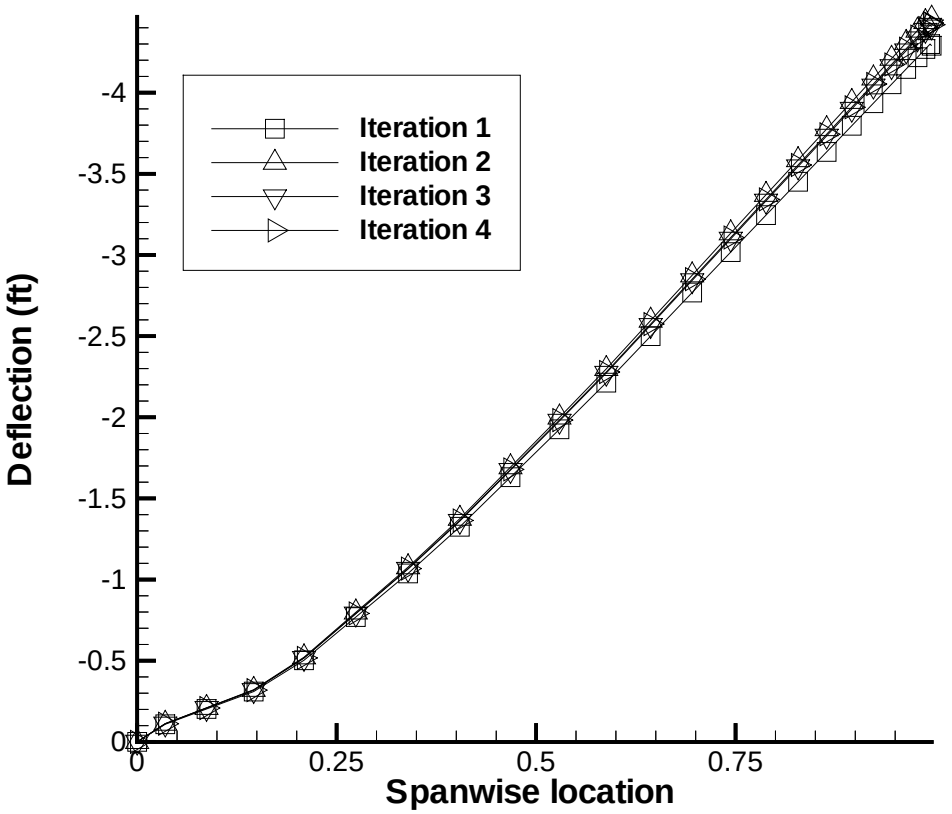

Figure 5.22: Bending Displacement Convergence for the 60,000-lbs case (Navier-Stokes, Newton's Method)

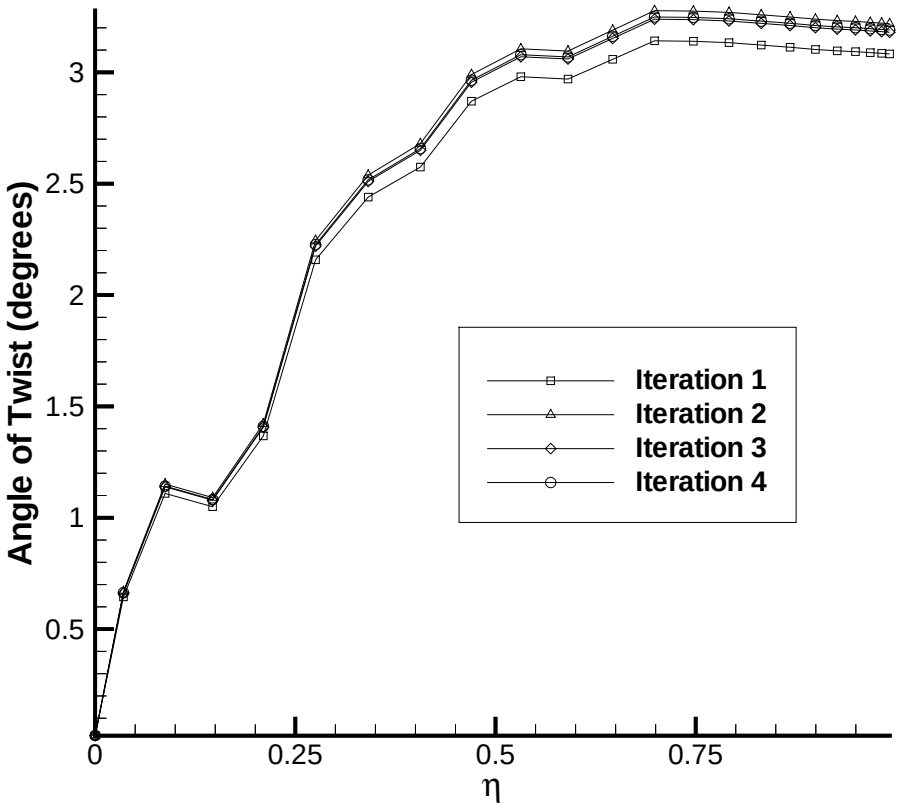

Figure 5.23: Angle of Twist Convergence for the 60,000-lbs case (Navier-Stokes, Newton's Method)

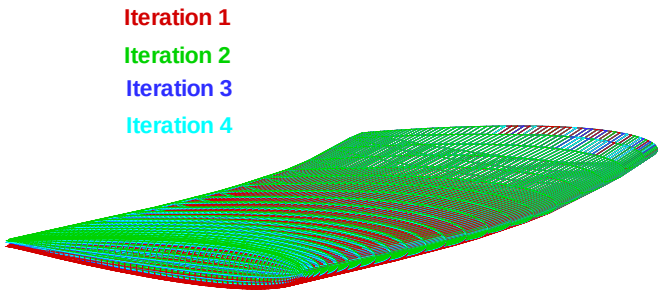

Figure 5.24: Deflection Convergence for the 60,000-lbs case (Navier-Stokes, Newton's Method)

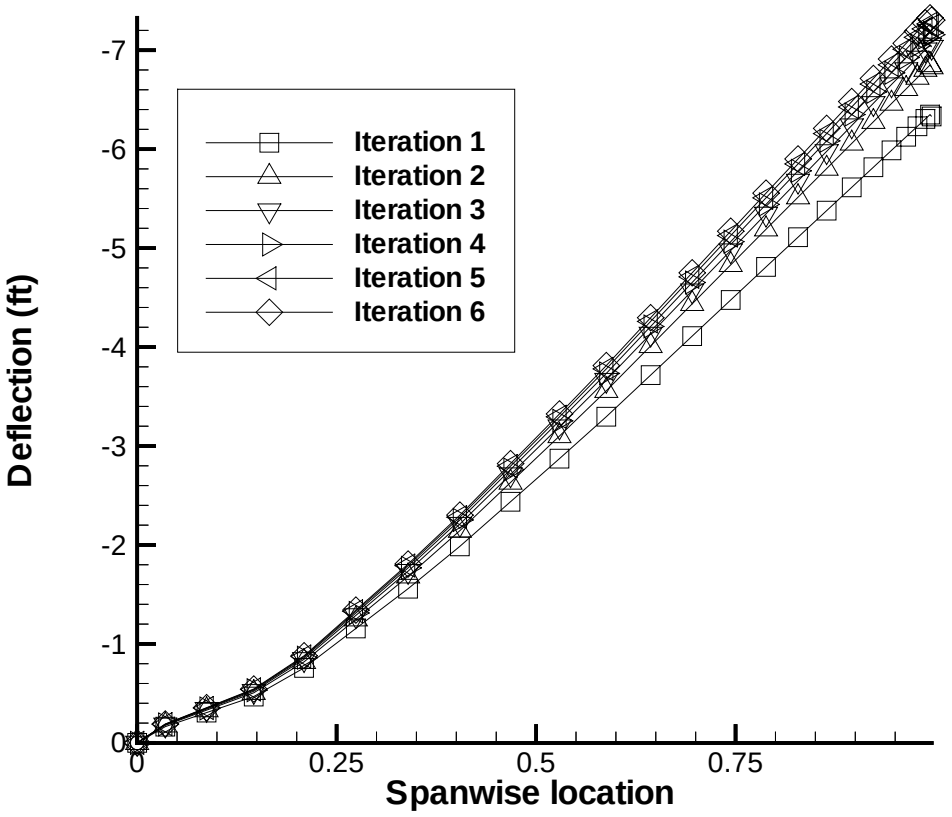

Figure 5.25: Bending Deflection Convergence for the 80,000-lbs case (Navier-Stokes, Newton's Method)

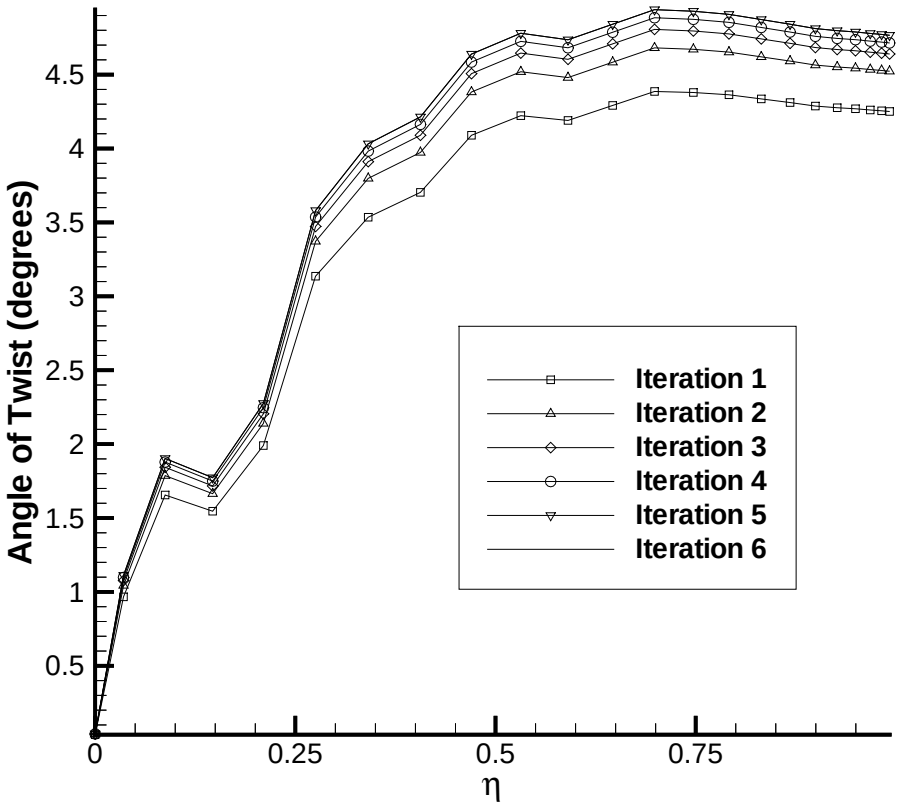

Figure 5.26: Angle of Twist Convergence for the 80,000-lbs case (Navier-Stokes, Newton's Method)

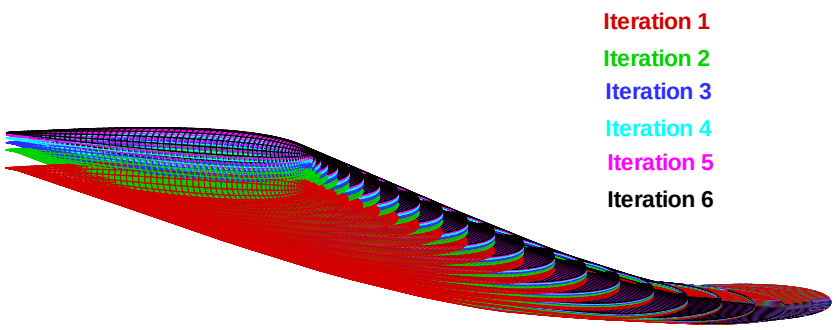

Figure 5.27: Deflection Convergence for the 80,000-lbs case (Navier-Stokes, Newton's Method)

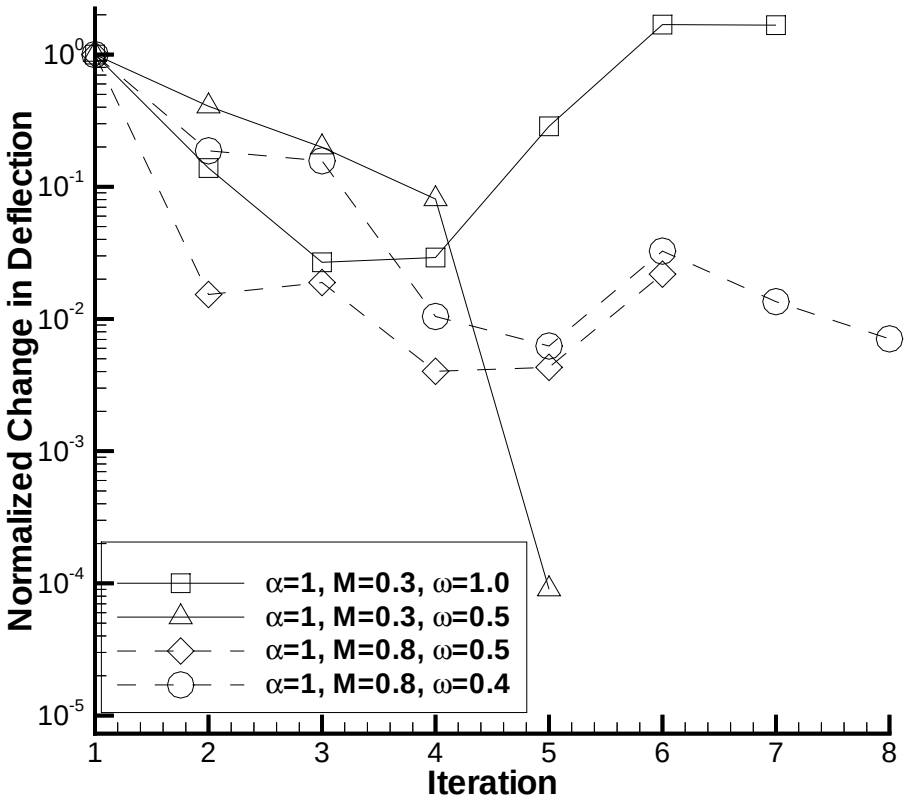

Figure 5.28: Structural Convergence for Fixed α Calculations

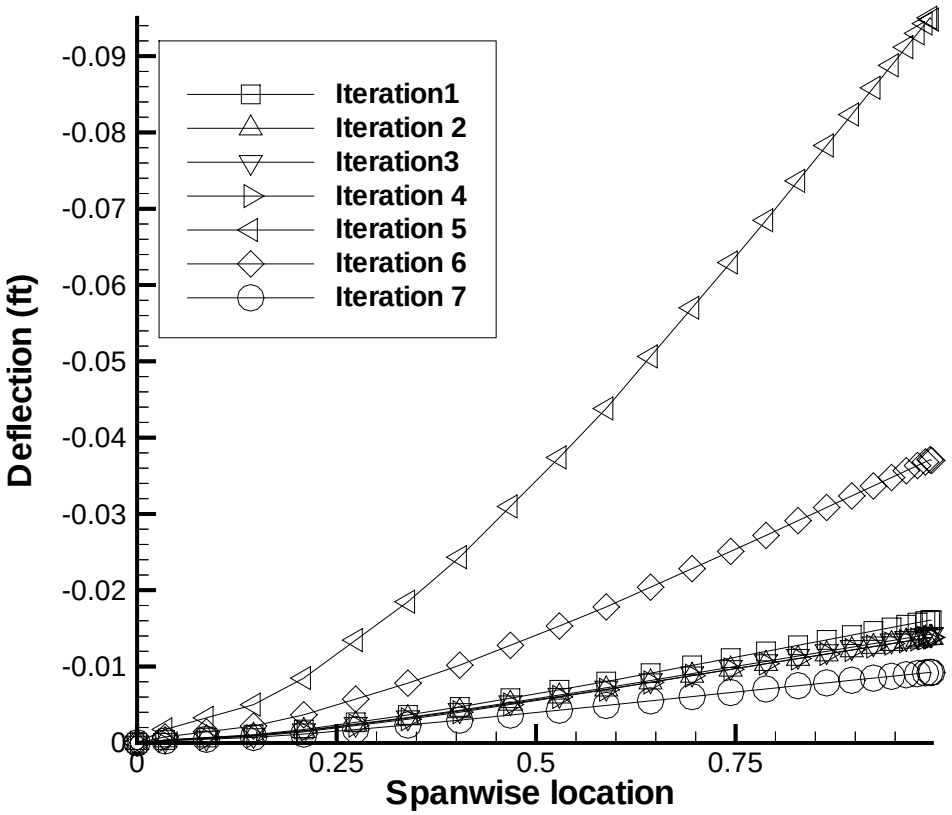

Figure 5.29: Bending Displacement Convergence for $\alpha = 1$, $M = 0.3$, $\omega = 1.0$

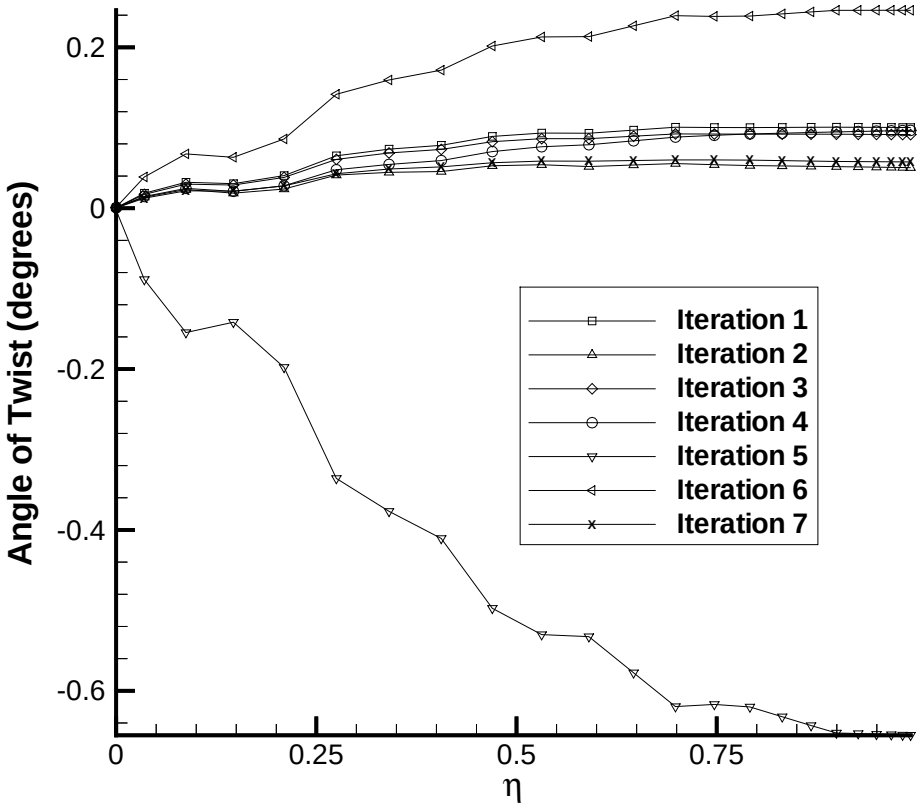

Figure 5.30: Angle of Twist Convergence Using NDM for $\alpha = 1$, $M = 0.3$, $\omega = 1.0$

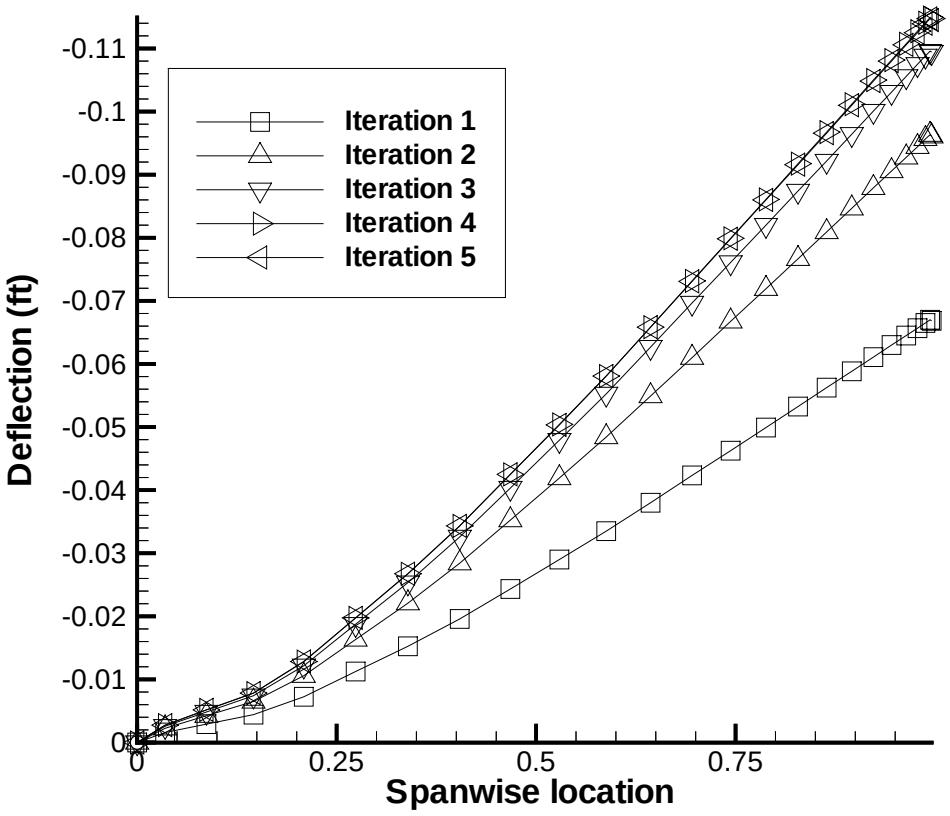

Figure 5.31: Bending Displacement Convergence Using NDM for $\alpha = 1$, $M = 0.3$, $\omega = 0.5$

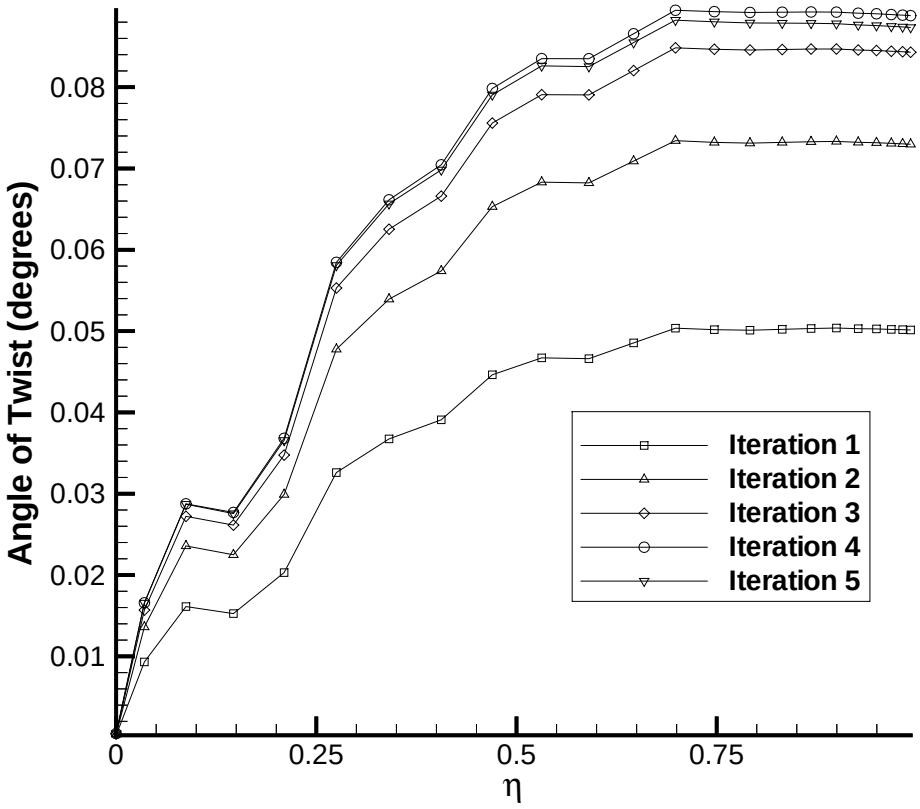

Figure 5.32: Angle of Twist Convergence Using NDM for $\alpha = 1$, $M = 0.3$, $\omega = 0.5$

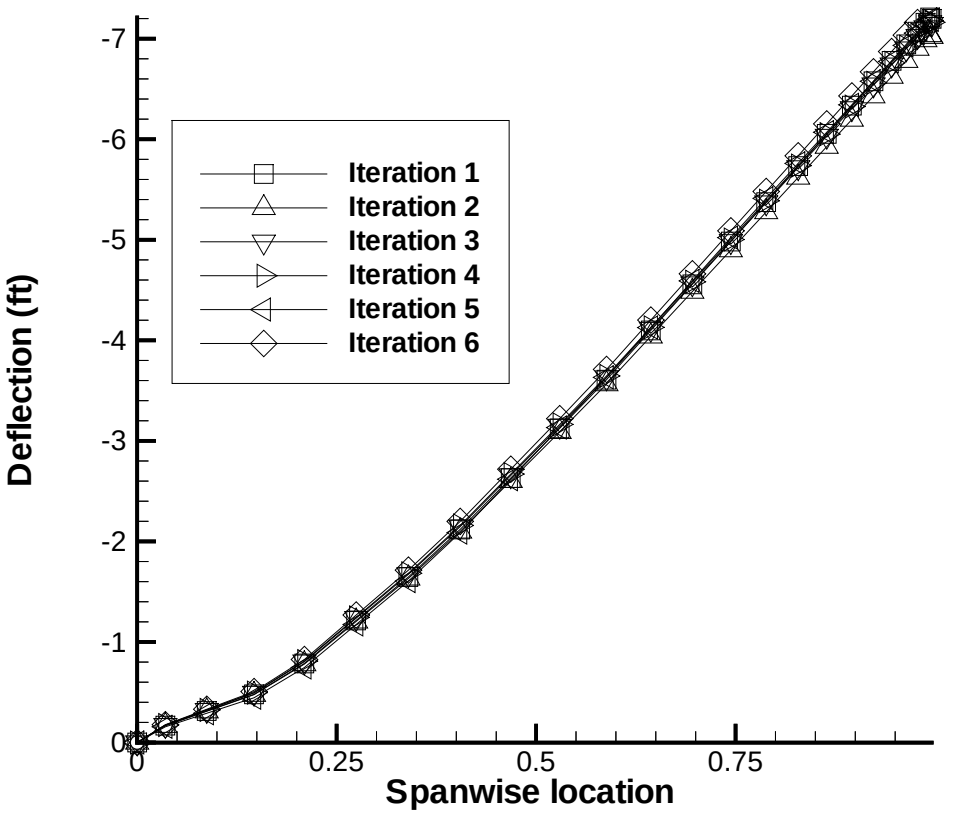

Figure 5.33: Bending Displacement Convergence Using NDM for $\alpha = 1$, $M = 0.8$, $\omega = 0.5$

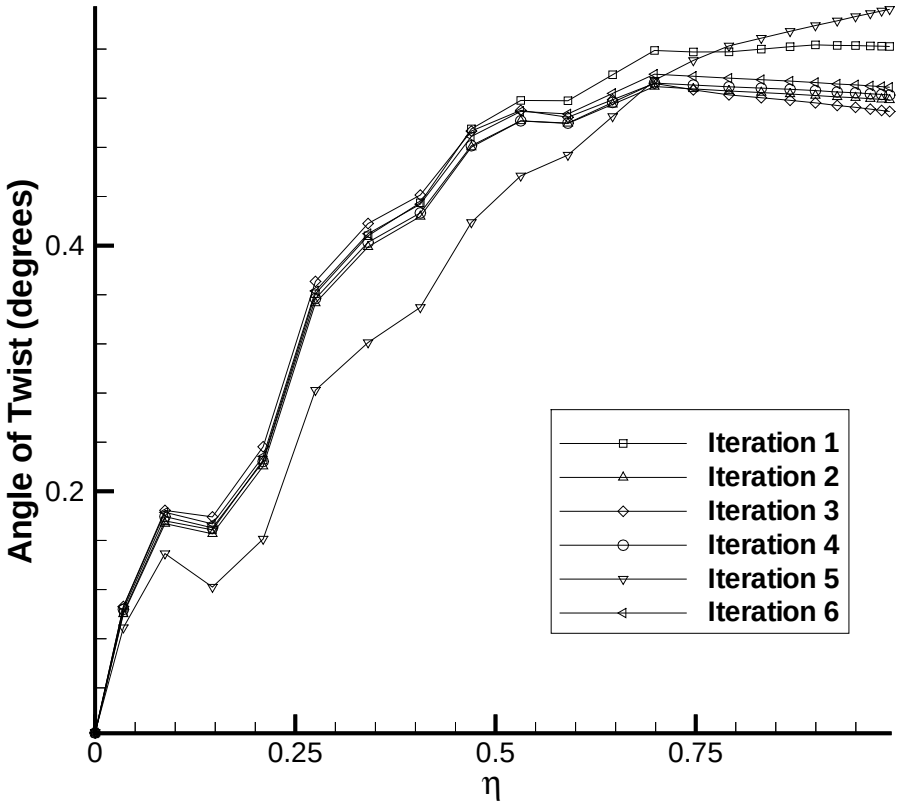

Figure 5.34: Angle of Twist Convergence Using NDM for $\alpha = 1$, $M = 0.8$, $\omega = 0.5$

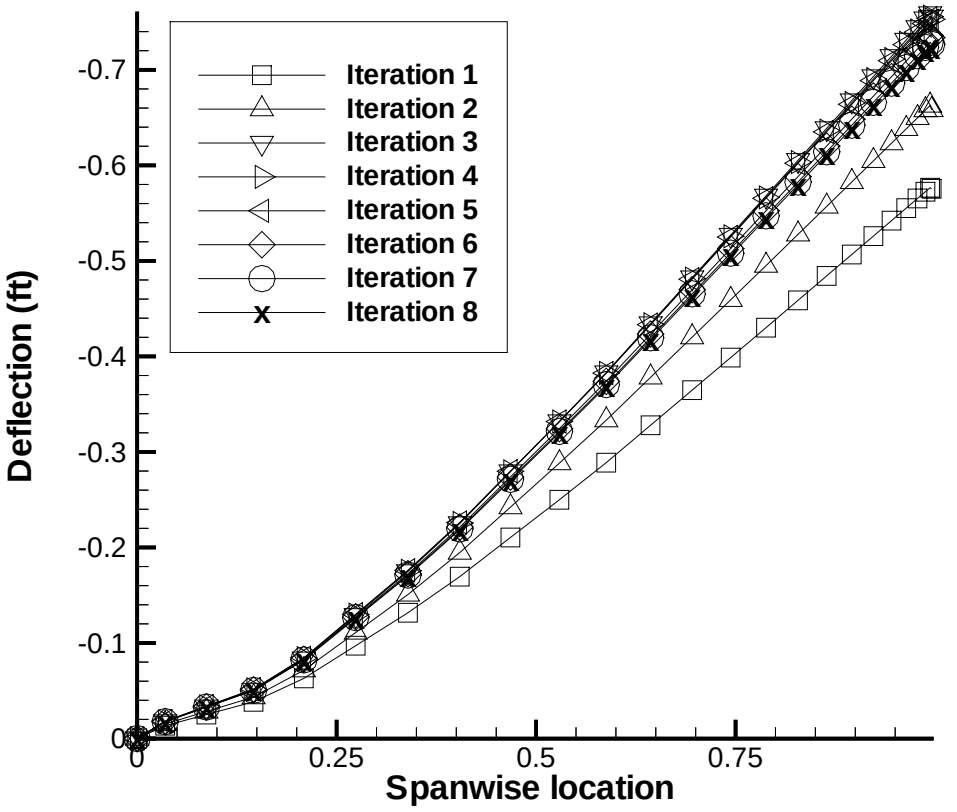

Figure 5.35: Bending Displacement Convergence Using NDM for $\alpha = 1$, $M = 0.8$, $\omega = 0.4$

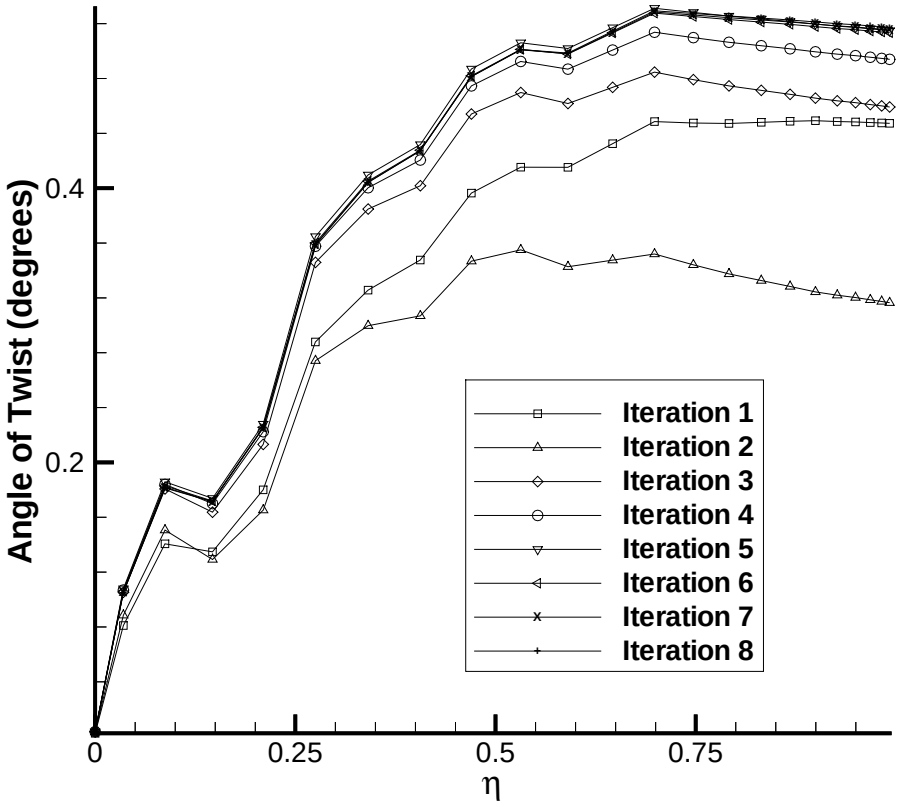

Figure 5.36: Angle of Twist Convergence Using NDM for $\alpha = 1$, $M = 0.8$, $\omega = 0.4$

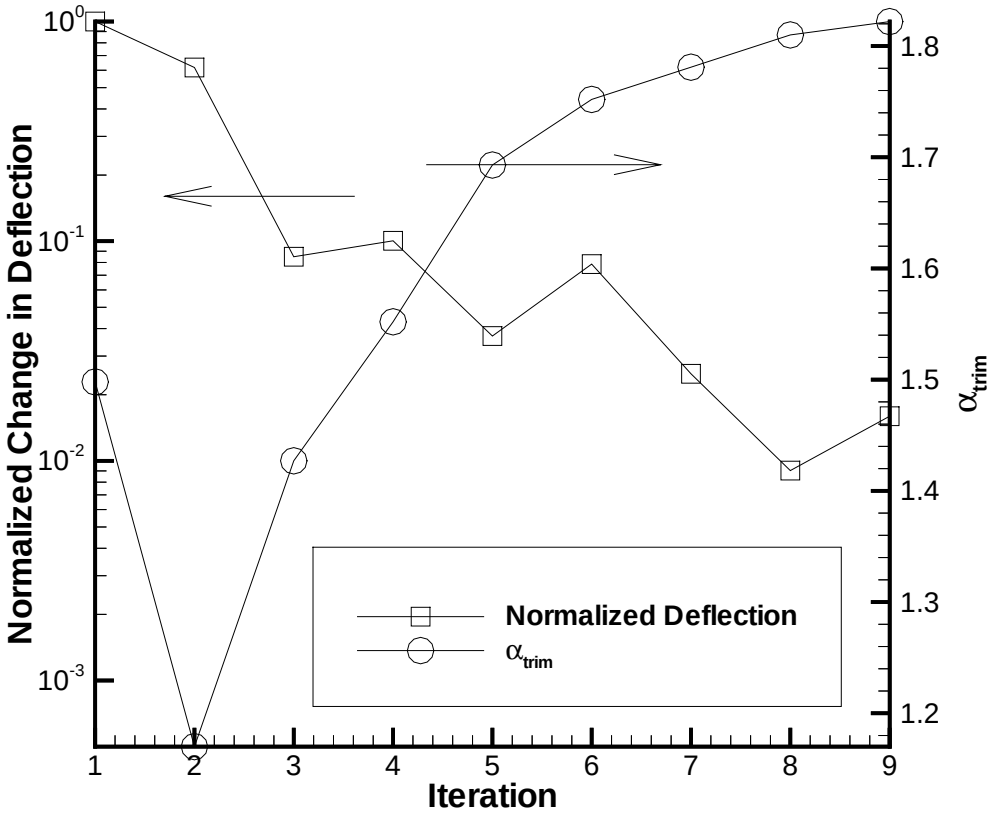

Figure 5.37: Convergence of Non Derivative Trim Calculations

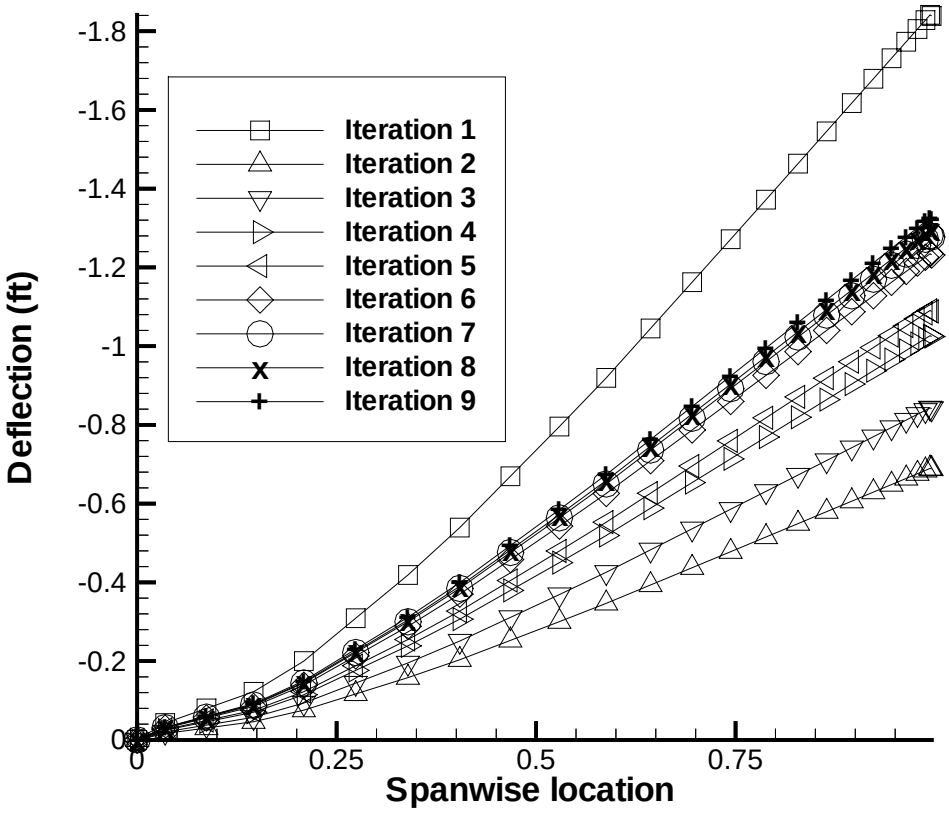

Figure 5.38: Bending Displacement Convergence for the 20,000-lbs Case (Euler, Non Derivative)

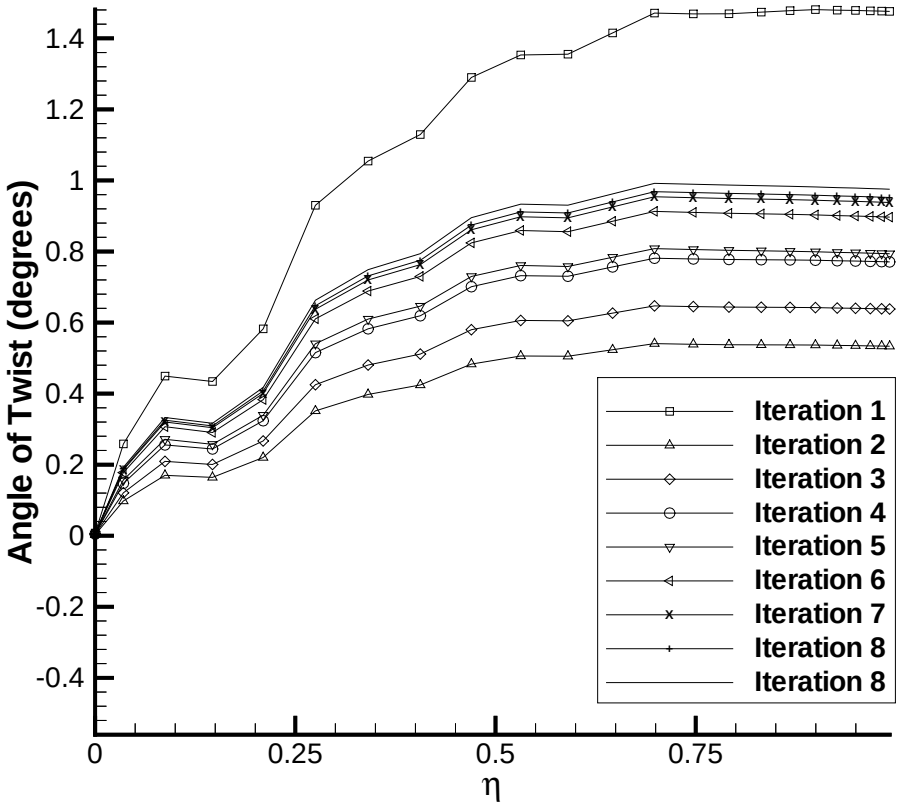

Figure 5.39: Angle of Twist Convergence for the 20,000-lbs Case (Euler, Non Derivative)

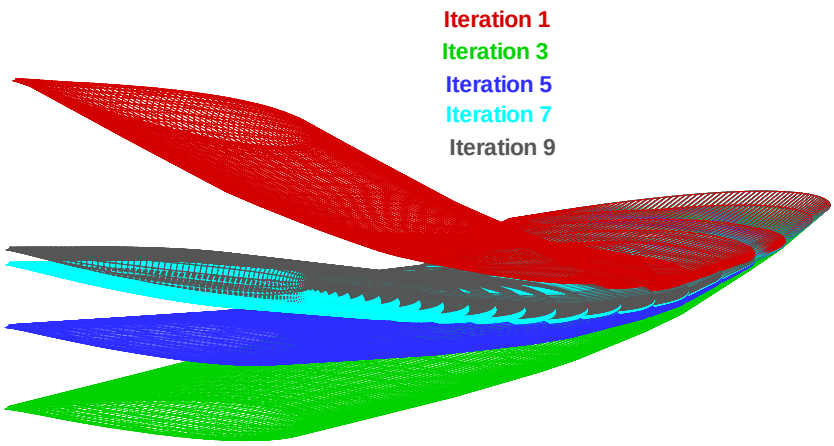

Figure 5.40: Deflection Convergence for the 20,000-lbs Case (Euler, Non Derivative) (Deflections x 10)

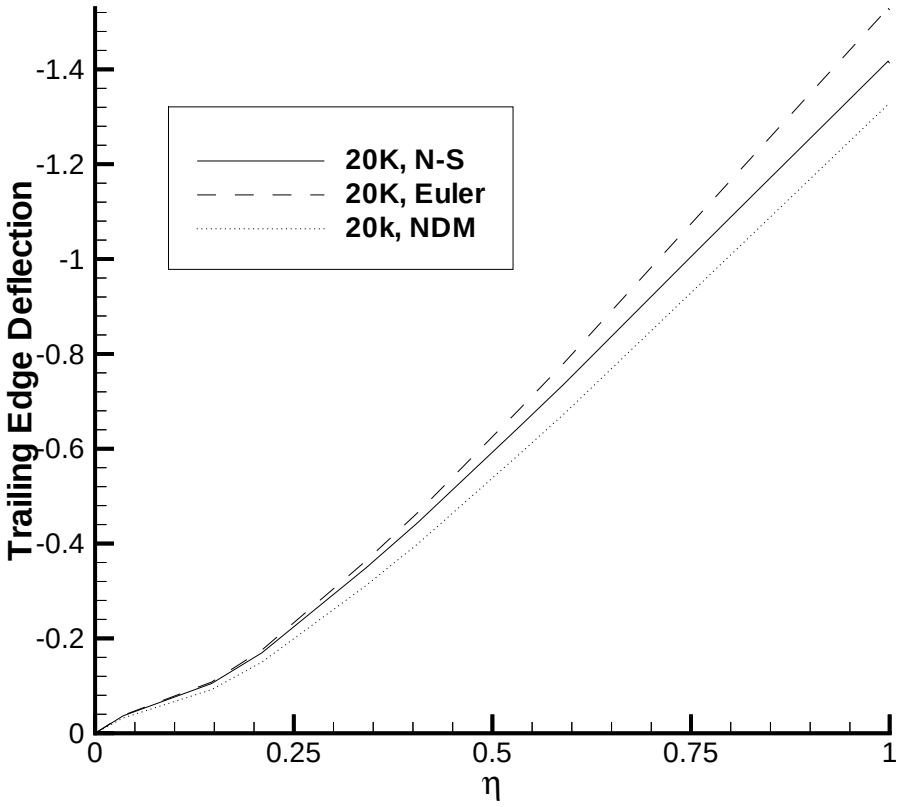

Figure 5.41: Spanwise Variation of the Bending Displacement for the 20,000-lbs Case

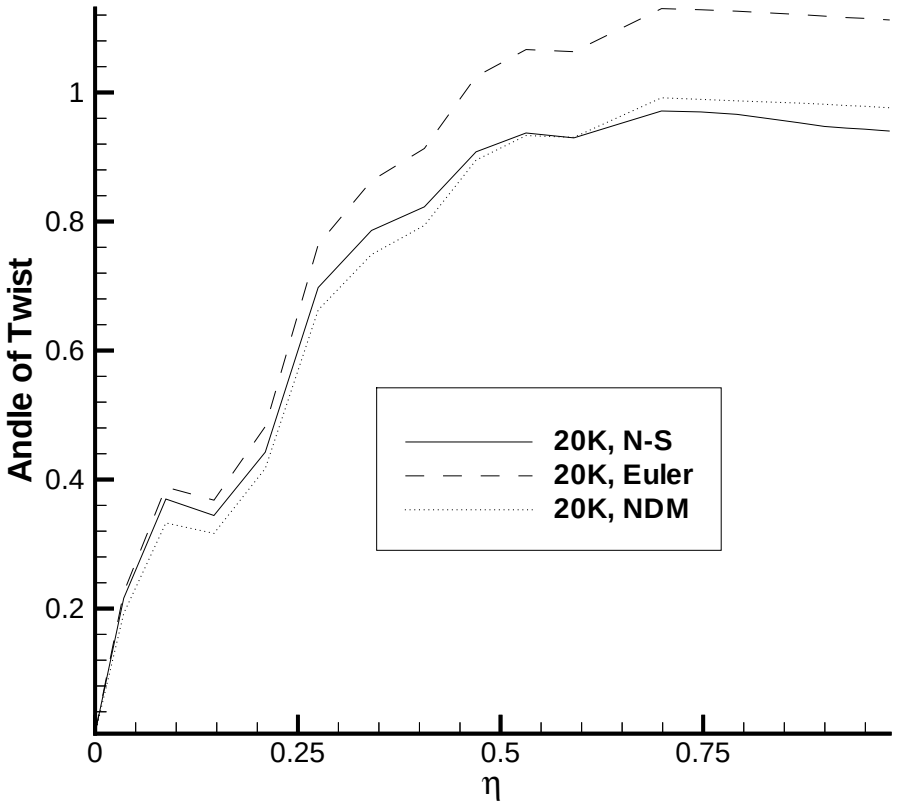

Figure 5.42: Spanwise Variation of the Angle of Twist for the 20,000-lbs Case

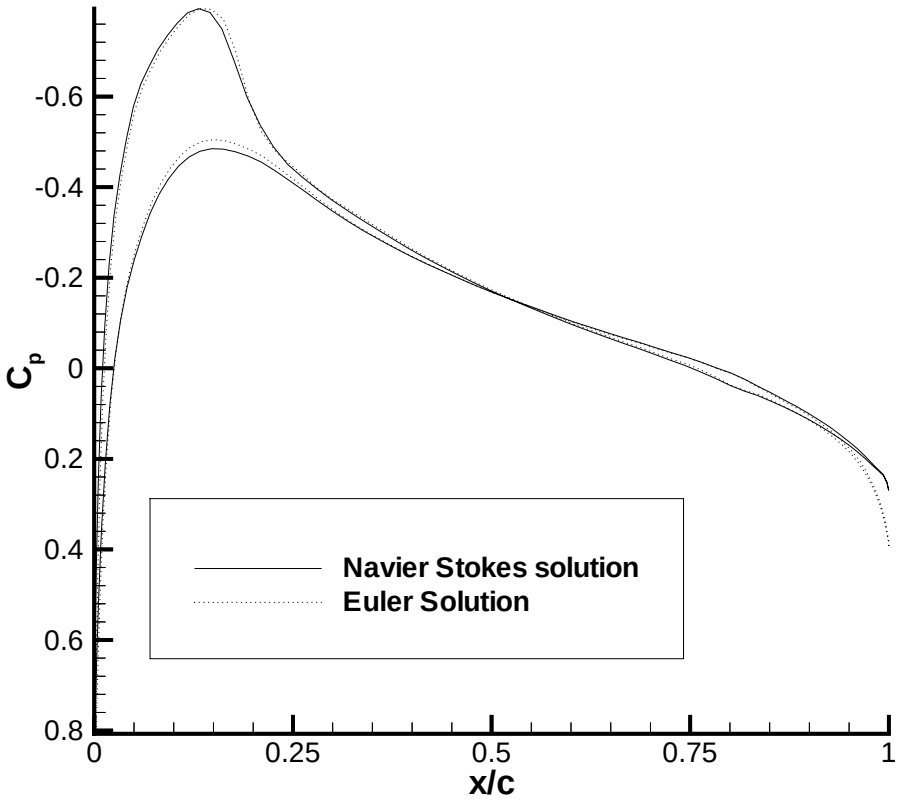

Figure 5.43: Pressure Coefficient at 80% Spanwise Location

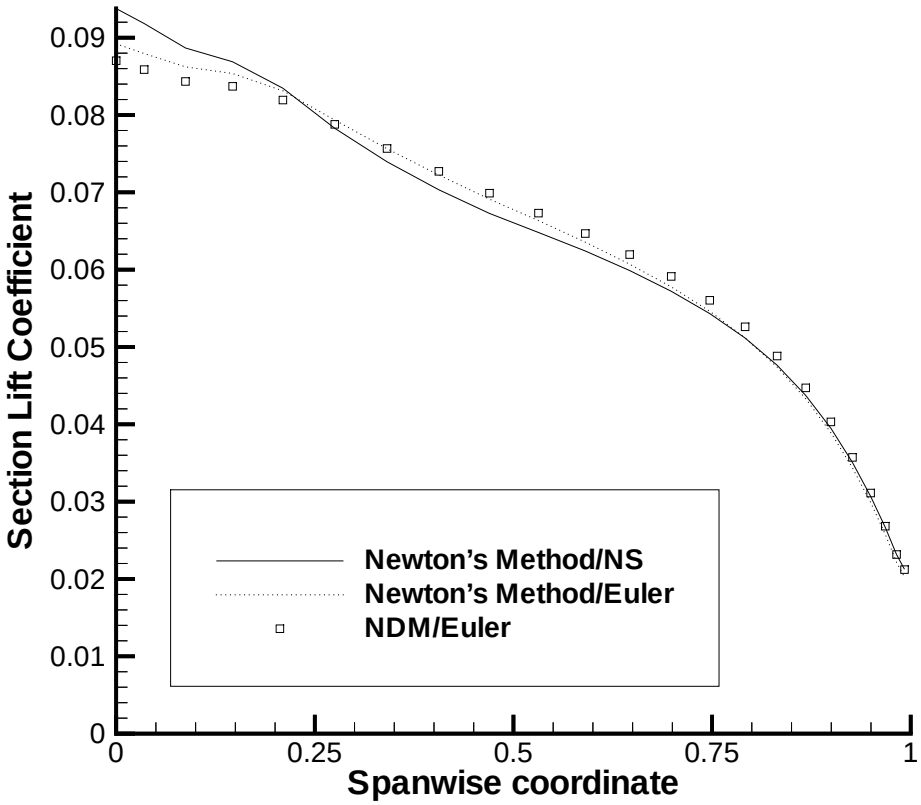

Figure 5.44: Spanload Plot for the 20,000-lbs Case

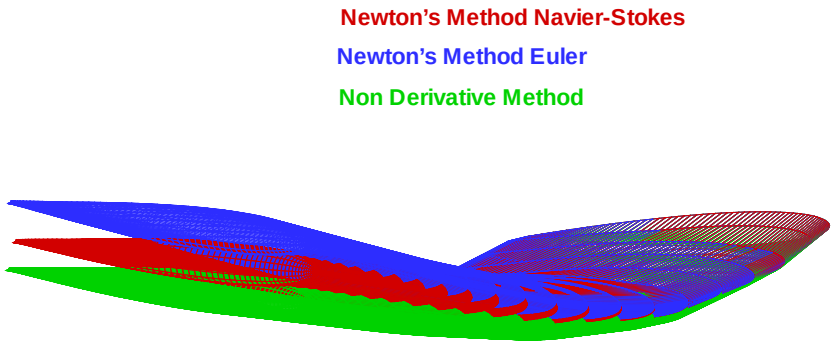

Figure 5.45: Converged Wing Shapes for the 20,000 lbs cases (Deflections x 10)

Chapter 6

ARW Results

6.1 ARW Description

The Aeroelastic Research Wing (ARW)[12] is a wing model for which both experimental,[57,58] and computational[3,55] aeroelastic results are available. For this research the availability of existing computational and experimental results provides a valuable opportunity to evaluate the behavior of the modal approach of structural modeling.

The ARW wing has a leading edge sweep of 28.8^o and an aspect ratio of 10.3. Figure 6.1 shows the planform geometry of the ARW wing. The airfoil section was originally formed from three different supercritical airfoil sections with differing thicknesses. A straight line interpolation was used between the defined airfoil stations.[12] The section was chosen based on a flight condition of Mach 0.8 and an altitude of $46,800ft$. The geometry of the ARW wing is the jig shape of the wing that was formulated based on the above conditions. The jig shape is the shape an elastic wing deforms to in the absence of aerodynamic loads and vehicle weights. A wing with no external loads will assume the jig shape as the aircraft is sitting on the runway.

The Finite element model of the wing was generated by Bhardwaj.[3] It has 312 nodes, and is composed of 56 axial bar elements and 896 Allman's triangular elements.

It has 1872 degrees of freedom. (See figure 6.2). The mode shapes used in this research generated by NASTRAN are shown in Figure 6.3.

The CFD grid has dimensions of 187 points around the chord, 39 points out the span of the wing and 45 points normal to the wing. It is the same surface grid used by Bhardwaj[3] in his CFD calculations and used by Farhangnia *et al.* in their analysis.[55] Farhangnia *et al.* combined a Navier-Stokes analysis of the fluid with a modal approach to the structures, using 5 mode shapes. The aeroelastic solution is run at $Mach = 0.85$, $\alpha = 1^0$ and at a dynamic pressure of $200psf$. The results presented were generated using GASPv3 solving the Euler equations on an SGI Power Challenge. Results are compared with those of Bhardwaj,[3] Farhangnia et al.[55] and with available experimental data.[58]

In addition, a Newton's method trim calculation was performed using the lift generated by the converged solution of the fixed α calculation.

6.2 Fixed Angle of Attack Results

Table 6.1 shows the modal amplitudes as a function of the convergence of the fixed angle of attack calculation. Convergence was determined using the same method as for the non derivative calculations for the simple wing. Structural Convergence is presented in figure 6.4. Convergence is plotted as $||\Delta q||_2$ vs iteration. A relaxation factor of 0.4 was used for this calculation.

Converged values of deflection along the front and rear spar of the wing are presented in figures 6.5 and 6.6. Rear spar data is available from Farhangnia *et al.*[55] The results from Farhangnia *et al.* were generated using 5 mode shapes and the Navier Stokes equations and the deflection of the wing is overpredicted by these results when compared with the experimental results. The results of Bhardwaj[3] calculated using finite element results coupled with a Navier Solution show good agreement with experimental results in predicting deflection.

Along the front spar more deflection is predicted using the Euler equations than with the results from Bhardwaj.[3] Along the rear spar, again deflection is overpredicted When compared with results from Bhardwaj and experimental results. Results generated using the Euler equations and the modal analysis agree with the results of Farhangnia for the deflection along the rear spar however. When compared with the results of Bhardwaj and the experimental results, the solution generated in this research using the Euler equations shows a greater increase in deflection along the front spar than along the rear spar. This corresponds to a local increase angle of attack outboard. This is consistent with the results from the 20,000 lbs case in the previous chapter which showed a decrease in twist angle for inviscid results when compared with viscous results.

A plot of spanload (Figure 6.7) shows an increase in lift outboard for the inviscid results when compared to the viscous results generated by Bhardwaj. This is also consistent with what is seen in the results in the previous chapter. Note that the spanload plot does not go to zero at the wingtip. This is an effect of the topology of the CFD grid near the wingtip.

Comparing the pressure coefficient distribution at the 70.7 % semi span location (Figure 6.8) shows agreement with available results and is consistent with the differences in spanload. The pressure coefficient results seem to show an increase in lift for the inviscid results which could result in the increased deflection seen for the Euler calculations. The increase in local lift shown in the pressure coefficient distribution could be a result of the increased local angle of attack for the Euler solution. The deflected shape is shown in Figure 6.9 compared to the jig shape. Chordwise deflection is plotted in Figure 6.10 and shows an almost linear distribution of vertical deflection between the leading and trailing edge at the 70.7

6.3 ARW Trim Calculation

The resultant lift from the above calculations was used as a starting point for a trim calculation for the ARW wing. Results are presented in Table 6.2. The trim calculations were started from the jig shape at $\alpha = 0^0$. Convergence behavior was consistent with results from the simple wing. Using the error in lift as the convergence criteria, the error was reduced to on the order of one percent in four iterations. Structural convergence is presented in figure 6.11. The numerical values of the modal amplitudes are presented in Table 6.3.

Table 6.1: Convergence of Modal Amplitudes for Fixed Angle of Attack Calculation for ARW Wing, $\alpha = 1^0$ (Euler)

	modal amplitude			
ARW FPI, $\alpha = 1^0$				
	Iteration 1	Iteration 2	Iteration 3	Iteration 4
Mode 1	-0.2612830E+00	-0.1728279E+00	-0.1375672E+00	-0.1098983E+00
Mode 2	-5.8576223E-03	-3.7892782E-03	-3.5783628E-03	-2.0034598E-03
Mode 3	-1.7098743E-02	-3.2623173E-02	-3.9361274E-02	-4.6819743E-02
Mode 4	3.7054380E-04	9.0691937E-04	2.8612361E-03	3.1916874E-03
Mode 5	-1.8907408E-03	-2.4394681E-03	-2.3069371E-03	-4.7178630E-03
Mode 6	7.5191419E-05	2.3967216E-05	-3.4149671E-05	-2.8627893E-05
Mode 7	-2.1810397E-04	-2.2648790E-04	-3.4493270E-04	-3.9387110E-04
Mode 8	-2.6383401E-05	-3.4849137E-05	-1.0396810E-05	-1.4464121E-05
	Iteration 5	Iteration 6		
Mode 1	-0.8225982E-01	-0.8324824E-01		
Mode 2	-1.5043281E-03	-1.5994213E-03		
Mode 3	-5.1687116E-02	-5.2167075E-03		
Mode 4	3.8141411E-03	3.0234831E-03		
Mode 5	-5.0031698E-03	-5.2672135E-04		
Mode 6	-2.1498734E-05	-2.2928027E-04		
Mode 7	-5.1961137E-05	-5.5311750E-05		
Mode 8	-1.6798124E-05	-1.7023662E-05		

Table 6.2: Convergence history of Trim Calculations for ARW Wing (Euler)

$L_{Des} = 2400lbs$			
Iteration	α	Lift	Error
1	1.3092	2928	19.7
2	0.949023	2301	5.70
3	0.989011	2401	1.60
4	0.995090	2429	0.45

Table 6.3: Convergence of Modal Amplitudes Trim Calculation for ARW Wing (Euler)

	modal amplitude			
ARW Trim Calculations				
	Iteration 1	Iteration 2	Iteration 3	Iteration 4
Mode 1	-1.0020982E-01	-0.7083920E-01	-0.8120092E-01	-0.8302398E-01
Mode 2	-1.9060120E-03	-2.4007502E-03	-1.9082712E-03	-1.6002398E-03
Mode 3	-7.9089707E-03	-5.7978270E-03	-5.3080773E-03	-5.2209807E-03
Mode 4	1.7868712E-03	2.4049021E-03	2.9482891E-03	3.0191809E-03
Mode 5	-2.998089‘E-04	-4.7034752E-04	-5.1112659E-04	-5.2092817E-04
Mode 6	-9.4008971E-04	-1.4004908E-04	-1.9978540E-04	-2.1909918E-04
Mode 7	-1.3897861E-05	-7.8709054E-05	-5.9897235E-05	-6.0019018E-05
Mode 8	-0.7973892E-06	-1.3230739E-05	-1.5401098E-05	-1.6787892E-05

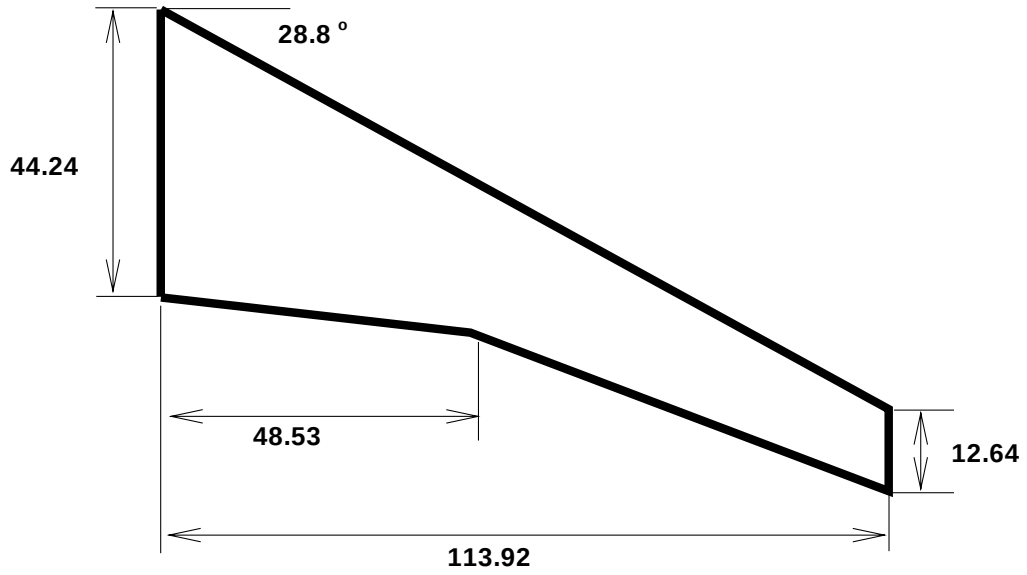

Figure 6.1: ARW Planform Geometry (all dimensions in inches)

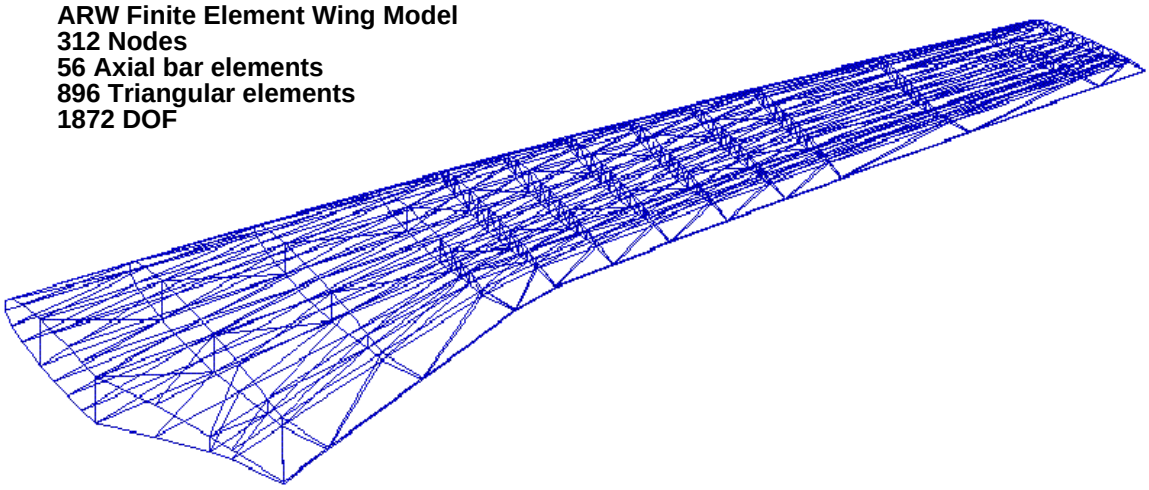

Figure 6.2: ARW Finite Element Model

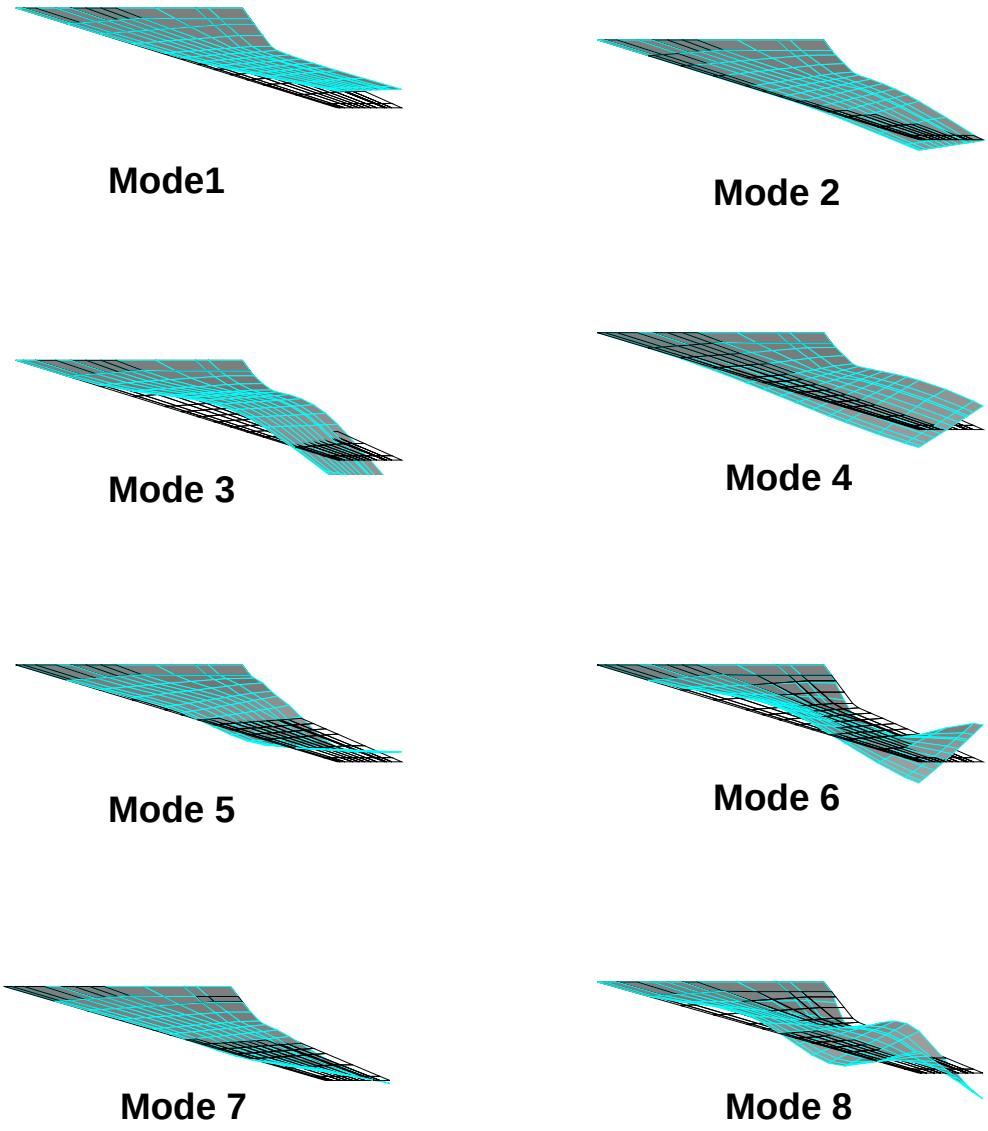

Figure 6.3: ARW Mode Shapes (Mode Shapes are solid Grey)

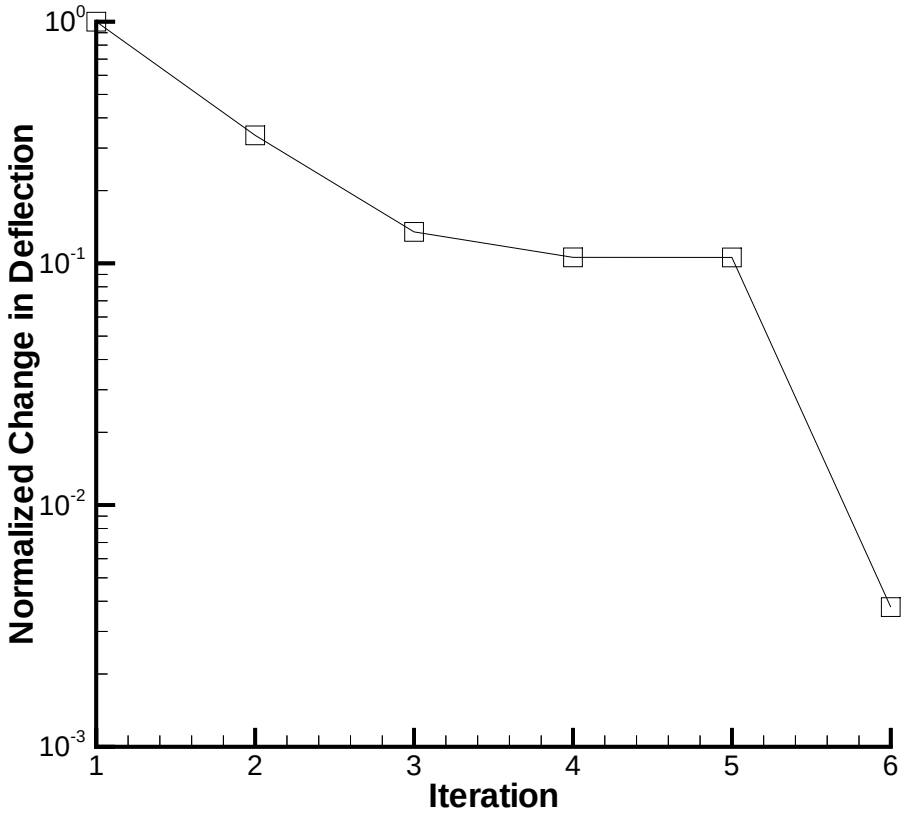

Figure 6.4: Convergence of the Structural Displacement of the ARW using NDM

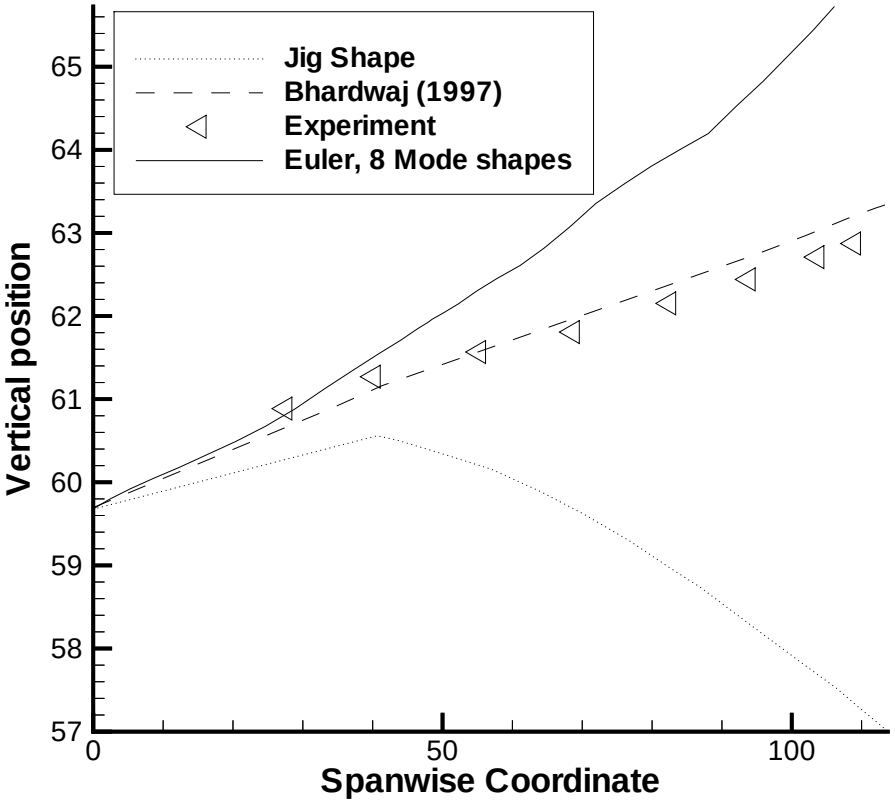

Figure 6.5: ARW Front Spar Deflection

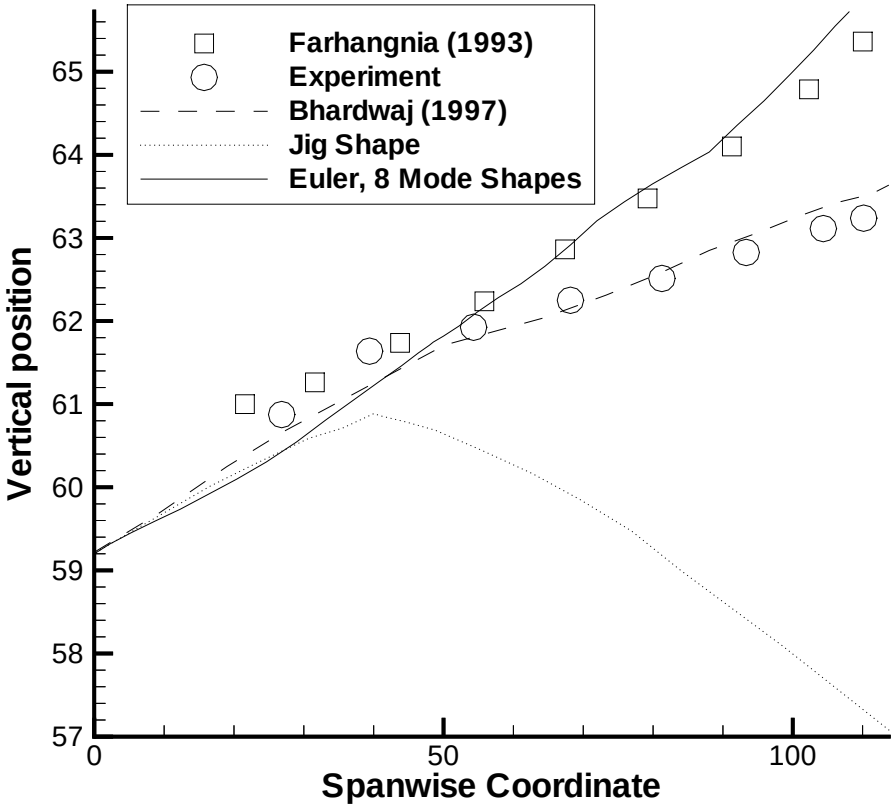

Figure 6.6: ARW Rear Spar Deflection

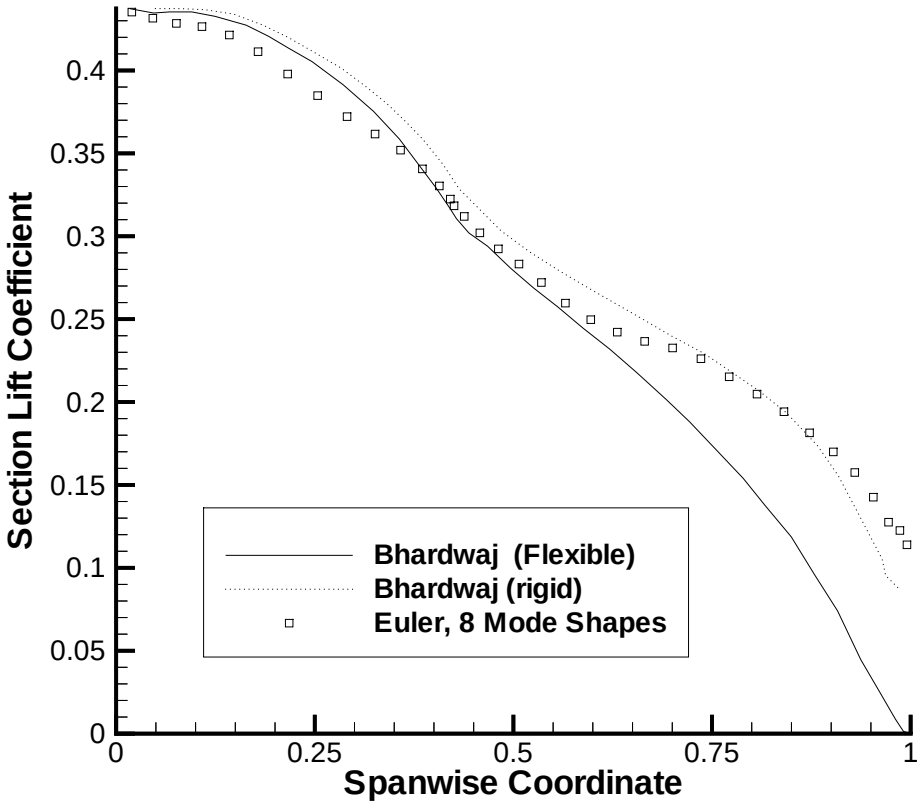

Figure 6.7: Section Lift Coefficient Variation along span for $\alpha = 1^0$

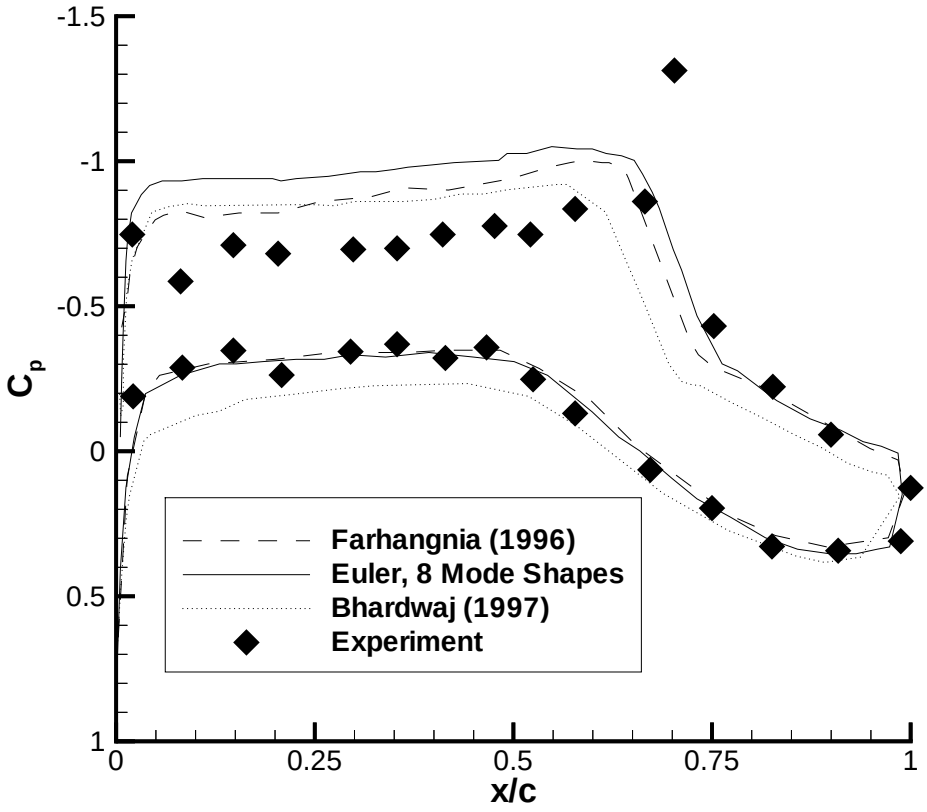

Figure 6.8: C_p plot at 70.7 % spanwise location for $\alpha = 1^0$

Figure 6.9: ARW Wing Deflection (Jig shape is solid grey)

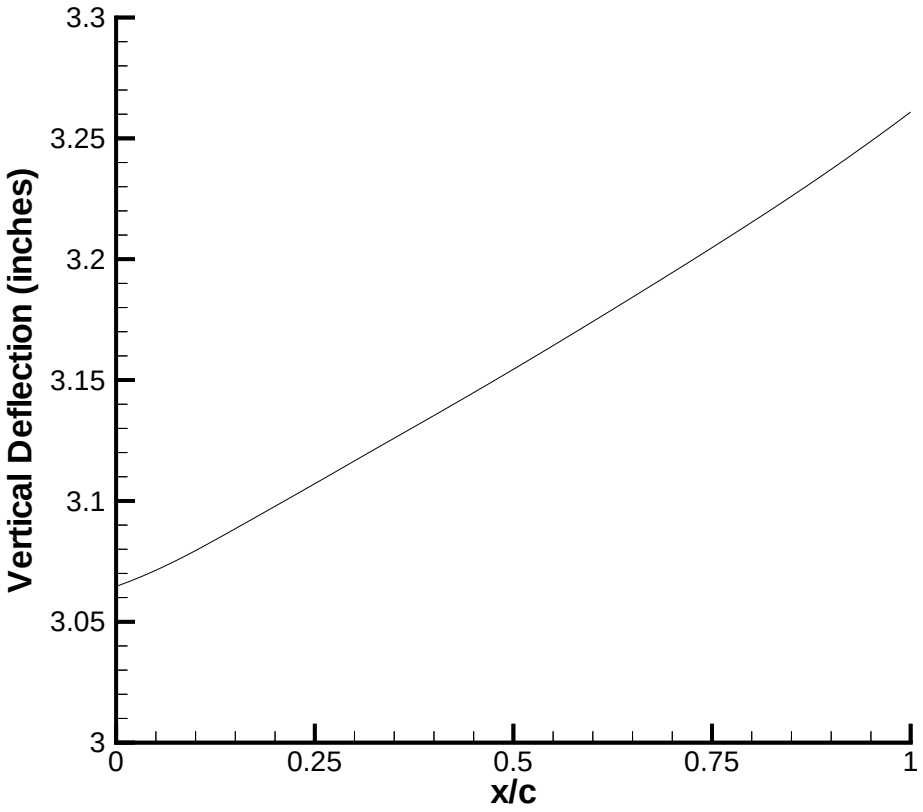

Figure 6.10: ARW Chordwise Deflection at 70.0 % spanwise location

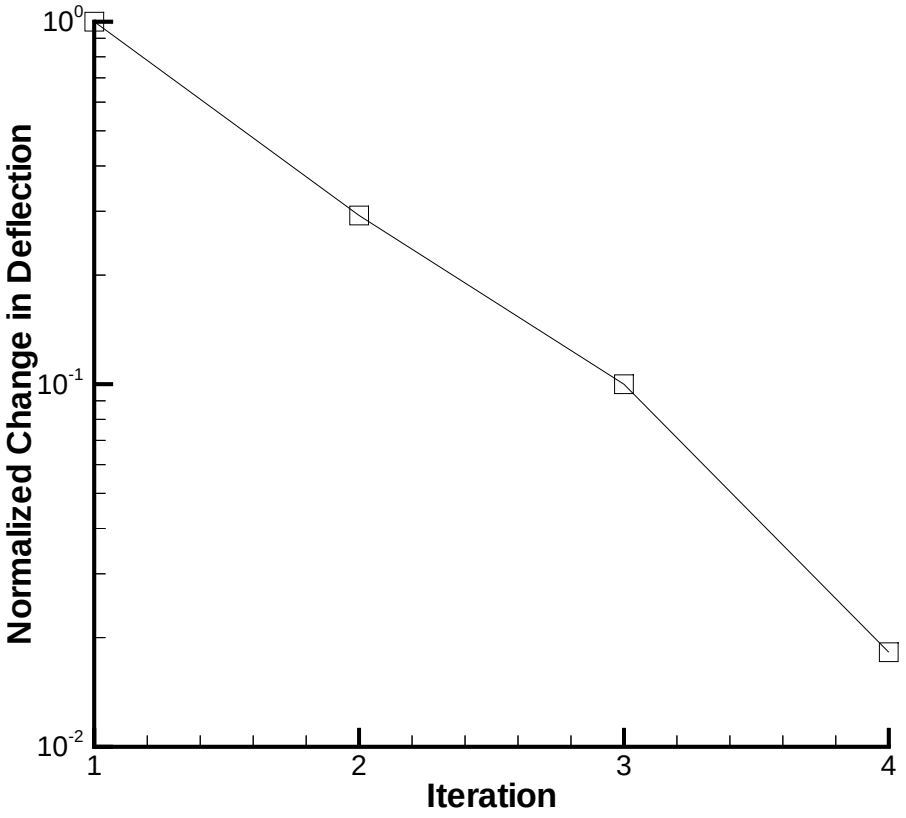

Figure 6.11: ARW Trim Calculation Structural Convergence

Chapter 7

Conclusions

A method was developed to simultaneously determine the deflection and angle of attack for a wing given a specific lift that the wing must generate. Different CFD codes were used, along with different structural codes to successfully calculate the trimmed condition. This demonstrates the modular nature of this research, and the robust nature of the algorithm developed. Results from the derived strongly coupled algorithm are compared with results from a loosely coupled typical non derivative Fixed-Point iterative technique, demonstrating the superiority of the strongly coupled technique in terms of convergence to the trimmed solution, although as mentioned below the strongly coupled technique is far more computational expensive per iteration than the non derivative scheme which requires only 1 CFD solution per iteration.

Both viscous and inviscid solutions were generated, and differences in results were seen, with the viscous results being more accurate based on previously obtained computational and experimental data. The use of the inviscid flow model doesn't result in a markedly different value for the trim angle of attack, but the deflection of the wing, and the span loading are different.

The obvious issue is the practicality of the algorithm developed for this work. That is to say, is this algorithm useful to design engineers working in industry on the design and analysis of aircraft wings. The only answer that can be given is that it depends

upon the circumstances. The algorithm derived here is computationally expensive. For a typical iteration in the trim calculation, 11 CFD solutions are required. This requires a considerable use of the CPU time. If an engineer is interested in generating many results on differing planforms, or if one is in the early stages of design and analysis and the geometry and structural makeup of the wing is subject to many changes, than this method may be too computationally expensive to be of value.

If, however, the case of interest is to perform aeroelastic analysis of a structure, and the engineer is interested in accurate loads or deflections, then this algorithm would seem to be very useful, especially if high speed computers are available. One trim cycle took approximately 4.5 computational hours on a Cray C-90, and typically 4 trim cycles were needed for convergence. Given representative turnaround times on similar machines, a trim calculation could take from 2 to 5 days of wallclock time to perform. If parallel computing could be taken advantage of, this time could drastically decrease.

The issue of CFD convergence should be investigated. For this research, the CFD results were converged three orders of magnitude. If the accuracy of the trim calculations could be maintained while converging the CFD calculations 2 orders of magnitude, this could reduce the high CPU times required in these calculations. Another possible way to increase the practicality of this method and decrease the CPU time required would be the incorporation of recent advances in sensitivity calculations involving CFD into the trim calculations. If it is possible to calculate the sensitivity terms required without the extensive use of CFD solutions, this should be researched. A reduced basis representation of the structural model based on structural modes was used in this research. There are other vectors that can be used to formulate a reduced basis model of the structure. Kapania and Byun[59] compare Ritz vectors to eigenvectors for structural analysis. It is possible that the use of a different reduced basis method may result in the need for fewer variables for the calculations in this research. This could reduce the CPU time needed for non linear trim calculations.

If accurate results are needed, then the difference in deflection results would seem to indicate that a viscous solution is needed for accurate determination of deflections, however an inviscid calculation provides an accurate value for the trim angle of attack. Furthermore, static analysis could be performed with the angle of attack fixed at the trim value.

This research provides a methodology to calculate the trimmed condition of a flexible wing with high fidelity aerodynamic calculations. This ability did not exist when this research began. Hopefully, this work will provide aerodynamicists with a useful tool to use in analysis and design of future aircraft.

Bibliography

[1] J. Sobieszczanski-Sobieski. "Sensitivity of Complex, Internally Coupled Systems," *AIAA-88-2378*, 1988.

[2] A. O. Oloso and A. C. Taylor III. "Aerodynamic Shape Sensitivity Analysis and Design Optimization on the IBM-SP2," *AIAA-97-2273*, 1997.

[3] M. K. Bhardwaj. *A CFD/CSD Interaction Methodology for Aircraft Wings*, Ph.D. thesis, Virginia Polytechnic Institute and State University, 1997.

[4] M. Bhardwaj, R. K. Kapania, C. Byun, and G. P. Guruswamy. "Parallel Aeroelastic Computations Using Coupled Euler Flow and Wing-Box Structural Models," *36th AIAA/ASME/ASCE/AHS/ASC Structures Structural Dynamics and Materials Conference*, AIAA-95-1291, April 1995.

[5] D. L. Knill, V. Balabanov, B. Grossman, W. H. Mason, and R. T. Haftka. "Certification of an Euler Code for High-Speed Civil Transport Design Optimization," *34th Aerospace Sciences Meeting and Exhibit, Reno Nevada*, AIAA-96-0330, January 1996.

[6] A. A. Giunta, V. Balabanov, D. Haim, B. Grossman, W. H. Mason, L. T. Watson, and R. T. Haftka. "Multidisciplinary optimization of a supersonic transport using design of eperiments theory and response surface modelling," *The Aeronautical Journal of the Royal Aeronautical Society*, October 1997.

[7] J. S. Tyll, M. Eaglesham, J. A. Schetz, and M. Deisenroth. "An MDO Design Methodology for the Concurrent Aerodynamic/Cost Design of MagLev Vehicles," *6th AIAA/NASA/ISSMO, Symposium on Multidisciplinary Analysis and Optimization, Bellevue, WA*, AIAA-96-4036, September 1996.

[8] Y. Fung. *An Introduction to the Theory of Aeroelasticity*, Dover, New York, 1955.

[9] G. P. Guruswamy. *User's Guide for ENSAERO-A Multidisciplinary Program for Fluid/Structural/Control Interaction Studies of Aircraft (Release 1)*, NASA Technical Memorandum 1088553, October 1994.

[10] R. Kapania, M. Bhardwaj, E. Reichenback, and G. Guruswamy. "Aeroelastic Analysis of Modern Complex Wings," *6th AIAA/NASA/ISSMO, Symposium on Multidisciplinary Analysis and Optimization, Bellevue, WA*, AIAA-96-4011, September 1996.

[11] R. L. Harder and R. N. Desmarais. "Interpolation Using Surface Splines," *Journal of Aircraft*, 9, No. 2: 189–191, October 1971.

[12] M. C. Sanford, D. A. Seidel, C. V. Eckstrom, and C. V. Spain. "Geometrical and Structural Properties of an Aeroelastic Research Wing (ARW-2)," *NASA TM 4110*, April 1989.

[13] D. E. MacMurdy. *ENSAERO/Plate Preliminary User's Manual*, January 1996.

[14] D. E. MacMurdy. *Aeroelasticity of Wings Coupling Navier–Stokes Aerodynamics with Wing–Box Finite Elements*, Master's thesis, Virginia Polytechnic Institute and State University, 1994.

[15] D. E. MacMurdy, G. P. Guruswamy, and R. K. Kapania. "Aeroelastic Analysis of Wings Using Euler/Navier–Stokes Equations Coupled with Improved Wing-Box Finite Element Structures," *35th AIAA/ASME/ASCE/AHS/ASC Structures, Structural Dynamics and Materials Conference*, AIAA-94-1587, April 1994.

[16] G. Tzong, H. H. Chen, K. C. Chang, T. Wu, and T. Cebici. "A General Method for Calculating Aero-Structure Interaction on Aircraft Configurations," *6th AIAA/NASA/ISSMO Symposium on Multidisciplinary Analysis and Optimization, Bellevue WA*, AIAA-96-3982, September 1996.

[17] McDonnel Douglas. *ADOP User's Manual*, February 1993.

[18] P. G. Buning, W. M. Chan, K. J. Renze, D. Sondak, I. T. Chiu, and J. P. Slotnik. *OVERFLOW User's Manual*, NASA Ames Research Center, 1991.

[19] T. J. Tzong, G. D. Sikes, and M. J. Loikkanen. "Large-Order Modal Analysis Techniques in the Aeroelastic Design Optimization Program (ADOP)," *SAE Technical Paper Series 892323*, September 1989.

[20] R. H. MacNeal. *The NASTRAN Theoretical Manual*, NASA SP-221(01), April 1971.

[21] G. Sikes, G. Tzong, and A. Sharma. "Flutter Optimization of Large Transport Aircraft," *AIAA 92-4795*, 1992.

[22] D. Schuster, J. Vadyak, and E. Atta. "Static Aeroelastic Analysis of Fighter Aircraft Using a Three Dimensional Navier Stokes Algorithm," *28th Aerospace Sciences Meeting*, January 1990.

[23] J. R. Hooker, A. W. Burner, and R. Valla. "Static Aeroelastic Analysis of Transonic Wind Tunnel Models Using Finite Element Methods," *AIAA-97-2243*, 1997.

[24] NASA Langley Research Center. *CFL3DE Version 1.0 User's Manual*, August 1988.

[25] T. W. Purcell, C. J. Borland, and E. N. Tinoco. "Non-Linear Aeroelastic Predictions for Transport Aircraft," *SAE Technical Paper Series 901852*, October 1990.

[26] Avions Marcel Dassault–Breguet, Aviation, Saint–Cloud. *ELFINI Aeroelasticity - General Introduction Manual*, Document No. ELF-AER-1, 1989.

[27] J. K. Nathman and J. M. Barton. "Aeroelastic Calculations With an Euler code," *AIAA-97-2271*, 1997.

[28] E. H. Johnson and V. B. Venkayya. *Automatic Structural Optimization System (ASTROS), Vol 1: Theoretical Manual, AFWAL–TR–88–3028*, Air Force Wright Aeronautical Laboratories, 1988.

[29] F. A. Woodward. "An Improved Method for the Aerodynamic Analysis of Wing–Body– Tail Configurations in Subsonic and Supersonic Flow, Part I – Theory and Applications," *NASA CR–2228*, May 1973.

[30] B. Epstein, A. Luntz, and A. Nachson. "Multigrid Euler Solver about Aircraft Cartesian Grids and Local Refinement," *AIAA–89–1960*, 1989.

[31] J. C. Newman III, A. C. Taylor III, and G. W. Burgreen. "An Unstructured Grid Approach to Sensitivity Analysis and Shapte Optimization Using The Euler Equations," *AIAA-95-1646*, 1995.

[32] J. M. Grasmeyer, A. Naghshineh-Pour, P.-A. Tetrault, B. Grossman, R. T. Haftka, R. K. Kapania, W. H. Mason, and J. A. Schetz. "Multidisciplinary Design Optimization of a Strut-Braced Wing Aircraft with Tip-Mounted Engines," Tech. rep., Multidisciplinary Analysis and Design Center for Advanced Vehicles, Virginia Polytechnic Institute and State University, MAD Center Report 98-01-01, 1998.

[33] J. C. Newman III, P. A. Newman, A. C. Taylor III, and G. J. Hou. "Efficient Nonlinear Static Aeroelastic Wing Analysis," *Computers and Fluids, an international Journal*, December 1996.

[34] G. P. Guruswamy and C. Byun. "Fluid-Structureal Interactions Using Navier-Stokes Flow Equations Coupled with Shell Finite Element Structures," *AIAA 24th Fluid Dynamics Conference*, AIAA-93-3087, June 1993.

[35] K. Appa. "Finite–Surface Spline," *Journal of Aircraft*, 26, No. 5: 495–496, 1986.

[36] C. Byun and G. P. Guruswamy. "A Comparative Study of Serial and Parallel Aeroelastic Computations of Wings," *NASA Technical Memorandum 108805*, January 1994.

[37] B. A. Robinson, J. T. Batina, and H. T. Y. Yang. "Aeroelastic Analysis of Wings Using the Euler Equations With a Deforming Mesh," *AIAA 90-1032*, 1990.

[38] J. T. Batina. "Unsteady Euler Airfoil Solutions Using Unstructured Dynamic Meshes," *AIAA-89-0115*, 1989.

[39] J. T. Batina. "Unsteady Euler Algorithm With Unstructured Dynamic Mesh for Complex-Aircraft Aeroelastic Analysis," *AIAA-89-1189*, 1989.

[40] K. A. Kousen and O. O. Bendiksen. "Limit Cycle Phenomena in Computational Transonic Aeroelasticity," *Journal of Aircraft*, 31, No. 6: 1256–63, November 1994.

[41] M. Karpel and L. Brainin. "Stress Considerations in REduced-Size Aeroelastic Optimization," *AIAA Journal*, 33, No. 4, April 1995.

[42] G. L. Giles. "Equivalent Plate Analysis of Aircraft Wing Box Structures with General Planform Geometry," *Journal of Aircraft*, 23, No. 11: 859–864, November 1986.

[43] G. L. Giles. "Further Generalization of an Equivalent Plate Representation For Aircraft Structural Analysis," *Journal of Aircraft*, 26, No. 1: 67–74, January 1989.

[44] R. K. Kapania and A. E. Lovejoy. "Free Vibration of Thick Generally-Laminated Cantilever Quadrilateral Plates," *AIAA Journal*, July 1996.

[45] J. R. Chawner and J. P. Steinbrenner. "Demonstration of the use of GRIDGEN to Generate A 3D, Multiple Block Structured Grid," *AIAA 92-0069*, 1992.

[46] J. P. Steinbrenner, J. R. Chawner, and D. A. Anderson. "Enhancements to the GRIDGEN System for Increased User Efficiency and Grid Quality," *AIAA-92-0662*, 1992.

[47] K. Appa, M. Yankulich, and D. L. Cowan. "The Determination of Loads and Slope Transformation Matrices for Aeroelastic Analysis," *Journal of Aircraft*, 22, No. 8: 734–736, 1984.

[48] F. N. Fritsch and R. E. Carlson. "Monotone Piecewise Cubic Interpolation," *Society for Industrial and Applied Mathematics, Journal of Numerical Analysis*, 17, No. 2: 238–246, April 1980.

[49] R. M. V. Pidaparti. "Structural and Aerodynamic Data Transformation Using Inverse Isoparametric Mapping," *Journal of Aircraft*, 29, No. 3: 507–509, 1989.

[50] M. J. Smith, D. H. Hodges, and C. E. S. Cesnik. "An Evaluation of Computational Algorithms to Interface Between CFD and CSD Methodology," Tech. rep., Georgia Tech, November 1995.

[51] R. K. Kapania, L. B. Eldred, and J.-F. M. Barthelemy. "Sensitivity Analysis of a Wing Aeroelastic Response," *Journal of Aircraft*, 30, No. 4: 496–504, July 1993.

[52] R. D'Vari and M. Baker. "A Static and Dynamic Aeroelastic Loads and Sensitivity Analysis For Structural Loads Optimization and Its Application to Transport Aircraft," *AIAA-93-1643*, 1993.

[53] R. R. Craig Jr. *Structural Dynamics, An Introduction to Computer Methods*, John Wiley and Sons, New York, pp. 341–377, 1981.

[54] W. H. Chan, I.-T. Chiu, and P. G. Buning. "User's Manual for the HYPGEN Hyperbolic Grid Generator and the HGUI Graphical User Interface," *NASA TM 108791*, October 1993.

[55] M. Farhangnia, G. P. Guruswamy, and S. Biringen. "Transonic-Buffet Associated Aeroelasticity of a Supercritical Wing," *AIAA-96-0286*, 1996.

[56] AEROSOFT. *GASP Version 3.0 User's Manual*, 1996.

[57] C. V. Eckstron, D. A. Seidel, and M. C. Sandford. "Measurements of Unsteady Pressure and Structural Response for an Elastic Supercritical Wing," *NASA Technical Paper 3443*, November 1994.

[58] T. A. Byrdsong, R. R. Adams, and M. C. Sandford. "Close-Range Photogrammetric Measurement of Static Deflections for an Aeroelastic Supercritical Wing," *NASA Technical Memorandum 4194*, 1994.

[59] R. K. Kapania and C. Byun. "Reduction Methods Based on Eigenvectors and Ritz Vectors for Nonlinear Transient Analysis," *Computational Mechanics*, pp. 65–82, November 1993.

[60] C. Hirsch. *Numerical Computation of Internal and External Flows Volume 1 Fundamentals of Numerical Discretization*, Wiley, New York, pp. 26–132, 1988.

[61] J. Bertin and M. L. Smith. *Aerodynamics for Engineers*, Prentice Hall, Englewood Cliffs, New Jersey, page 27, 1989.

[62] J. D. Anderson Jr. *Modern Compresssible Flow With Historical Perspective*, McGraw–Hill, Inc., New York, 1990.

[63] A. H. Shapiro. *The Dynamics and Thermodynamics of Compressible Fluid Flow, Volume I*, The Ronald Press Company, New York, pp. 394-9, 1953.

[64] V. Shankar, W. F. Hall, and S. V. Ramakrishnan. "Quick-Turnaround Computational Simulation," *Computational Science and Engineering*, 5, No. 1: 66–78, January 1998.

[65] J. F. Thompson, Z. U. A. Warsi, and C. W. Mastin. *Numerical Grid Generation Foudations and Applications*, North Holland, New York, pp. 272–276, 1985.

[66] K. E. Tatum and G. L. Giles. "Integrating Nonlinear Aerodynamic and Structural Analysis for a Complete Fighter Configuration," *Journal of Aircraft*, 25, No. 12, AIAA-87-2863, December 1987.

[67] S. D. Senturia, N. Aluru, and J. White. "Simulating the Behavior of MEMS Devices: Computational Methods and Needs," *IEEE Computational Science and Engineering*, pp. 30 – 43, January 1997.

[68] R. L. Burden and J. D. Faires. *Numerical Analysis*, PWS Kent Publishing, New York, 1989.

Appendix A

Levels of Aerodynamic Modeling

A.1 Navier-Stokes Equations

The "most general description of a fluid flow" (Hirsch,[60] p. 29) is given by the Navier-Stokes equations. These equations are an expression of the conservation of momentum for a fluid, although what are commonly referred to as the Navier-Stokes equations are the full set of conservation equations that govern the behavior of a fluid. The assumptions behind the Navier-Stokes equations are that the fluid is a continuum, that the stress is proportional to the rate of strain (that it is a Newtonian fluid) and that Stokes hypothesis holds in the relation between the first and second coefficients of viscosity.

The full Navier-Stokes Equations in Cartesian coordinates are[61]

$$\begin{aligned}
\rho\frac{\partial u}{\partial t} + \rho(\vec{V}\cdot\nabla)u &= \rho f_x - \frac{\partial p}{\partial x} + \frac{\partial}{\partial x}\left(2\mu\frac{\partial u}{\partial x} - \frac{2}{3}\mu\nabla\cdot\vec{V}\right) + \\
&\quad \frac{\partial}{\partial y}\left[\mu\left(\frac{\partial u}{\partial y} + \frac{\partial v}{\partial x}\right)\right] + \frac{\partial}{\partial z}\left[\mu\left(\frac{\partial w}{\partial x} + \frac{\partial u}{\partial z}\right)\right] \qquad \text{(A.1)} \\
\rho\frac{\partial v}{\partial t} + \rho(\vec{V}\cdot\nabla)v &= \rho f_y + \frac{\partial}{\partial x}\left[\mu\left(\frac{\partial u}{\partial y} + \frac{\partial v}{\partial x}\right)\right] -
\end{aligned}$$

$$\begin{aligned} & \frac{\partial p}{\partial y} + \frac{\partial}{\partial x}\left(2\mu\frac{\partial v}{\partial y} - \frac{2}{3}\mu\nabla\cdot\vec{V}\right) + \\ & \frac{\partial}{\partial z}\left[\mu\left(\frac{\partial w}{\partial y} + \frac{\partial v}{\partial z}\right)\right] \\ \rho\frac{\partial w}{\partial t} + \rho(\vec{V}\cdot\nabla)w &= \rho f_z + \frac{\partial}{\partial x}\left[\mu\left(\frac{\partial w}{\partial x} + \frac{\partial u}{\partial z}\right)\right] \\ & \frac{\partial}{\partial y}\left[\mu\left(\frac{\partial v}{\partial z} + \frac{\partial w}{\partial y}\right)\right] - \frac{\partial p}{\partial z} \\ & \frac{\partial}{\partial z}\left(2\mu\frac{\partial w}{\partial z} - \frac{2}{3}\mu\nabla\cdot\vec{V}\right) \end{aligned} \tag{A.2}$$

Neglecting body forces, the Navier-Stokes equations can be expressed more simply as

$$\frac{\partial Q}{\partial t} = \frac{\partial F}{\partial x} + \frac{\partial G}{\partial y} + \frac{\partial H}{\partial z} \tag{A.3}$$

where Q is the vector of conserved variables, and the fluxes F, G and H have an inviscid and a viscous component $F = F_i + F_v$, $G = G_i + G_v$ and $H = H_i + H_v$. So the Navier-Stokes Equations can be expressed as

$$\frac{\partial Q}{\partial t} + \left(\frac{\partial F_i}{\partial x} + \frac{\partial G_i}{\partial y} + \frac{\partial H_i}{\partial z}\right) - \left(\frac{\partial F_v}{\partial x} + \frac{\partial G_v}{\partial y} + \frac{\partial H_v}{\partial z}\right) = 0 \tag{A.4}$$

In generalized coordinates, the Navier-Stokes Equations can be expressed as

$$\frac{1}{J}\frac{\partial Q}{\partial t} + \left(\frac{\partial \hat{F}_i}{\partial \xi} + \frac{\partial \hat{G}_i}{\partial \eta} + \frac{\partial \hat{H}_i}{\partial \zeta}\right) - \left(\frac{\partial \hat{F}_v}{\partial \xi} + \frac{\partial \hat{G}_v}{\partial \eta} + \frac{\partial \hat{H}_v}{\partial \zeta}\right) = 0 \tag{A.5}$$

where J is the Jacobian matrix for the coordinate transformation from the Cartesian x, y, z coordinate system to the generalized ξ, η, ζ coordinate system. Figure A.3 shows a typical 2-D region of a CFD grid.

Several assumptions were made in order to solve these equations numerically in the CFD codes involved in this research. The codes solved the Reynolds Averaged Navier Stokes Equations.

A.2 Reynolds-Averaged Navier-Stokes Equations

In order to solve the Navier-Stokes equations and retain the time dependent nature of the fluids being studies while removing the influence of turbulent fluctuations, turbulent averaged quantities are introduced. A quantity, A can be expressed as a combination of a time averaged mean component and a fluctuating component

$$A = \bar{A} + A' \tag{A.6}$$

where

$$\bar{A}(x,t) = \frac{1}{T}\int_{-T/2}^{T/2} A(x,t+\tau)d\tau \tag{A.7}$$

Where the time scale T is much larger than the time scale of the turbulent fluctuations, but much smaller than any other characteristic time scale of the fluid. By performing the averaging process on the Navier-Stokes equations, the result is the Reynolds-Averaged Navier-Stokes Equations (RANS).

One significant term that results from deriving the RANS equations is the Reynolds stress $-\rho\overline{u'v'}$ and it is this term that turbulence models try to estimate. For this research, both OVERFLOW and GASPv3 used the Baldwin-Lomax turbulence model.

A.3 Thin Layer Navier-Stokes Equations

Discretizing the flow field into logical coordinates, one can neglect all of the viscous flux terms except those in the logical direction normal to the surface of the wing, or body being analyzed. For example, if the surface of interest is in the $x - z$ plane, then the governing equations in Cartesian coordinates become

$$\frac{\partial Q}{\partial t} + \left(\frac{\partial F_i}{\partial x} + \frac{\partial G_i}{\partial y} + \frac{\partial H_i}{\partial z}\right) - \frac{\partial G_{TL}}{\partial y} = 0 \tag{A.8}$$

For generalized coordinates,

$$\frac{1}{J}\frac{\partial Q}{\partial t} + \left(\frac{\partial \hat{F}_i}{\partial \xi} + \frac{\partial \hat{G}_i}{\partial \eta} + \frac{\partial \hat{H}_i}{\partial \zeta}\right) - \frac{\partial \hat{G}_{TL}}{\partial \eta} = 0 \tag{A.9}$$

assuming the surface of interest is in the $\xi - \zeta$ plane, J is the Jacobian matrix for the coordinate transformation, and G_{TL} is the thin layer viscous flux vector. (Fig. A.2). Note that the CFD grid must be much finer in the η direction in this case to calculate the viscous gradients.

The resulting equations are called the Thin Layer Navier-Stokes (TLNS) equations or the Thin Shear Layer equations. This proves to be a reasonable assumption in high Reynolds number flows and where shear layers, wakes and viscous dominated regions are of limited size. For flows along a viscous surface the TLNS equations provide a less computationally expensive way to calculate the flows than through a full Navier-Stokes calculation, while still retaining the ability to calculate separated or reversed regions of flow.

A.4 Euler Equations

Neglecting the viscous fluxes completely results in the Euler equations.

$$\frac{\partial Q}{\partial t} + \left(\frac{\partial F_i}{\partial x} + \frac{\partial G_i}{\partial y} + \frac{\partial H_i}{\partial z}\right) = 0 \tag{A.10}$$

The Euler equations provide a good approximation of fluid behavior away from viscous dominated areas of a fluid flow. Since no viscous terms are calculated, a much coarser grid can be used to solve the Euler equations than the Navier-Stokes equations or the TLNS equations. Since the equations are simpler, and one can use a coarser mesh, the Euler equations are much less expensive to solve in terms of computational time. (Fig. A.1)

The Euler equations were used to calculate the inviscid cases in this research.

A.5 Potential Flow

If fluid flow is assumed to be irrotational and inviscid, then the velocity can be represented by a single scalar potential function, ϕ where the velocity, v, can be expressed as

$$\vec{v} = \nabla\phi \tag{A.11}$$

The basic potential flow equation can be expressed as

$$\frac{\partial \rho}{\partial t} + \nabla \cdot (\rho \nabla \phi) = 0 \tag{A.12}$$

The small disturbance potential equation (Anderson,[62] p. 256)

$$(1 - M_\infty^2)\phi_{xx} + \phi_{yy} + \phi_{zz} = 0 \tag{A.13}$$

is linear and steady. This equation is valid for small perturbations, and it is not valid for transonic flows. For transonic flow, extra terms are needed, and the resulting transonic small disturbance equation is (Anderson,[62] p. 432)

$$(1 - M_\infty^2)\phi_{xx} + \phi_{yy} + \phi_{zz} = M_\infty^2 \left[(\gamma + 1)\frac{\phi_x}{V_\infty}\right]\phi_{xx} \tag{A.14}$$

This equation is non-linear. The assumption that the flow is steady and incompressible reduces the governing equation to the Laplace equation, which is linear.

$$\nabla^2\phi = 0 \tag{A.15}$$

Because of the linearity of the governing equation, a flow field can be expressed as a linear combination of known elementary flows. This forms the basis for panel and lattice methods which are common in engineering research due to the relative ease with which they can be used, and the low CPU times, when compared to CFD, that are required to solve linear aerodynamic calculations. In panel or lattice method, the surface of the body of interest is defined by singularities and control points placed on the body. The combination of the flows resulting from the singularities and boundary conditions enforced at the control points result in the flow field about the body.

The accuracy of panel and lattice methods can be greatly improved with experimental corrections based on existing data. In many cases, similar models are used in the transonic regime as a result of modifications and corrections based on known behavior of the geometry being studied, or similar geometry.

In addition, through compressibility corrections such as Prandtl-Glauert in two dimensions (Anderson[62] pp. 268-9) and Gothert[63] in three dimensions, the accuracy of potential flow calculations in the compressible and transonic regime can be

improved. These developed panel and lattice methods can provide good results. However accuracy outside of the incompressible regime breaks down when one does not have existing data or experimental corrections with which to modify the calculations. Table A.1 from Shankar *et al.*[64] gives an idea of the relative times involved in solving linearized panel methods compared to Euler and Navier-Stokes solvers.

A.6 Grid Generation

One of the most fundamental issues involved in CFD is that of grid generation. Grid generation can be expensive for complex geometry in terms of computer time, but more costly in terms of man hours spent on grid generation.

Two types of grid generators will be discussed here. The first type that we will consider are elliptic grid generators. These solve elliptic partial differential equations to calculate the volume grid. To do this, the user must define all of the boundaries. For a typical structured 3- dimensional grid, this means defining 6 surface grids explicitly and then running an iterative elliptical solver to calculate the interior grid. (See Fig. A.5) Obviously one of the shortcomings of this is that the user must define all of the boundaries and this can be a time consuming task.

A second type of grid generator is the hyperbolic grid generator. In this case, the equations that are solved to calculate the volume grid are hyperbolic in character and as a result, the user can solve these equations in a non-iterative way, and march the solution away from a surface. (Fig. A.4) This makes hyperbolic grid generation ideal for the analysis of a wing, or a body.[65] One drawback is that hyperbolic grid generators can behave poorly around concave surfaces. In this research, the behavior of the grid generator was discovered to be extremely sensitive to spacing parameters especially when the surface grid was densely spaced.

In the aeroelastic analysis, the surface grid of the wing is the only surface grid that has to be generated. For an elliptical solver, the other 5 logical boundaries

would have to be defined. So for this research, the surface grid is defined through a linear combination of the mode shapes, and the volume grid is generated based on that surface grid. Mathematically, if the surface grid is denoted by $\{\vec{G}\}$, then the deflected grid is given by

$$\{\vec{G}_{def}\} = \{\vec{G}_{init}\} + \sum q_i \phi_i \tag{A.16}$$

where q_i is the ith modal amplitude and ϕ_i is the ith mode shape in the aerodynamic coordinate system.

All that is needed is an initial surface grid for the wing. For the simple wing used in the bulk of this research, the surface grid was initially generated at McDonnell Douglas Long Beach and is the same surface grid used for the research by Tzong *et al.*[16] For the ARW research, the surface grid was obtained from Bhardwaj and is the same surface grid used for the CFD results in that research[3] and in the work by Farhangnia *et al.*[55]

Table A.1: Hierarchial Approach to Computational Simulation in Support of Aerospace Design (Shankar *et al.*[64])

Design role	Hierarchial physics	Computational cost(relative)	Computer class
Conceptual phase	Linearized panel methods	1	PC or workstation
Preliminary phase	Nonlinear potential	10	Workstation and
	Inviscid Euler	50	clusters
Final phase	Viscous Navier-Stokes:		Workstation clusters,
	perfect gas	200	MPPs, and Cray
	real gas	1,000	supercomputers
Scientific curiosity	Large Eddy simulation	10,000	Teraflops machines
	Direct Navier-Stokes	100,000	

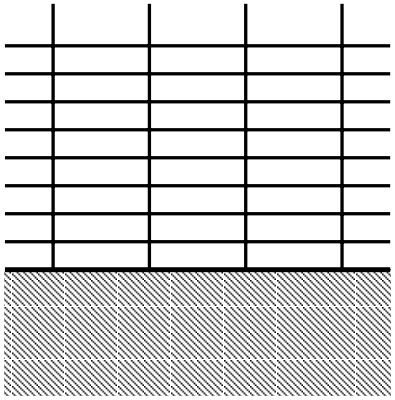

Typical grid near a viscous surface

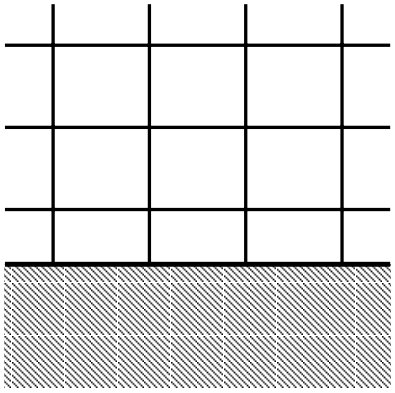

Typical grid near an inviscid surface

Figure A.1: Comparison Between Viscous and Inviscid CFD Grids

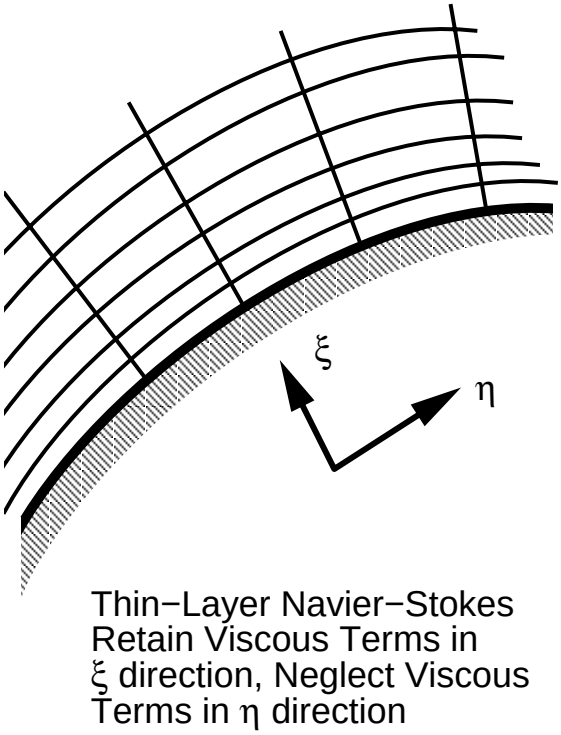

Figure A.2: Typical Grid for a Viscous Surface

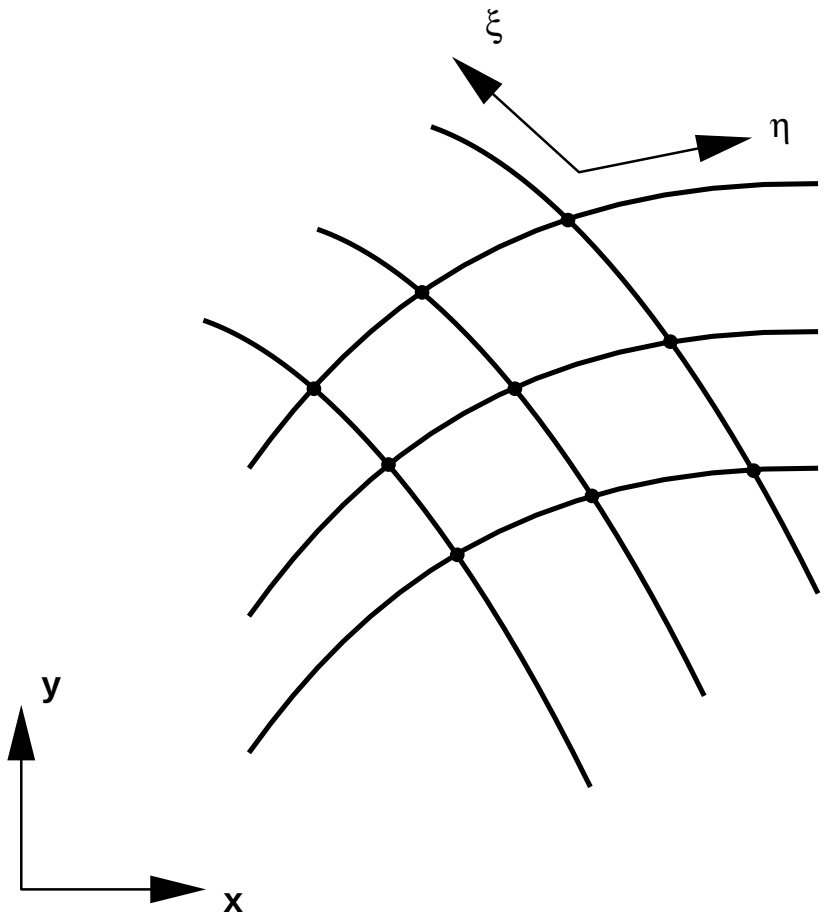

Figure A.3: Typical Discretization of a flow field

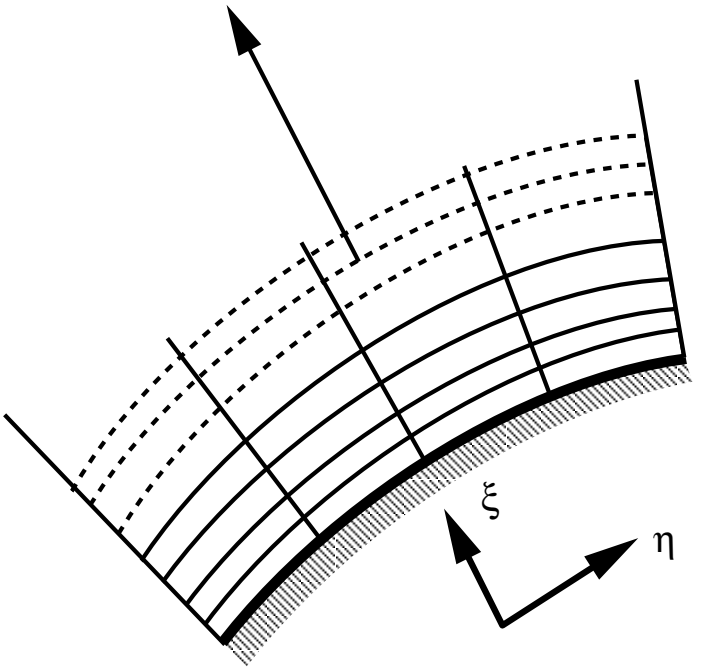

Figure A.4: Hyperbolic Grid Generation

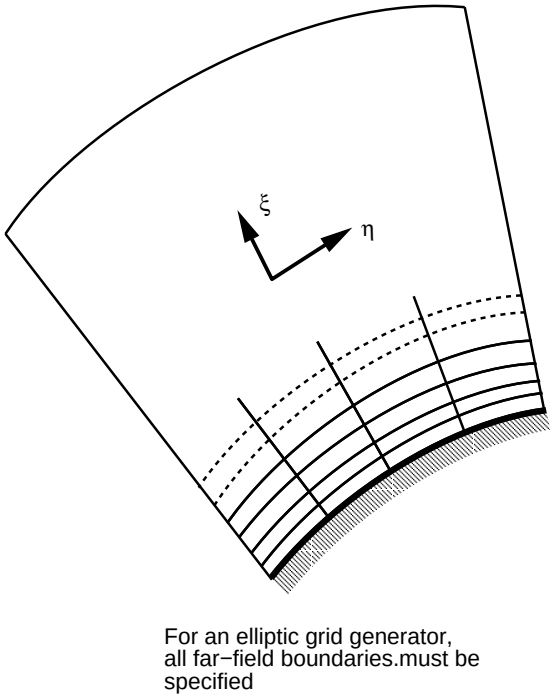

Figure A.5: Elliptical Grid Generation

Appendix B

Structural Modeling Using Modal Analysis

In this research, structural modeling is performed using a modal representation. This approach begins with an eigenvalue problem. If $[K]$ is the stiffness matrix, and $[M]$ is the mass matrix for the structure,

$$([K] - \omega^2[M])U = 0 \tag{B.1}$$

with the characteristic equation

$$det([K] - \omega^2[M]) = 0 \tag{B.2}$$

which results in an nth degree polynomial for ω^2 which are the squares of the natural frequency of the structure. The eigenvector, U_i that corresponds with the eigenvalue ω^2 is known as the ith mode shape, and from here on will be called ϕ_i. As it's name implies, the mode shapes can be determined to within a constant factor, and can be scaled up or down hence the name mode *shape*. The eigenvalues are the

normal vibrational frequencies of the structure, and the corresponding mode shapes are the physical shape of the vibration that goes along with that frequency.

From what is called the expansion theorem,[53] the mode shapes form a mutually orthogonal set of n-dimensional vectors. An arbitrary vector, c can be expressed as a linear combination of the mode shapes

$$c = \sum_{i=1}^{n} q_i \phi_i \tag{B.3}$$

A result of this is that any deflection can be represented as a linear combination of the mode shapes of a structure. Another key ingredient in the use of mode shapes to represent structural deflections is the issue of truncation. If the structure has n degrees of freedom, then it will have n mode shapes. This can be a very large number for real structures. So what is used is a reduced basis representation. The mode shapes are truncated, and a smaller number are used to represent the deflection c such that

$$c = \sum_{i=1}^{N} q_i \phi_i \tag{B.4}$$

where

$$N << n$$

The advantage of this method is its simplicity and the fact that it is computationally inexpensive. Initially the mode shapes must be calculated along with the eigenvalues, but after that structural calculations are negligible in terms of computational expense. For aeroelastic problems typically on the order of 10 modes are used.(reference papers that use mode shapes. Tzong, plus the one that talks about

flutter optimization.) The FEM model of the simple wing used in this research had approximately 500 degrees of freedom. Using a modal representation with 8 mode shapes, the number of structural variables was reduced by two orders of magnitude.

The method of modal superposition as outlined here is a common way to model structural behavior in aeroelastic problems.[19, 55, 66] It produces accurate results for very little computational effort.

Appendix C

Numerical Aspects

C.1 Newton's Method

Newton's method is a simple and powerful root finding method, it solves the problem $f(x) = 0$. Newton's method is a member of a larger class of root finding methods known as fixed point methods. To derive Newton's Method, Consider the function f that is twice differentiable on $[a, b]$. Assume that x_0 is an approximation to p, a root of f such that $f'(x_0) \neq 0$ although $|x_0 - p|$ is small. Begin with series expansion of $f(x)$ about x_0.

$$f(x) = f(x_0) + (x - x_0)f'(x_0) + \frac{(x - x_0)^2}{2}f''(\xi(x)) \tag{C.1}$$

where $\xi(x)$ is between x and x_0. Solving for p, a root of $f(x)$, the Taylor series expansion becomes

$$0 = f(x_0) + (p - x_0)f'(x_0) + \frac{(p - x_0)^2}{2}f''(\xi(p)) \tag{C.2}$$

If $|p - x_0|$ is small, then $(p - x_0)^2$ becomes negligible and so

$$0 \approx f(x_0) + (p - x_0)f'(x_0) \tag{C.3}$$

Since this is a root finding problem, solving for p results in

$$p \approx x_0 - \frac{f(x_0)}{f'(x_0)} \tag{C.4}$$

Newton's method is an iterative method whereby the ith approximation to the root, p is

$$p_i = p_{i-1} - \frac{f(p_{i-1})}{f'(p_{i-1})}, i \geq 1 \tag{C.5}$$

See figure C.1 for a graphical interpretation of Newton's Method.[67]

To determine convergence of Newton's Method, one can look at the terms

$$|p_i - p_{i-1}| < \varepsilon \tag{C.6}$$

or

$$f(p_i) < \varepsilon \tag{C.7}$$

where ε is a predetermined tolerance. It can be shown that if a root exists on the interval $[a, b]$ and if $f'(p) \neq 0$, then there exists $\delta > 0$ such that Newton's method will converge to p for an initial guess $p_0 \in [p - \delta, p + \delta]$. (Burden and Faires[68] , pp 47-51)

Using a first order finite difference approximation to $f'(p_{i-1})$,

$$f'(p_{i-1}) \approx \frac{f(p_{i-1}) - f(p_{i-2})}{p_{i-1} - p_{i-2}} \tag{C.8}$$

Incorporating this into the formulation for Newton's method, the result is what is known as the Secant method.

$$p_i = p_{i-1} - \frac{f(p_{i-1})(p_{i-1} - p_{i-2})}{f(p_{i-1}) - f(p_{i-2})} \tag{C.9}$$

This can be extremely useful when one is interested in a root finding problem where $f'(x)$ cannot be found analytically or is too complicated to be readily calculated.

C.2 Newtons Method for Systems of Equations

Newton's Method solves for p such that $f(p) = 0$. This problem can be extended to a system of equations such that one is trying to find $\vec{x}$ where $[F(\vec{x})] = \vec{0}$.

The formulation of this problem is similar to that for one variable.

$$\vec{x}^{(k)} = \vec{x}^{(k-1)} - [J(\vec{x}^{(k-1)})]^{-1}[F(\vec{x}^{(k-1)})] \tag{C.10}$$

In this case, the matrix $[J(\vec{x})]$ is known as the Jacobian matrix and if

$$[F(\vec{x})] = \begin{bmatrix} f_1(\vec{x}) \\ f_2(\vec{x}) \\ \vdots \\ f_N(\vec{x}) \end{bmatrix}, \vec{x} = \begin{bmatrix} x_1 \\ x_2 \\ \vdots \\ x_N \end{bmatrix} \tag{C.11}$$

then

$$[J(\vec{x})] = \begin{bmatrix} \frac{\partial f_1(\vec{x})}{\partial x_1} & \frac{\partial f_1(\vec{x})}{\partial x_2} & \cdots & \frac{\partial f_1(\vec{x})}{\partial x_N} \\ \frac{\partial f_2(\vec{x})}{\partial x_1} & \frac{\partial f_2(\vec{x})}{\partial x_2} & \cdots & \frac{\partial f_2(\vec{x})}{\partial x_N} \\ \vdots & \vdots & \ddots & \vdots \\ \frac{\partial f_N(\vec{x})}{\partial x_1} & \frac{\partial f_N(\vec{x})}{\partial x_2} & \cdots & \frac{\partial f_N(\vec{x})}{\partial x_N} \end{bmatrix} \tag{C.12}$$

Note that $[J(\vec{x})]$ must be inverted for each iteration, although this can be avoided if one solves for $\vec{y}$ such that $[J(\vec{x}^{(k)})]\vec{y} = -[F(\vec{x}^{(k)})]$ and then updates $\vec{x}$ as $\vec{x}^{(k+1)} = \vec{x}^{(k)} + \vec{y}$.

Convergence for Newton's method for systems of equations is given in the following theorem (Burden and Faires,[68] pp 536-539)

Suppose $\mathbf{p}$ is a solution of $\mathbf{G}(\mathbf{x}) = \mathbf{x}$ for some function $\mathbf{G} = (g_1, g_2, \ldots, g_n)^t$ mapping $\Re^n$ into $\Re^n$. If a number $\delta > 0$ exists with th property that

1. $\partial g_i/\partial x_j$ is continuous on $N_\delta = \{\mathbf{x} | \|\mathbf{x} - \mathbf{p}\| < \delta\}$ for each $i = 1, 2, \ldots, n$ and $j = 1, 2, \ldots, n$,

2. $\partial^2 g_i(\mathbf{x})/(\partial x_j \partial x_k)$ is continuous, and $|\partial^2 g_i(\mathbf{x})/(\partial x_j \partial x_k)| \leq M$ for some constant M, whenever $\mathbf{x} \subset N_{delta}$ for each $i = 1, 2, \ldots, n$, $j = 1, 2, \ldots, n$, and $k = 1, 2, \ldots, n$,

3. $\partial g_i(\mathbf{p})/\partial x_j = 0$ for each $i = 1, 2, \ldots, n$ and $j = 1, 2, \ldots, n$,

then a number $\hat{\delta} \leq \delta$ exists such that the sequence generated by $\mathbf{x^k} = \mathbf{G}(\mathbf{x^{(k-1)}})$ converges quadratically to $\mathbf{p}$ for any choice of $\mathbf{x}^{(0)}$, provided that $\|\mathbf{x^{(0)}} - \mathbf{p}\| < \hat{\delta}$. Moreover,

$$\|\mathbf{x^{(k)}} - \mathbf{p}\|_\infty \leq \frac{n^2 M}{2} \|\mathbf{x^{(k-1)}} - \mathbf{p}\|_\infty^2 \; for \; each \; k \geq 1. \tag{C.13}$$

C.3 Non Derivative Method

The non derivative method is a simple version of fixed point iteration. Fixed point iteration is a numerical scheme to calculate the fixed point of a function. A fixed-point p for a function, $g(p)$ is where $g(p) = p$. Numerically the scheme can be expressed as

$$p_n = g(p_{n-1}) \tag{C.14}$$

Convergence is given in the following theorem (Burden and Faires,[68] pp. 38-43)

(Fixed-Point Theorem) Let $g \in\subset [a, b]$ and suppose that $g(x) \in [a, b]$ for all x in $[a, b]$. Further, suppose g' exists on (a,b) with

$$|g'(x)| \leq k < 1 \; for \; all \; x \in (a, b) \tag{C.15}$$

if p_0 is any number in $[a, b]$, then the sequence defined by

$$p_n = g(p_{n-1}), n > 1 \tag{C.16}$$

converges to the unique fixed point p in $[a, b]$.

If one can re-state a root finding problem for $f(p) = 0$ as a fixed point problem where $g(p) = p$ then the non derivative method can be used as a root finding algorithm.

C.4 Non Derivative Method for Systems of Equations

For a system of equations $[G]$, a fixed point $\vec{p}$ is defined as $[G(\vec{p})] = \vec{p}$. An iterative algorithm to find $\vec{p}$ can be expressed as

$$\vec{p}^{(k)} = [G(\vec{p}^{(k+1)})] \tag{C.17}$$

Otherwise, the solution of a system of equations by the non derivative method is analogous to the solution of a problem with one variable. See figure C.2 for a graphical interpretation of the non derivative method[67] for a system of equations.

Convergence for the non derivative method for systems of equations is given in the following theorem (Burden and Faires,[68] pp 528-531)

Let $D = \{(x_1, x_2, \ldots, x_n) | a_i \leq x_i \leq b_i \; for \; each \; i = 1, 2, \ldots, n\}$ for some collection of constants $a_1, a_2, \ldots, a_n$ and $b_1, b_2, \ldots, b_n$. Suppose $\mathbf{G}$ is a continuous function from $D \subset \Re^n$ into $\Re^n$ with the property that $\mathbf{G}(\mathbf{x}) \in D$ whenever $x \in D$. Then $\mathbf{G}$ has a fixed point in D.

Moreover, suppose $\mathbf{G}$ has continuous partial derivatives and a constant $K < 1$ exists with

$$\left| \frac{\partial g_i(\mathbf{x})}{\partial x_j} \right| \leq \frac{K}{n} \; whenever \; x \subset D, \tag{C.18}$$

for each $j = 1, 2, \ldots, n$ and each component function g_i. Then the sequence $\{\mathbf{x}^{(k)}\}_{k=0}^{\infty}$ defined by an arbitrarily selected $\mathbf{x}^{(0)}$ in D and generated by

$$\mathbf{x}^{(k)} = G(\mathbf{x}^{(k-1)}) \; for \; each \; k \geq 1 \tag{C.19}$$

converges to the unique fixed point $\mathbf{p} \in D$ and

$$\|\mathbf{x}^{(k)} - \mathbf{p}\|_\infty \leq \frac{K^k}{1 - K} \|\mathbf{x}^{(1)} - \mathbf{x}^{(0)}\|_\infty. \tag{C.20}$$

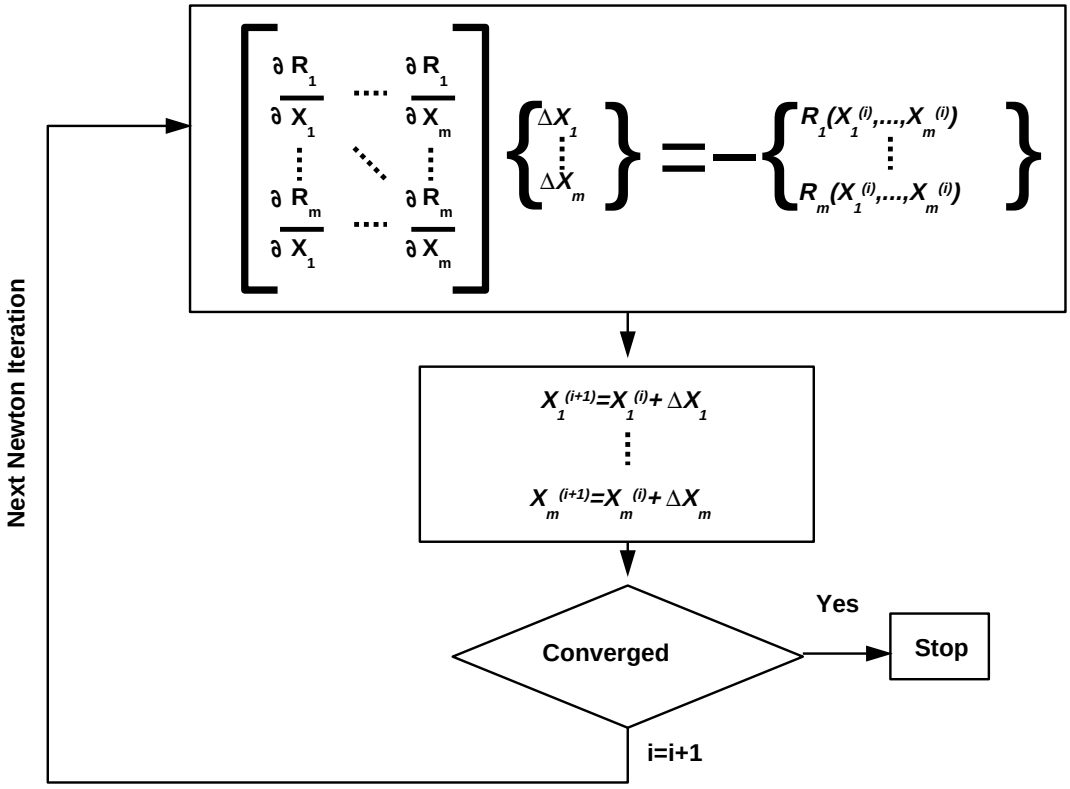

Figure C.1: Newton's Method

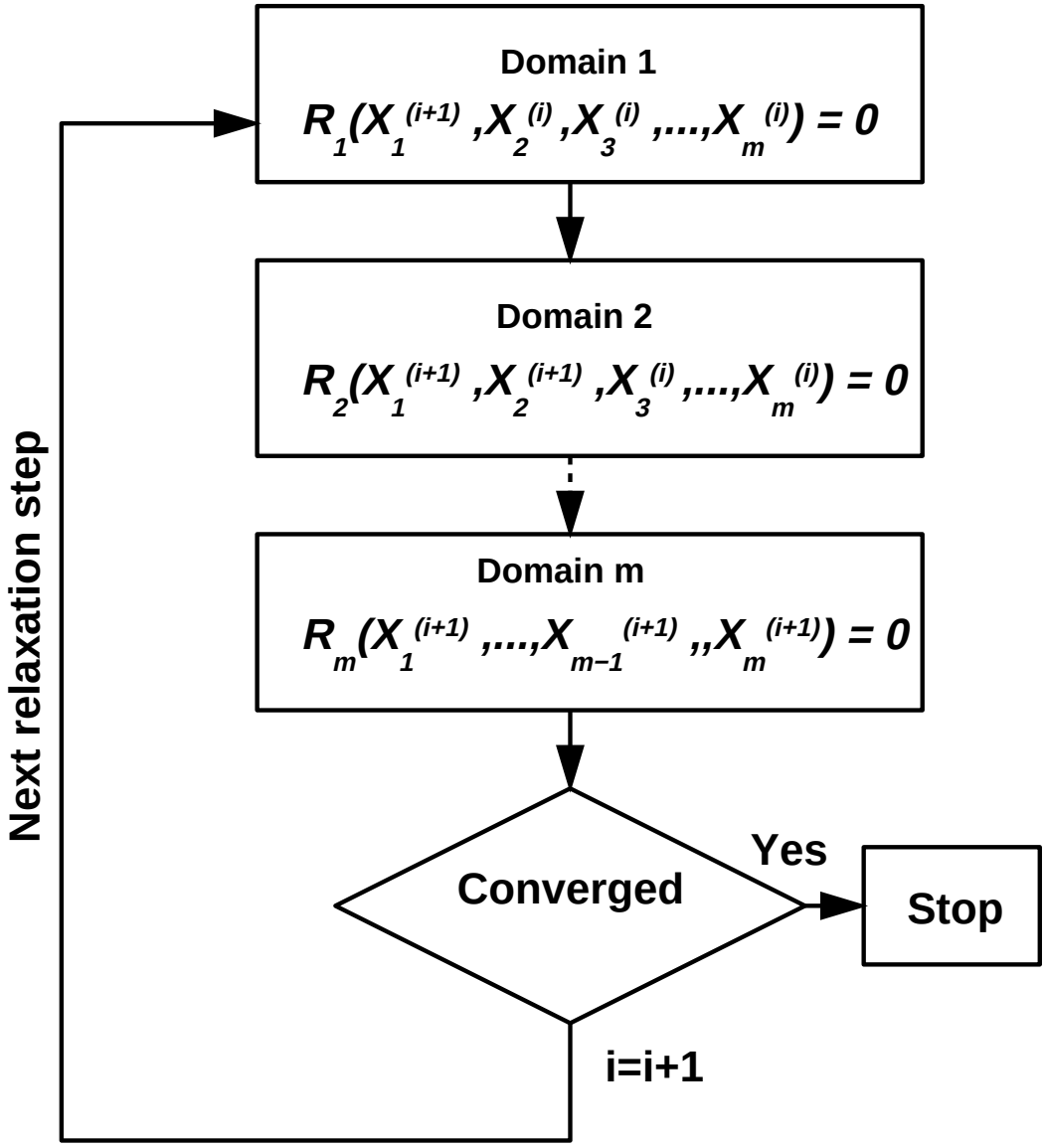

Figure C.2: Non Derivative Method (NDM)

vita

David Erik Cohen was born on Thanksgiving day 1969 in Washington D.C. He spent most of his childhood in suburban Virginia. He graduated from Mount Vernon High School in 1987 and based on his interest in airplanes, he entered Virginia Tech to study Aerospace Engineering, graduating with his B.S. in the spring of 1991. David spent the fall of 1995 at McDonnel Douglas in Long Beach California. He will be working at the Standard Missile Company in McLean Virginia upon completion of his Ph.D.